

COMPRESSIVE BEHAVIOR OF BULK METALLIC GLASS UNDER
DIFFERENT CONDITIONS —
COUPLED EFFECT OF TEMPERATURE AND STRAIN RATE

by

Weihua Yin

A dissertation submitted to the faculty of
The University of North Carolina at Charlotte
in partial fulfillment of the requirements
for the degree of Doctor of Philosophy in
Mechanical Engineering

Charlotte

2013

Approved by:

Dr. Qiuming Wei

Dr. Laszlo Kecskes

Dr. Aixi Zhou

Dr. Haitao Zhang

Dr. Jing Zhou

©2013
Weihua Yin
ALL RIGHTS RESERVED

ABSTRACT

WEIHUA YIN. Compressive behavior of bulk metallic glass under different conditions — Coupled effect of temperature and strain rate. (Under the direction of DR. QIUMING WEI)

Metallic glass was first reported in 1960 by rapid quenching of Au-Si alloys. But, due to the size limitation, this material did not attract remarkable interest until the development of bulk metallic glasses (BMGs) with specimen sizes in excess of 1 mm. BMGs are considered to be promising engineering materials because of their ultrahigh strength, high elastic limit and wear resistance. However, they usually suffer from a strong tendency for localized plastic deformation with catastrophic failure. Many basic questions, such as the origin of shear softening and the strain rate effect remain unclear. In this thesis, the mechanical behavior of the $Zr_{55}Al_{10}Ni_5Cu_{30}$ bulk metallic glass and a metallic glass composite is investigated.

The stress-strain relationship for $Zr_{55}Al_{10}Ni_5Cu_{30}$ over a wide range of strain rate (5×10^{-5} to $2 \times 10^3 s^{-1}$) was investigated in uniaxial compression loading using both MTS servo-hydraulic system (quasi-static) and compression Kolsky bar system (dynamic). The effect of the strain rate on the fracture stress at room temperature was discussed. Based on the experimental results, the strain rate sensitivity of the bulk metallic glass changes from a positive value to a negative value at high strain rate, which is a consequence of the significant adiabatic temperature rise during the dynamic testing. In order to characterize the temperature effect on the mechanical behavior of the metallic glass, a synchronically assembled heating unit was designed to be attached onto the Kolsky bar system to perform high temperature and high strain

rate mechanical testing. A transition from inhomogeneous deformation to homogeneous deformation has been observed during the quasi-static compressive experiments at testing temperatures close to the glass transition temperature. However, no transition has been observed at high strain rates at all the testing temperatures. A free volume based model is applied to analyze the stress-strain behavior of the homogeneous deformation. To further examine the inelastic deformation of the Zr-based bulk metallic glasses, instrumented nanoindentation experiments were performed. A transition from discrete plastic deformation to continuous plastic deformation was found when strain rate is increased but still within the quasi-static strain rate region. Motivated by the metal matrix composite material, a tungsten reinforced BMG composite was investigated at quasi-static and dynamic strain rates. The mechanical behavior of the metallic glass matrix was improved significantly by the addition of W particles.

ACKNOWLEDGMENTS

I would like to express my deep gratitude to my advisor, Dr Qiuming Wei and Dr. Laszlo Kecskes for advising me during the 5 years Ph.D study and research. I also would like to deeply appreciate Dr. Hiatao Zhang, Dr. Aixi Zhou and Dr. Jing Zhou for being my committee members and giving me valuable suggestions on my dissertation research. Thanks to GASP grant support from the University of North Carolina at Charlotte and the support from Army Research Laboratory.

At last but not the least, I would like to express my special thanks to my lovely wife Xianlin. Thanks to her for alway believing in and supporting me.

TABLE OF CONTENTS

| | |
|--|------|
| LIST OF FIGURES | viii |
| LIST OF TABLES | x |
| CHAPTER 1: INTRODUCTION | 1 |
| 1.1 Motivation | 1 |
| 1.2 Metallic Glasses | 4 |
| 1.3 Mechanical Properties of Bulk Metallic Glasses | 8 |
| 1.4 Zr-Based Bulk Metallic Glass | 15 |
| CHAPTER 2: ROOM TEMPERATURE BEHAVIOR | 18 |
| 2.1 Introduction | 18 |
| 2.2 Materials and Experimental Procedure | 20 |
| 2.3 Experimental results | 23 |
| 2.4 Discussion | 27 |
| 2.5 Summary and concluding remarks | 46 |
| CHAPTER 3: ELEVATED TEMPERATURE BEHAVIOR | 48 |
| 3.1 Introduction | 48 |
| 3.2 Experimental procedures | 50 |
| 3.3 Experimental Results | 56 |
| 3.4 Discussion | 62 |
| 3.5 Conclusion | 72 |

| | |
|--|-----|
| CHAPTER 4: NANOINDENTATION EXPERIEMNTS | 74 |
| 4.1 Introduction | 74 |
| 4.2 Experimental Procedure | 78 |
| 4.3 Experimental Results | 81 |
| 4.4 Discussion | 89 |
| 4.5 Conclusions | 100 |
| CHAPTER 5: W-REINFORCED BMG COMPOSITE | 102 |
| 5.1 Introduction | 102 |
| 5.2 Materials and experimental procedure | 104 |
| 5.3 Experimental results | 105 |
| 5.4 Discussion | 111 |
| 5.5 Conclusions | 114 |
| CHAPTER 6: CONCLUSIONS AND FUTURE WORK | 116 |
| REFERENCES | 119 |

LIST OF FIGURES

| | |
|--|----|
| FIGURE 1: Schematic drawing of TTT diagram of metallic glass system. | 6 |
| FIGURE 2: Strain rate effect of different BMG systems. | 9 |
| FIGURE 3: Elastic limit versus Young's modulus. | 15 |
| FIGURE 4: DSC curve of the Zr-based bulk metallic glass. | 16 |
| FIGURE 5: Schematic of Kolsky bar system. | 23 |
| FIGURE 6: Kolsky bar signal from strain gage.. | 24 |
| FIGURE 7: QS and DY stress-strain curves of BMGs. | 25 |
| FIGURE 8: Fracture angle of metallic glass under quasi-static loading. | 26 |
| FIGURE 9: SEM images of quasi-static post-loading sample. | 27 |
| FIGURE 10: SEM images of dynamic post-loading sample. | 28 |
| FIGURE 11: The fracture strength of BMGs Vs. the strain rate. | 29 |
| FIGURE 12: First load serration during QS tests Vs. strain rate. | 30 |
| FIGURE 13: True stress-strain curve for Zr-based BMG. | 32 |
| FIGURE 14: The displacement burst at different QS strain rates. | 37 |
| FIGURE 15: Viscosity inside shear band. | 38 |
| FIGURE 16: SEM image of the tested Zr-based metallic glass sample. | 39 |
| FIGURE 17: Strain rate sensitivity within QS strain rate region. | 41 |
| FIGURE 18: Synchronically assembled heating system. | 54 |
| FIGURE 19: Time gap measurement. | 56 |
| FIGURE 20: High temperature QS true stress-strain curves. | 57 |
| FIGURE 21: High temperature DY true stress-strain curves. | 58 |

| | |
|---|-----|
| FIGURE 22: Maximum stress plotted as a function of temperature. | 59 |
| FIGURE 23: SEM images of Zr-BMG QS-tested at room temperature. | 60 |
| FIGURE 24: SEM images of Zr-BMG QS-tested at 550K. | 62 |
| FIGURE 25: SEM images of Zr-BMG DY-tested at 698K. | 63 |
| FIGURE 26: Experimental and simulated result of QS compression test. | 67 |
| FIGURE 27: Free volume model prediction. | 68 |
| FIGURE 28: The failure stress at different temperature and the fitted curve. | 70 |
| FIGURE 29: A typical $h - p$ curve of nanoindentation result. | 76 |
| FIGURE 30: Strain rate Versus displacement during the strain rate jump test. | 82 |
| FIGURE 31: An AFM image and profile of an indentation. | 83 |
| FIGURE 32: Typical $h-p$ curves measured from nanoindentation experiments. | 84 |
| FIGURE 33: Maximum displacement during the load control tests. | 85 |
| FIGURE 34: H and p Vs. h during displacement-control with $1 \times 10^{-3} s^{-1}$. | 86 |
| FIGURE 35: H and p Vs. h during displacement-control with $1 \times 10^{-1} s^{-1}$. | 88 |
| FIGURE 36: H as a function of $\dot{\epsilon}$ with strain rate jump test. | 89 |
| FIGURE 37: $\dot{\epsilon}$ plotted as a function of the indentation depth | 90 |
| FIGURE 38: SEM images of the as received composite. | 105 |
| FIGURE 39: True strain-stress curve of the composite under QS compression. | 107 |
| FIGURE 40: True strain-stress curve of the composite under DY compression. | 108 |
| FIGURE 41: SEM images of QS post-mortem composite specimen. | 109 |
| FIGURE 42: SEM images of DY post-mortem composite specimen. | 110 |

LIST OF TABLES

| | |
|--|-----|
| TABLE 1: Fundamental properties and potential applications of BMGs. | 14 |
| TABLE 2: Physical and mechanical properties of $Zr_{55}Al_{10}Ni_5Cu_{30}$. | 16 |
| TABLE 3: Temperature increase of Zr-BMG associated with serrated flows. | 34 |
| TABLE 4: Physical and mechanical properties of W-BMG composite. | 104 |

CHAPTER 1: INTRODUCTION

1.1 Motivation

Metallic alloys are traditionally considered as crystalline in nature, whose constituent atoms are arranged in an ordered pattern periodically in three dimensions. The structures of crystalline metallic alloys have been well studied. The structure can be divided into 7 crystal systems, 14 Bravais lattices and 230 space groups. Two metals may have the same Bravais lattice, but the difference in the lattice parameters and inter-axial angles render them into totally different materials. Because of this structural periodicity, the deformation of crystalline metals can proceed via activities of dislocations and deformation twinning.

But when the structural periodicity is absent and the atoms are randomly packed together, the materials are considered as "noncrystalline". "Amorphous" and "glassy" are other terms to describe this random arrangement of atoms in the solid state. The first metallic glass was discovered in 1960, when Klement and his coworkers [79] were trying to rapidly solidify a liquid Au-Si alloy using splat quenching with a cooling speed approaching a million Kelvin per second. The amorphous metal they created was only a 10 μm thick ribbon. The exploitation for the structural application of metallic glasses was not widely performed because of the limitation of the extreme production conditions required and the very small size of the samples. But in 1974,

the first bulk metallic glass(BMG) was developed by Chen [9]. At present, bulk metallic glasses can be produced at relatively low cooling rates having well designed compositions. The so-called term "bulk" means that the diameter of a cast rod of the amorphous metal or alloy is larger than 10 mm.

The mechanical properties of metallic glasses are closely related to the amorphous state of the atomic structure. The amorphous alloys generally exhibit the same order of magnitude of elastic modulus as their conventional engineering metals, but have a larger elastic limit with a significant increase in their strength. Also the high hardness, great wear and corrosion resistance and good forming ability make them as excellent candidates as structural materials.

But due to the large-scale random atomic arrangement, the characterization of metallic glasses is very difficult compared to the structural analysis of crystalline alloys. The structure-properties relationship is still unclear for metallic glasses. Since the development of bulk metallic glasses, there are a great number of research efforts concerning the mechanical behavior of bulk metallic glasses. Nevertheless, the complete characterization of the mechanical behaviors, particularly the plastic deformation mechanisms of BMGs, is still incomplete. In order to make bulk metallic glasses widely used as structural materials, the understanding of their mechanical behavior at large is necessary. For example, it is well known that the mechanical properties of conventional crystalline metals and alloys usually, more or less, exhibit strain rate and temperature dependence[21, 160, 161, 150, 46]. A great number of efforts have been undertaken to understand the coupled effect of temperature and strain rate on the mechanical properties of crystalline metals and alloys and as such certain

common features have been identified for these materials. However, this is largely not the case for bulk metallic glasses. First of all, most of the experimental work in the literature on the mechanical properties of bulk metallic glasses focuses on behavior at ambient temperature and at quasi-static strain rates. Second, no clear trend has been identified regarding the strain rate dependence of the mechanical behavior of bulk metallic glasses. As a matter of fact, different groups have reported largely different and sometimes even contradictory results. For example, negative strain rate sensitivity [65, 92], positive strain rate sensitivity [110, 98] and absence of strain rate dependence [7, 149] have all been claimed to be associated with bulk metallic glasses. Third, there is only sporadic data on the thermal (temperature) effect on the mechanical properties of bulk metallic glasses [105, 73, 123, 102]. Most of such data has been obtained at quasi-static strain rates [105, 73, 123]. Fourth, no elaborated effort can be found in the literature regarding the coupled effect of temperature and strain rate on the mechanical behavior of bulk metallic glasses.

Therefore, the primary objective of this dissertation is to provide a comprehensive investigation of the various aspects of mechanical properties of a few typical bulk metallic glasses, particularly the plastic deformation and flow characteristics of a Zr-based bulk metallic glass, $Zr_{55}Al_{10}Ni_5Cu_{30}$ over a wide range of strain rates and temperatures.

In Chapter 2 we will discuss the plastic deformation mechanism and the strain rate sensitivity of this Zr-based bulk metallic glass at room temperature. In Chapter 3, we will describe the investigation on the temperature and strain rate effect on the mechanical behavior of the bulk metallic glasses. In Chapter 4, we will report

nanoindentation experimental results on some BMGs, particularly on the strain rate sensitivity based on the instrumented nanoindentation experiments. Hardness evolution and the strain rate effect will be discussed in detail. In Chapter 5, a Hf-based metallic glass composite with tungsten particle reinforcement is tested at different strain rates, and the effect of the addition of W particles on the mechanical behavior of the Hf-based metallic glass is studied.

In what follows, we will provide a concise review on the major aspects of bulk metallic glasses, with a focus on the mechanical behavior, especially plastic deformation. A brief general historical background will also be given regarding the development of bulk metallic glasses.

1.2 Metallic Glasses

Generally speaking, when a metal liquid is cooled at a low rate, such as 1K/s, the crystallization process that will happen during the cooling stage, causes the material to form a long-range periodical structure, which is a crystalline material as we know it. But when an alloy is cooled down at a certain cooling rate, such that the crystallization process is suppressed, the nucleation and growth of the crystalline phase could be bypassed in the metal liquid during the cooling period. Figure 1 is a schematic drawing of a time-temperature-transformation (TTT) diagram of a metallic glass system. The slope of the green arrow indicates the critical cooling rate that the liquid can cool down quickly enough to bypass the nose on the TTT diagram for crystallization. If the cooling rate is faster than this critical cooling rate, the crystallization process will be suppressed and glass will form. In practice, the faster

the critical cooling rate, the easier it is to form metallic glasses. The T_l shown in the Figure 1 is the liquidus temperature, and the T_g is the glass transition temperature. The glass forming ability (GFA) describes the ability of a system to form glass state solid. Researchers have linked the GFA to some characteristic temperatures of the material and other physical properties. With the assumption that the nucleation frequency and the crystal growth of a melt scale inversely with the viscosity of the liquid, Turnbull [151] proposed the reduced glass transition temperature T_{rg} , defined as the ratio of the glass transition temperature to the liquidus temperature, T_l/T_g . Lu and his co-workers confirmed that the reduced glass transition temperature, T_{rg} shows a good correlation with the GFA. Another GFA indicator, i.e., the supercooled liquid region, ΔT_{xg} has been proposed by Inoue et al. [61]. The supercooled liquid region, defined as the difference between the onset temperature of crystallization T_x and the glass transition temperature T_g , is based on the stability of the supercooled liquid against crystallization.

In order to obtain alloy systems with excellent glass forming ability, a great deal of work has been undertaken in the community. Inoue [52] from Tohoku University has proposed three empirical rules for a system with high GFA: (1) more than three elements in the system; (2) large atomic size difference between major constituent elements; (3) negative heats of mixing of the major constituent elements. A system which satisfies these three empirical rules will result in an increase in the degree of dense randomly packed structure, and a liquid with new atomic configurations will form having a large solid/liquid interfacial energy; it is also difficult for the atoms to rearrange, and as such the crystallization process can be arrested. All these empirical

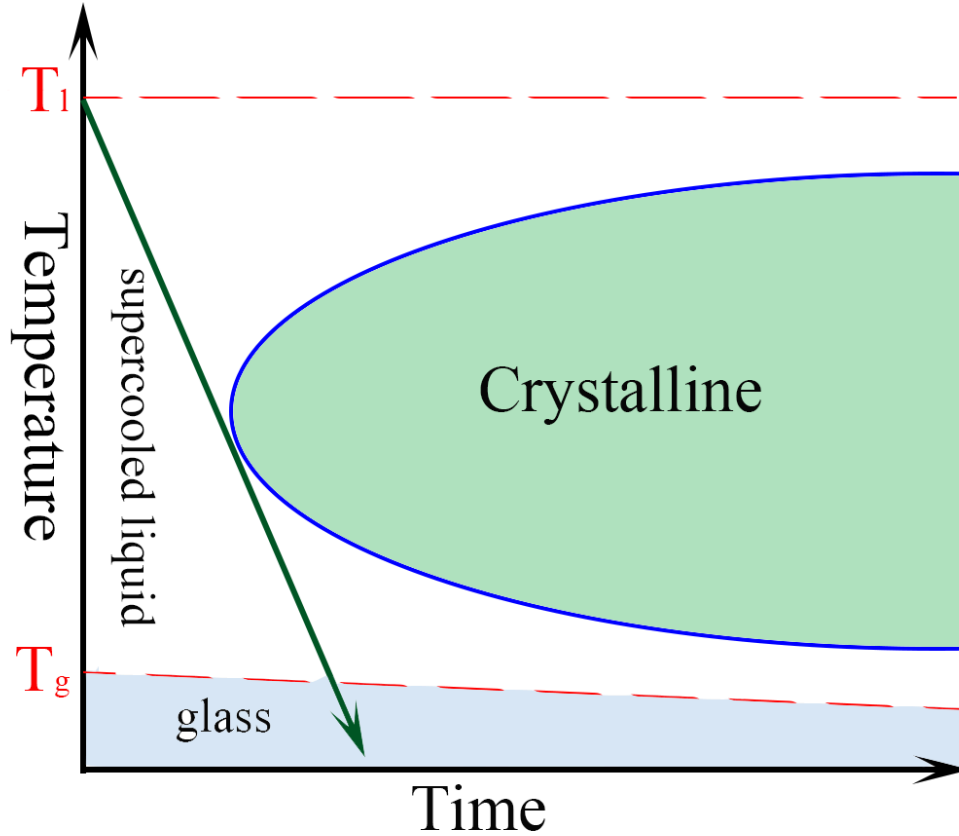


Figure 1: Schematic drawing of a TTT diagram of metallic glass system.

rules will increase the glass transition temperature which results in a higher value of T_{rg} , and thus better GFA.

Following the three empirical rules proposed by Inoue[52], a large number of studies on the formation and the properties of bulk metallic glasses have been performed in the past two decades. Numerous bulk metallic glass systems have been reported and the alloy systems can be classified as non-ferromagnetic and ferromagnetic alloys depending on their composition[58]. The non-ferromagnetic alloy systems include Ln-, Mg-, Zr-, Ti-, Pd-, Ca-, Cu-, Pt-, and Au-based systems, while the ferromagnetic group comprises of Fe-, Co-, and Ni-based alloy systems. The lowest critical cooling

rate for bulk metallic glasses reach as low as 0.067 K/s for a Pd-based bulk metallic glass system reported by Inoue et al.[124]. This low critical cooling rate is about 10^8 times smaller than those for other ordinary glassy alloys[60, 57, 66, 52]. With such a low critical cooling rate, production of large-scale metallic glass objects with different external shapes has been enabled. For example, Pd-Cu-Ni-P systems with over 70 mm in diameter and height have been reported by Inoue et al.[53] and over 20 mm in diameter, 40 mm in height for Zr-Al-Cu-Ni[59, 177], Cu-Zr-Al-Ag[181] and Ni-Pd-P-B[179] systems.

Despite the intense interest in glass forming ability and applications of bulk metallic glasses, many details about their structure remain a mystery. Although the bulk metallic glasses lack the long range order, and the local atomic configurations are completely different from those for the corresponding crystalline alloys, simulations and experimental efforts reveal that in metallic glasses there exist medium to short range order atomic structures[43, 143, 116]. Hirata and his co-workers[43] applied nanobeam electron diffraction to the Zr-Ni binary system. Experimental results suggested the existence of the short- and medium-range order atomic clusters inside the amorphous alloy. Molecular dynamics simulations have been conducted by Sheng et al.[143] with different metallic glass systems, and analysis of the local atomic configuration of the simulation results revealed a short- and medium-range order structure of the atoms. A dense cluster-packing model has been proposed by Miracle[116], which is based on coordination polyhedra. Ye et al.[176] performed high-frequency dynamic micropillar tests on a Zr-based bulk metallic glass system. The experimental results showed that loosely bonded atomistic free volume zones are enveloped by elastically

tightly bonded atomic clusters.

1.3 Mechanical Properties of Bulk Metallic Glasses

Because of the structural difference between metallic glasses and crystalline metallic alloys, BMGs exhibit attractive properties. The deformation behavior of bulk metallic glasses is characterized by either homogeneous or inhomogeneous deformation. According to deformation maps of the metallic glasses[135], inhomogeneous deformation usually occurs when a metallic glass is deformed at low temperature or high strain rate, and the plastic deformation is characterized by the formation of localized shear bands. Homogeneous deformation happens at high temperature and low strain rate, where the specimen deforms uniformly without any localized shear band formation.

For a polycrystalline solid, the yield criterion predicts the same magnitude in either tension or compression. In contrast, metallic glasses have an asymmetry of their tension and compression strengths, suggested by the different shear angles of the tested sample under tension and compression. The fracture angle in compression tests is less than 45° [28, 165, 91] while that angle is always larger than 45° in tension[91, 117, 96] tested sample. Donovan[28] argued that the yielding of metallic glasses obeys the Mohr-Coulomb criterion instead of the von Mises criterion. The yield stress of the metallic glasses depends not only on the applied shear stress, but also on the stress normal to the shear plane σ_n . And the criterion can be written as follows:

$$\tau_y = \tau_0 + \alpha\sigma_n \quad (1)$$

co-workers[50] also reported that the failure strength of $Zr_{57}Ti_5Cu_{20}Ni_8Al_{10}$ bulk metallic glass decreased with increasing strain rate. Li et al.[92] also reported the same strain rate effect for $Hf_{52.5}Ti_5Ni_{14.6}Cu_{17.9}Al_{10}$ bulk metallic glass. The stress drop at high strain rate was attributed to the formation of multiple shear bands at the same time when the rate of shear band emission is not sufficiently fast to accommodate the applied strain rate. In contrast, Lu et al.[105] and Bruck et al.[7] reported that the compressive fracture strength of $Zr_{41.2}Ti_{13.8}Cu_{12.5}Ni_{10}Be_{22.5}$ bulk metallic glass was independent of the imposed strain rate. Liu and his co-workers[98] reported a positive strain rate sensitivity for $Nd_{60}Fe_{20}Co_{10}Al_{10}$ bulk metallic glass system. Data of the compressive fracture strength as a function of strain rate from different researchers[118, 50, 92, 105, 7, 98, 184] are summarized in Figure 2. It is apparent that the strain rate dependence of the strength in bulk metallic glass is still controversial. There are few detailed discussions about the strain rate effect on the strength of bulk metallic glasses in the literature.

1.3.2 Strength and Plasticity

The strength and the ductility of bulk metallic glass are the two mechanical properties of major concern for structural applications. Johnson and Samwer[68] concluded that the typical elastic limit of a bulk metallic glass is about 2%, and therefore, the critical shear strength is about 0.02μ (where μ is the shear modulus of the metallic glass). After further investigation of 30 different bulk metallic glass systems, Johnson and Samwer[68] found that the critical shear strength of a BMG is related to the physical parameters associated with the atomic cohesive energy, such as the glass

transition temperature T_g and shear modulus μ . Inoue and his co-workers[54] also reported that the strength of BMG relates to the elastic modulus of the specimen. Since the T_g is the key parameter controlling the glass forming ability of the amorphous alloy system[106], the relationship between the strength and T_g has drawn particular interest. The strength of bulk metallic glasses is found to relate to the composition of the alloy. Different compositions of an alloy system have different glass transition temperatures, which will produce different strengths. Yang et al.[174] have concluded that the strength of a bulk metallic glass depends on T_g , testing temperature T , and the molar volume V , and can be expressed as

$$\sigma_f = 55 \frac{T_g - T}{V} \quad (2)$$

Experimental results from different researchers[180, 140, 133, 178, 109, 56, 118, 157, 8, 182, 107] also suggest that the strength of the BMG at room temperature depends on the glass transition temperature and the molar volume.

Because of the absence of crystal-slip mechanisms in bulk metallic glasses, they exhibit very high strengths which can be close to the theoretical limit[39], but their ability to deform plastically is very limited. In uniaxial tension, the plastic strain is near zero[171]. Even under a compressive load, the plastic strain is still limited. In order to increase the ability of the BMG systems to deform plastically, researchers have reported different systems with large plastic strain under compression and bending tests[171, 131, 25, 103]. Lewandowski et al.[89] have proposed a universal correlation between the toughness and the elastic modulus ratio μ/B (B is the bulk modulus). A

solidity index $S = \mu/B$ is used to distinguish a ductile solid from a brittle one. The higher the value of S , the more brittle of the material. A transition from ductile to brittle has been found when $S > 0.41 - 0.43$ [89]. Since metallic glasses are isotropic materials, the solidity index can be expressed as

$$S = \frac{3(1 - 2\nu)}{2(1 + \nu)} \quad (3)$$

where ν is the Poisson's ratio. The above equation indicates that a low solidity index corresponds to a high Poisson's ratio. In other words, bulk metallic glasses with high Poisson's ratio is more ductile. A high Poisson' ratio can promote multiple shear band formation, and as such, crack initiation can be suppressed[40, 131]. It is also reported that the higher the Poisson's ratio, the larger the shear transformation zone volume, and a relatively large STZ volume reinforces the shear capability of the metallic glass and promotes the formation of multiple shear bands[128].

1.3.3 Size Effect

The plastic deformation of bulk metallic glasses is a process through shear transformation zones, and the dimension of a STZ is about 1 nm[128], which is significantly smaller than the length scales of the samples in conventional mechanical testing. In this context, one could argue that the mechanical properties of metallic glasses are relatively size-independent. However, Schuh et al.[138, 135] suggested that the critical nucleus of a shear band has a diameter of $\sim 50 - 500$ nm, which indicates that a size dependence of the mechanical behavior of BMGs could exist when the specimens approach this size. Size dependence of the mechanical behavior of BMGs has

been found even at the mm-scale region[168, 166, 49, 170, 94]. The strength and the malleability of the BMGs depend on the specimen size. The smaller size specimens experienced a faster cooling rate during the solidification, which created more preferential nucleation size for shear band[49].

Size-dependent strength and deformation modes of micro- and nano-scale specimen of metallic glasses are also reported[155, 139, 41, 63]. A change in deformation mode in the smallest metallic glass specimens has been reported in tension[41, 63] and also in compression[155]. However, Schuster and his co-workers[139] have shown that the plastic flow of BMG in compression is always localized in shear band, and there is no deformation mode change even when the specimen diameter is only $\sim 250\text{nm}$, or smaller[169]. The deformation mode change observed in other reports are attributed to the geometrical effect of the tapered shapes of the micro-pillar specimens[139, 99]. A correlation between the reduced specimen size and the strength of bulk metallic glasses is also reported[139, 155, 83].

Although a number of efforts regarding the mechanical properties of metallic glasses have been undertaken in the past two decades, due to the lack of an accurate structural model and the experimental difficulties in investigating a disordered system, the relationship between the properties and the amorphous structure has not been well clarified theoretically. Nevertheless, a wide range of excellent properties of metallic glasses have been measured and the potential application have been summarized in Table 1 based on the work of Wang et al.[158].

Of all the properties of bulk metallic glasses, mechanical properties have attracted the most interest from researchers. In Figure 3[4] we have plotted the elastic limit

Table 1: Fundamental properties and potential applications of bulk metallic glasses.

| Properties | Application field |
|--|---------------------------------|
| High strength | Machinery structural materials |
| High hardness | Cutting materials |
| High fracture toughness | Die materials |
| High impact fracture energy | Tool materials |
| High fatigue strength | Bonding materials |
| High elastic energy | Sporting goods materials |
| High corrosion resistance | Corrosion resistance materials |
| High wear resistance | Writing appliance materials |
| High reflection ratio | Optical precision materials |
| High hydrogen storage | Hydrogen storage materials |
| Good soft magnetism | Soft magnetic materials |
| High frequency permeability | High magnetostrictive materials |
| Efficient electrode | Electrode materials |
| High viscous flowability | Composite materials |
| High acoustic attenuation | Acoustic absorption materials |
| Self-sharpening property | Penetrator |
| High wear resistance and manufacturability | Medical devices materials |

against Young's modulus, E , for different metallic materials. Also σ_y/E and σ_y^2/E are plotted, in which the first is the yield strain and the second is the ability of the material to store elastic energy. The figure reveals that metallic glasses have excellent properties compared to other materials. The high yield strength, and in turn, the high elastic strain limit have made bulk metallic glasses attractive for many engineering applications.

Although the elastic limit and the yield strength of metallic glasses are much higher than most of the conventional alloys, limited macro-plasticity has been reported in uniaxial compression and tension in metallic glasses at room temperature and high stress levels. It is widely recognized that the plastic deformation of metallic glasses is primarily accommodated through the formation of localized shear bands. The rapid propagation of the shear band results in catastrophic failure of the sample. The

plastic strain of the BMGs is limited to be less than 2% by shear banding and shear band propagation processes.

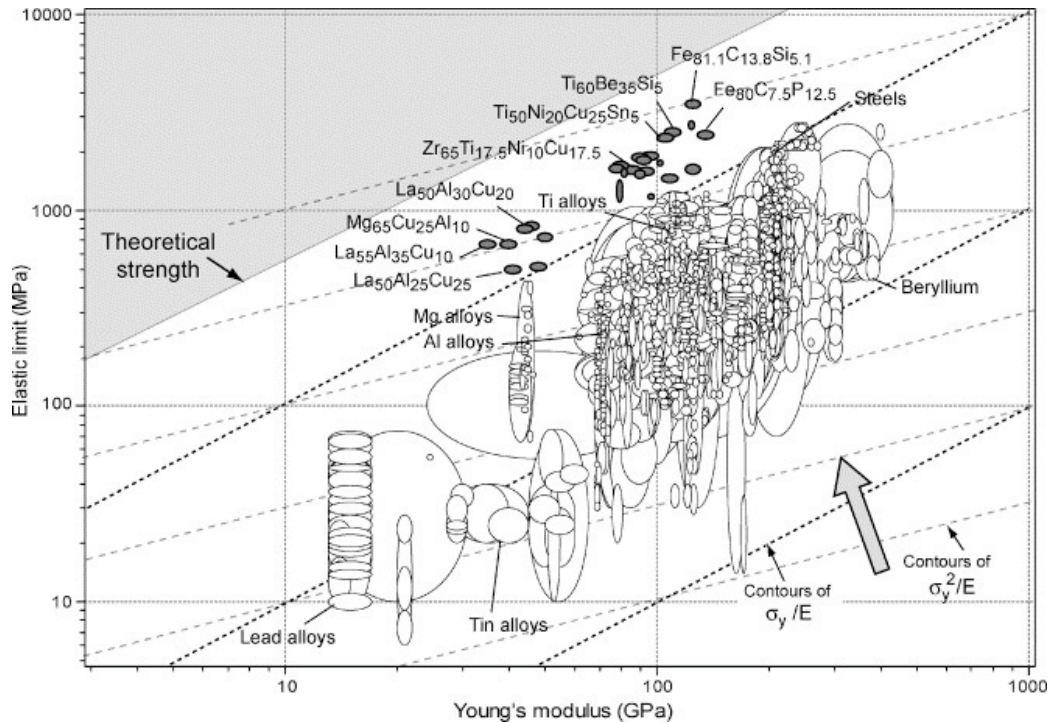


Figure 3: Elastic limit σ_y is plotted against elastic modulus E for 1507 metals, metal matrix composites and metallic glasses. The contours show the yield strain σ_y/E and the resilience σ_y^2/E [4].

1.4 Zr-Based Bulk Metallic Glass

The material that will be investigated in this dissertation is primarily a Zr-based bulk metallic glass, $Zr_{55}Al_{10}Ni_5Cu_{30}$. Materials were provided by Professor Chaoli Ma from Beijing University of Aeronautics and Astronautics (Beihang University). The composition is given by the nominal atomic percentage. The materials are made with copper mold casting method. The alloy ingots were prepared by arc melting the mixture of the Zr(99.99 mass%), Al(99.99 mass%), Ni(99.99 mass%), Cu(99.99 mass%) in an Ar atmosphere. The molten alloys are melted repeatedly for several

Table 2: Physical and mechanical properties of $Zr_{55}Al_{10}Ni_5Cu_{30}$ bulk metallic glass.

| $T_g(K)$ | $T_x(K)$ | $\rho(g/cm^3)$ | $E(GPa)$ | $G(GPa)$ | $H_v(GPa)$ |
|----------|----------|----------------|----------|----------|------------|
| 693 | 768 | 6.84 | 89 | 32.1[51] | 5.2 |

times to ensure a compositional homogeneity. Then the molten alloy is poured into a copper mold. The alloy will solidify quickly because of the rapid heat extraction by the metal mold. The details of the copper mold casting method can be found in the publication of Inoue et al.[55].

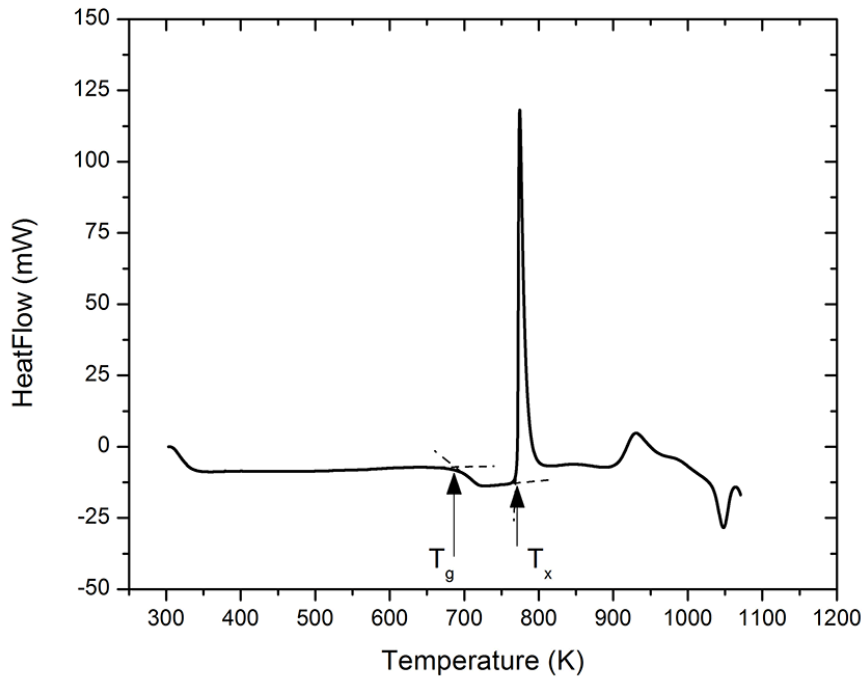


Figure 4: Differential scanning calorimetric (DSC) curves taken from $Zr_{55}Al_{10}Ni_5Cu_{30}$ with a heating rate of 20K/min.

The characteristic temperatures associated with the crystallization reaction of the Zr-based bulk metallic glass, for example the glass transition temperature (T_g) and the onset crystallization temperature (T_x), have been identified by differential scanning calorimetric (DSC) measurements. The DSC measurement was implemented at a

constant Ar flow of 50ml/minute. Figure 4 is the DSC curve of $Zr_{55}Al_{10}Ni_5Cu_{30}$ with a heating rate of 20K/min. Due to the glass transition, the sample shows a distinct endothermic reaction and an exothermic reaction due to crystallization. The glass transition temperature, T_g , and the crystallization temperature, T_x are measured to be 693 and 768K, respectively. The physical and mechanical properties of the as-cast $Zr_{55}Al_{10}Ni_5Cu_{30}$ bulk metallic glass are summarized in Table 2. The as-received rod samples have a diameter about 3mm.

CHAPTER 2: UNIAXIAL COMPRESSIVE BEHAVIOR OF BULK METALLIC GLASSES AT ROOM TEMPERATURE

2.1 Introduction

Excellent mechanical behavior is one of the most important requirements for structure material. Bulk metallic glasses have been considered for structural applications in many critical areas[4]. Although the first metallic glass had been discovered in the 1960s by Klement et al. [79], the first mechanical characterization on metallic glass materials had not been performed until 1970s. For example, Masumoto and Maddin carried out some mechanical testing on $Pd_{80}Si_{20}$ glass ribbons over a wide range of temperature[112]. Since that time, the mechanical properties of metallic glasses have attracted a great amount of interest and attention from researchers in the communities of materials science and engineering at large. In general, high fracture strength and limited or vanishingly small tensile ductility have been associated with metallic glasses in earlier research efforts. Inhomogeneous plastic deformation at room temperature and below through the formation of very narrow shear bands has been revealed as the main deformation mechanism responsible for plasticity. A number of theories and models have been proposed to explain the plastic deformation behavior. However, due to the limited size of the ribbon shaped samples and the ill-controlled stress state during mechanical testing, no strong experimental validation has been found for these theories and models. As such, whether these theories could be supported by ex-

perimental observations remained an outstanding question for quite some time. The successful synthesis of bulk metallic glasses have provided good opportunities for researchers to understand this category of structure material much better, particularly in the contexts of mechanical behavior, plastic deformation mechanisms, and failure mode. Extraordinary mechanical properties such as very high fracture strength, large elastic strain (because of the relatively small elastic moduli), great wear resistance and excellent formability in the super-cooled temperature region [26, 58, 66, 81, 135] have made bulk metallic glasses promising candidates as structural materials for some important applications [4]. Great progress has been made during the past few decades both in the fabrication of large size metallic glass materials (i.e., bulk metallic glasses -BMGs) and in the understanding of the various aspects of their behavior, such as thermal, mechanical and chemical properties [9, 10, 11, 158]. For many structure materials, it is required that they have the ability to maintain their good mechanical properties over a relatively wide window of loading rates or strain rates. However, to the knowledge of the author, the strain rate dependence of BMGs has been an area that still awaits exploration. Only a few reports are available in the literature that deal with the high strain rate behavior and the strain rate dependence behavior of BMGs [7, 50, 64, 98, 102, 105, 110].

Usually, for a visco-plastic material, the strain rate dependence of the strength is defined by the strain rate sensitivity parameter as follows [160] :

$$m = \frac{\partial \log \sigma}{\partial \log \dot{\epsilon}} \quad (4)$$

In this definition, σ is the stress and $\dot{\epsilon}$ is the imposed strain rate in s^{-1} .

According to the results published by different researchers, the relationship between strain rate and the yield strength or fracture stress is still unclear for BMGs. For example, Bruck et al. [7] and Sunny et al. [149] have found that the yield strength was independent of the strain rate for Zr-based metallic glasses. However, Ma et al. [110] and Liu et al. [98] have reported a positive strain rate sensitivity for Ti-based and Nb-based metallic glasses. Hufnagel et al. [65] and Li et al. [92] have shown the yield strength of Zr-based metallic glasses to decrease with increased strain rate.

The conflicting experimental results on the strain rate dependence of BMGs suggest that the effect of strain rate on the yield strength of bulk metallic glasses is still a controversial issue. What is more, a commonly accepted theory is lacking for such rate dependence behavior of BMGs.

In order to obtain a better understanding of the nature of the deformation mechanism at relatively high strain rates ($\sim 10^3 s^{-1}$), and of the strain rate dependence of BMGs, in this work we have investigated the quasi-static and dynamic behavior of Zr-based and Hf-based metallic glasses. We have used uni-axial compressive loading to examine the mechanical behavior at various strain rates. The strain rate dependence of these BMGs has been discussed from an energetics point of view.

2.2 Materials and Experimental Procedure

Four different BMGs of compositions $Zr_{57}Ti_5Cu_{20}Ni_8Al_{10}$, $Zr_{52.5}Ti_5Cu_{17.9}Ni_{14.6}Al_{10}$, $Hf_{52.5}Ti_5Cu_{17.9}Ni_{14.6}Al_{10}$ and $Zr_{55}Al_{10}Ni_5Cu_{30}$ were prepared using melt-suction casting method [50]. The as-cast cylindrical rods were cut into samples with dimensions

$\Phi 3 \times 6 \text{ mm}$ for quasi-static and $\Phi 3 \times 3 \text{ mm}$ for dynamic loading using electrical discharge machining. The loading surfaces of the specimens were well polished to ensure the parallelism of the two faces. Quasi-static uniaxial compression tests were conducted on a servo-hydraulic MTS system using displacement control to ensure $1 \times 10^{-3} \text{ s}^{-1}$ strain rate.

Kolsky bar (or Split-Hopkinson pressure bar) technique was used to measure the dynamic compressive properties of the BMGs. High strain rate in the order of $\sim 10^3 \text{ s}^{-1}$ was reached during the tests. Figure 5 provides a schematic of the Kolsky bar system used in this work. In these high-strain rate experiments, the specimen is sandwiched between the input bar and output bar with two WC platens. A projectile is launched by pressurized gas to strike one end of the input bar so as to produce a stress wave that travels down the input bar. When the stress wave arrives at the interface between the specimen and the platen, part of the wave will be reflected back into the input bar, and part of the wave will be taken up by the specimen to cause deformation or failure of the specimen. A few reverberations of the stress wave within the specimen will eventually lead to equilibrium condition. Another part of the wave will transmit through the specimen to the output bar. Strain gages are attached to the input and output bars to measure the wave signals which are recorded with an ultra-fast, multiple-channel oscilloscope through a wheatstone bridge to amplify the wave signal. Wave signals can be used to analyze the stress and strain information of the samples. As demonstrated by Figure 6, it is a typical strain-gage signal from a compressive Kolsky bar test of metallic glass. The input wave, transmitted wave and reflected wave are marked in the figure. After applying the strain gage factor

and the wheatstone bridge input voltage to the wave signals, the input, transmitted and reflected waves can be denoted as ε_i , ε_t , and ε_r . Then the engineering stress and engineering strain can be calculated based on those waves by the following equations.

$$\sigma_E = \frac{A_0 E_0 \varepsilon_t}{A} \quad (5)$$

$$\varepsilon_E = \int_0^t \dot{\varepsilon} dt = \int_0^t \frac{2c_0 \varepsilon_r}{L} dt \quad (6)$$

where the A_0 and E_0 are the cross section area and the elastic modulus of the bar respectively; A is the cross section area of the specimen; c_0 is the wave velocity travelling through the bar and L is the length of the specimen. The details of the working principles and data processing methods can be found in a recently published monograph [12]. Brief descriptions of the Kolsky bar technique can be found in Refs. [36, 120]. The ends of the bars, the platens and the loading faces of the specimens have all been carefully conditioned to avoid unwanted stress concentrations during high strain rate loading of the specimens. The post-loading specimens were examined with scanning electron microscopy (SEM) to identify the deformation and fracture mechanisms of those BMGs.

In order to access the materials behavior over a wide range of strain rates, an MTS hydro-servo machine was used to examine the mechanical properties at various quasi-static strain rates for the $Zr_{55}Al_{10}Ni_5Cu_{30}$ bulk metallic glass. The strain rate range is set up from $5 \times 10^{-5} s^{-1}$ to $1 \times 10^{-2} s^{-1}$. Tungsten carbide platens were used during the compression experiments to protect the cross heads from damage.

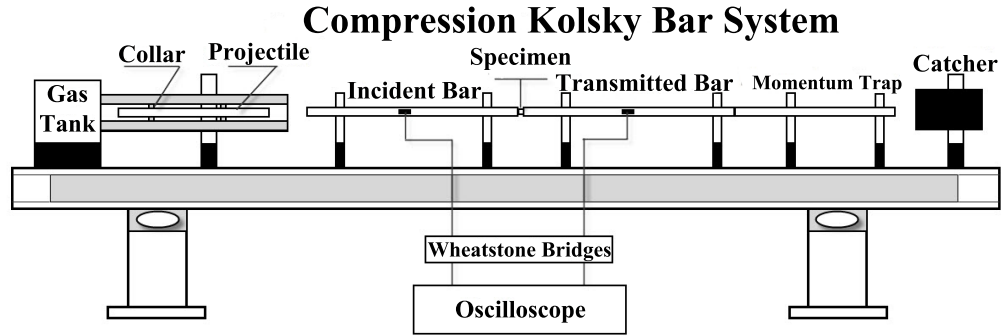


Figure 5: Schematic of the Kolsky bar system for the high-strain-rate mechanical testing. The projectile, input bar, output bar and the momentum trap are all made of the same ultra-strong maraging steel with the same diameter of 7.86mm . A heating unit is also attached to this system to investigate the coupled thermal and strain rate effect on materials mechanical behavior.

2.3 Experimental results

Figure 7 shows the typical quasi-static and dynamic compressive true stress-strain curves for the four different metallic glasses. From the quasi-static curves, we can see that some of the metallic glasses deform elastically to 2% elastic strain, followed by plastic flow without any strain hardening. In other words, nearly elastic-perfectly-plastic behavior has been observed from the quasi-static stress-strain curves. The plastic part of the stress-strain curves exhibits serrated flow, which suggests the formation of multiple shear bands during quasi-static compressive loading. In contrast, all the dynamic stress-strain curves show that the specimens fracture right after the elastic deformation, and the plastic strain is almost zero. The dynamic stress-strain curves shown in this work are similar to those reported by Hufnagel et al.[50] and Bruck et al.[7]. The experimental results of the uniaxial quasi-static and dynamic compressive tests presented in Figure 7 indicate that the dynamic fracture strength is lower than that under quasi-static loading condition for each individual BMG. The

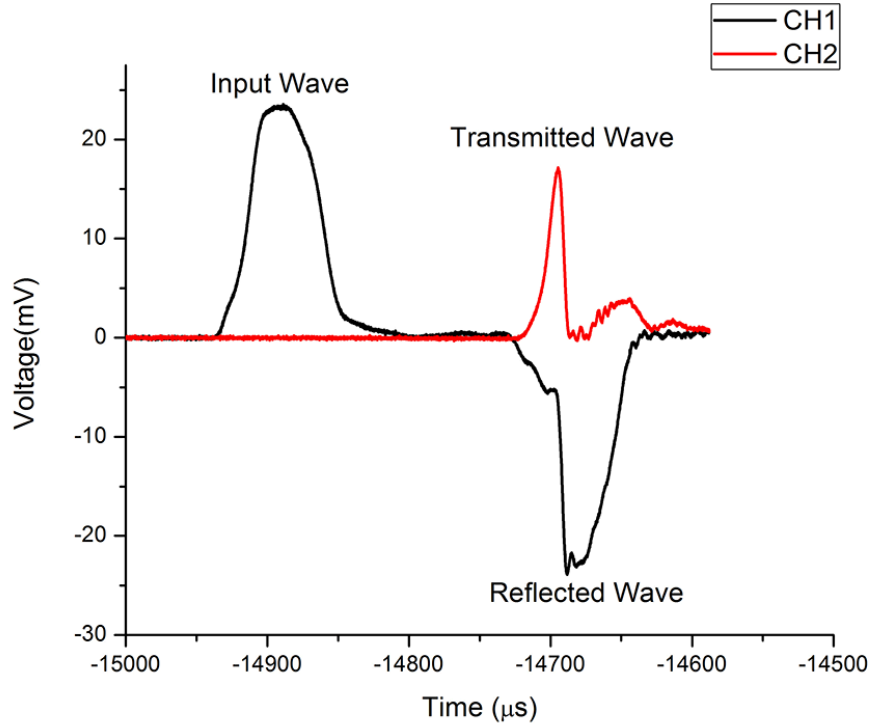


Figure 6: A typical strain-gage data after signal conditioning and amplification from the compressive Kolsky bar experiment of metallic glasses showing the three stress waves measured as a function of time.

strength has dropped by 10-20% under dynamic loading, suggesting a negative strain rate sensitivity for these BMGs under uniaxial compressive loading.

Post-loading specimens were examined by SEM to reveal the deformation and fracture mechanisms. Figure 8 shows the fracture angle of post-loading metallic glass ($Zr_{55}Al_{10}Ni_5Cu_{30}$) under quasi-static compressive loading condition. The angle is measured between the fracture surface and the loading axis. The angles from all the quasi-static fracture surfaces are measured to be about 41° . On the other hand, under dynamic uniaxial compression, no constant value for the fracture angle can be identified. Figure 9 shows the fracture surface of a quasi-static post-loading BMG specimen ($Zr_{55}Al_{10}Ni_5Cu_{30}$). We can see that the fracture surface is quite flat (Fig-

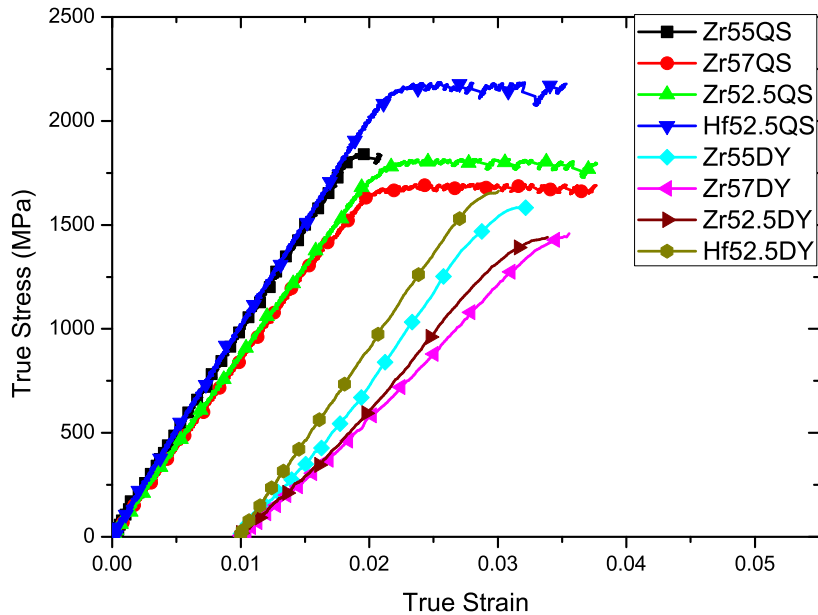


Figure 7: Quasi-static (QS) and dynamic (DY) uniaxial compressive stress-strain curves of three different metallic glasses. The dynamic curves are offset with 1% strain for a better view. Serration in plastic flows have been observed from some of the QS curves. For the dynamic experiments, specimens have failed right almost immediately after elastic deformation. Notice the lower strength under dynamic loading vis-à-vis the quasi-static loading.

ure 9 (a)) and the vein-like pattern is uniformly distributed (Figure 9 (a)). There is an apparent flow direction of the vein-like pattern which is also reported by other researchers[183]. Compared to the quasi-static specimen, the fracture surface of the dynamic sample is more uneven, as is shown by Figure 10(a) for a dynamic specimen of the same BMG material ($Zr_{55}Al_{10}Ni_5Cu_{30}$). Figure 10(b) shows that the distribution of the veinlike pattern is non-uniform. Also, there is no obvious flow direction of the vein-like pattern. Evidence for numerous areas that have probably gone through melting is visible on the fracture surfaces of the dynamically loaded specimens. Some of such areas are marked by arrows in Figure 10(b). Such evidence suggests that

very significant temperature rise has taken place locally in the specimen during the dynamic loading. These observations are in line with the experimental results of Refs. [102, 184]. Under both quasi-static and dynamic loading conditions, light emissions were observed from the samples.

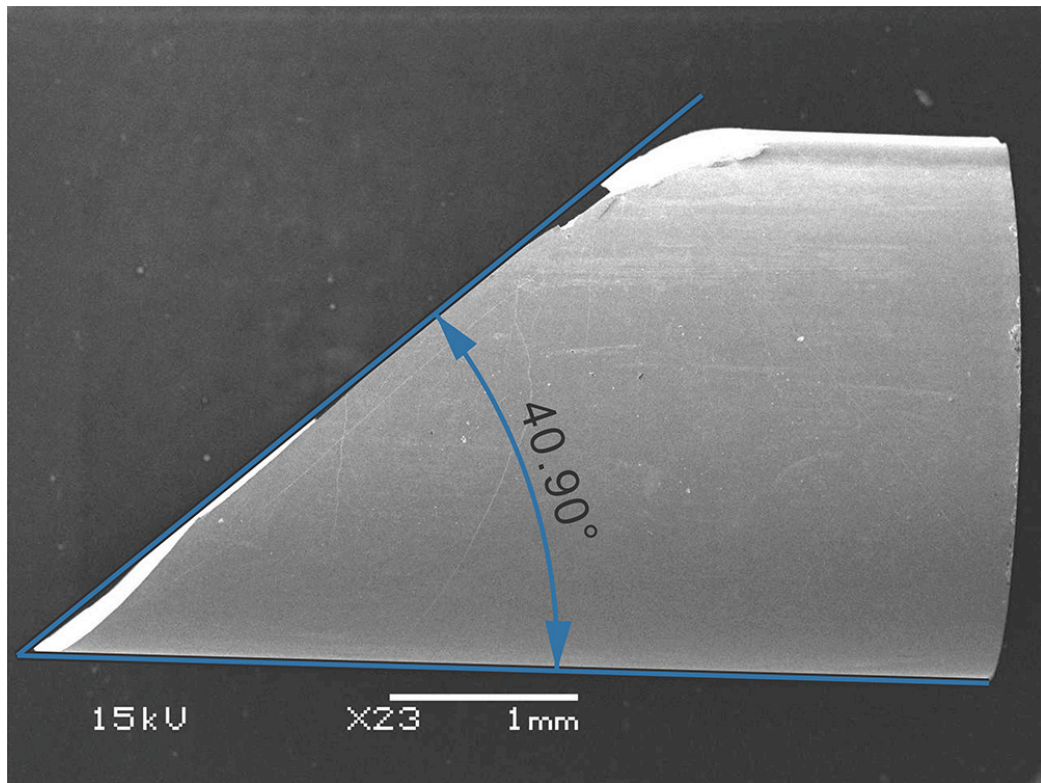


Figure 8: The fracture surface angle of the $Zr_{55}Al_{10}Ni_5Cu_{30}$ bulk metallic glass tested under quasi-static compressive loading condition. Loading is approximately horizontal. It shows that the fracture angle (the angle between the fracture plane and the loading axis) is measured to be 40.90° . See the text for discussion on the significance of this fracture angle.

In order to assess the mechanical behavior, particularly the strain rate dependence of BMGs over wider strain rate window, we have measured the compressive behavior of the $Zr_{55}Al_{10}Ni_5Cu_{30}$ bulk metallic glass at different strain rates. The strain rate is controlled by the speed of the cross head displacement of the MTS machine. The fracture stresses of $Zr_{55}Al_{10}Ni_5Cu_{30}$ together with those of the other three bulk

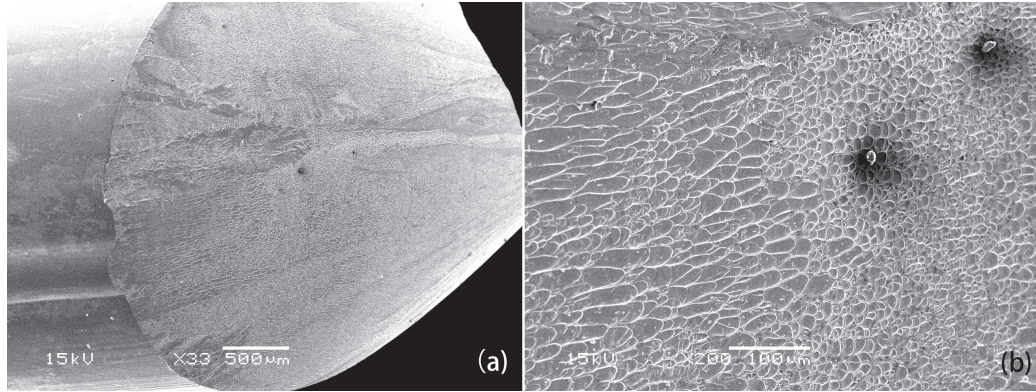


Figure 9: Post-quasi-static loading images of a representative sample (Zr₅₇Ti₅Cu₂₀Ni₈Al₁₀). (a) Low-magnification, overview of the fracture surface, showing a relatively flat fracture surface with a uniform distribution of the vein-like pattern; (b) the enlarged view of the vein-like pattern showing a clear flow direction without any obvious evidence of local melting.

metallic glasses are plotted versus the strain rate in Figure 11. From the results presented in this figure, we can see that the fracture strength of tested bulk metallic glasses increases with increasing strain rate within the quasi-static region. But when the strain rate is increased into the dynamic region, the fracture strength decreases.

In summary, our experimental results show that within the quasi-static loading rate regime, the BMGs investigated in this work all exhibit positive strain rate dependence. That is, the strength increases with the imposed strain rate. However, under dynamic loading, the strength of these BMGs decreased compared to the quasi-static strength. Such behavior calls for a consistent interpretation.

2.4 Discussion

2.4.1 Serrated flow under quasi-static compressive uniaxial compression

During uniaxial compressive experiment at a constant displacement rate, the loading rate is a non-linear function of time, which leads to the stress serration after

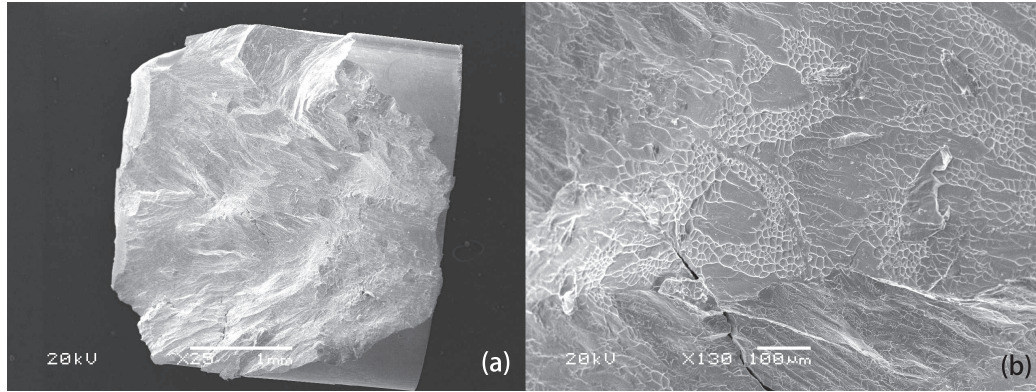


Figure 10: Post-dynamic loading images of a representative sample (Zr57Ti5Cu20Ni8Al10). (a) Low magnification, overview of the fracture surface, revealing uneven fracture surface with scattered vein-like pattern; (b) the enlarged view of the vein-like pattern showing no clear flow direction.

yielding as shown on the true stress-strain curves (Figure 7). Each serration during the experiments corresponds to the formation of a shear band. There are many prior reports about the serration of flow during the mechanical loading of metallic glasses. For example, Kimura and Masumoto[78] have studied the serration flow during compressive loading of Pd-16Si-6Cu metallic glass, and they found the serration amplitude ($\delta\sigma$) was related to the strain rate. Wright et al.[165] also reported the load serration during the compressive test of a Zr-based bulk metallic glass.

In order to find out where on the stress-strain curve the first stress serration occurred during the compressive experiments, the load-time history was investigated. The earliest or the first load serration was found during the lowest strain rate ($5 \times 10^{-5} s^{-1}$) compression with stress at around 1500MPa as shown in Figure 12(a). This stress value is much lower than the flow stress shown on the stress-strain curve. It is also found that the first load serration happens at different point at different strain rate. As shown in Figure 12(b), the true stress corresponding to the first load ser-

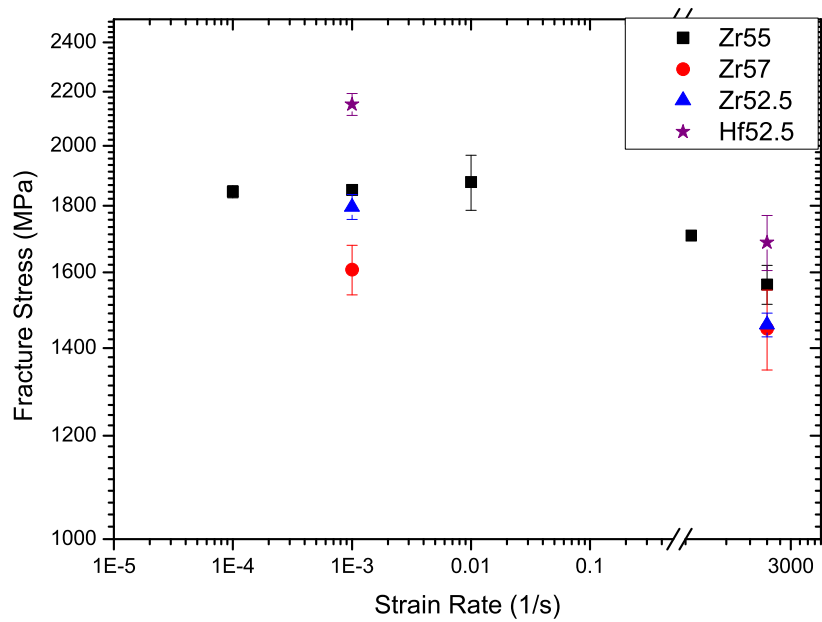


Figure 11: The fracture strength of four different bulk metallic glasses versus the imposed strain rate. The strain rate axis is plot as logarithmic scale. It can be seen that for the Zr55 specimen which has been tested over a wide range of strain rate, a positive strain rate sensitivity is identified within the quasi-static strain rate window, while high strain rate strength is lower than all the quasi-static strength values, indicating a negative strain rate dependence in the dynamic loading regime.

ration is plotted as a function of the imposed strain rate. It should be advised that in this figure, both axes are in logarithmic scale. It is found that the value of the stress at the first load serration increases with increased strain rate. But, this trend does not suggest the serration happens at higher stress when strain rate is high; the disappearance of the serrated flow at low stress state with high strain rate is because the local strain rate during the serration is less than the imposed strain rate, and the load jump is overcome by the imposed strain. Schuh et al.[132] have reported the flow serration that happened at lower loading rate during the nanoindentation tests, but a continuous load-displacement curve was observed when the loading rate was

high. Kimura and Masumoto[78] also reported that the load serration was completely suppressed when the imposed strain rate is higher than $3 \times 10^{-2} s^{-1}$.

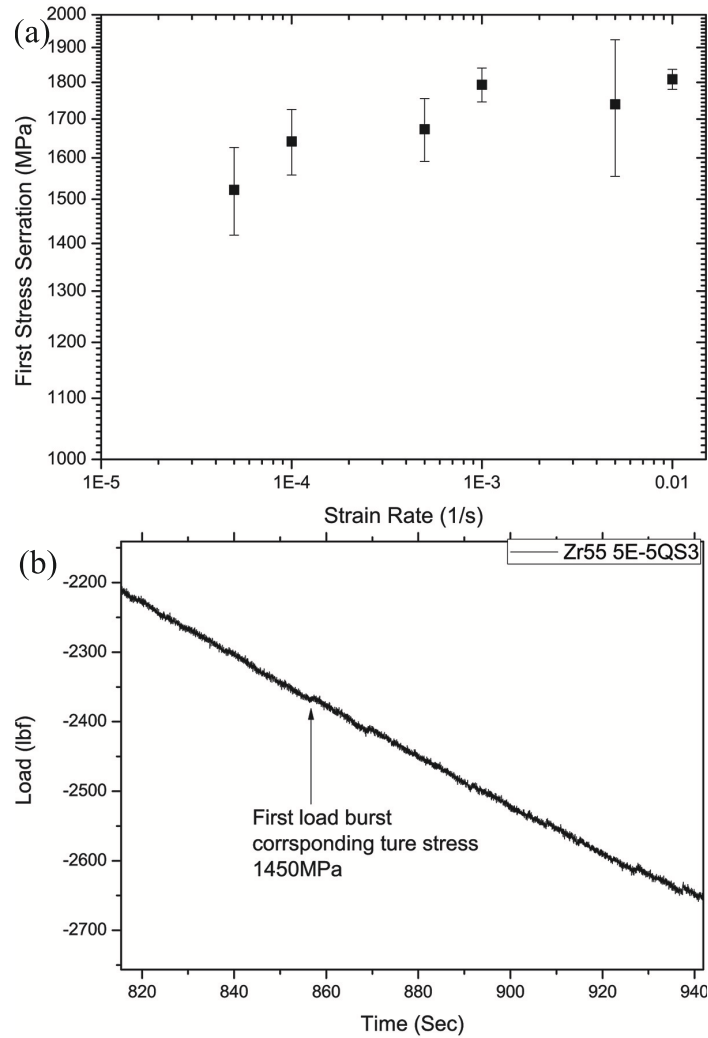


Figure 12: (a) The first load serration during the quasi-static compressive experiment at a strain rate of $5 \times 10^{-5} s^{-1}$. The corresponding true stress at this first load serration (or load drop) is 1450MPa. (b) The true stress corresponding to the first load serration vs. the imposed strain rate. The true stress and strain rate are both plot in logarithmic scale.

Figure 13 is a typical compressive true stress-strain curve at a strain rate of $5 \times 10^{-4} s^{-1}$. The maximum stress was measured to be about 1.8GPa, and this value of σ_{max} agrees with the fracture strength reported in the literature[69] for the same

material. If we enlarge the yield section of the stress-strain curve, it then shows that the curve bends after it passes the elastic limit, and the yielding occurs at a lower stress level which is about the value corresponding to the first load serration. According to Song et al.[144], the flow serration in bulk metallic glasses can be divided into two stages, and the intersection of the extended elastic curve and the stress plateau is used to represent the demarcation line between the two stages. Notice that the bend in the stress-strain curve from stage 1 to stage 2 in Figure13 was not caused by any strain hardening mechanism, but is because of the formation of shear bands. The investigation of the relative displacement-time curve of the Zr-based bulk metallic glasses has been summarized by Figure 14. Experimental results show that the transition from stage 1 to stage 2 always takes place at the same strain, $\varepsilon \sim 0.019$, which is independent of the imposed quasi-static strain rate. In the left hand side of Figure 14, we have plotted the displacement bursts versus the strain, where the dash line was drawn to indicate the separation of stage 1 from 2. In the right hand side of Figure 14, we have plotted the offset speed for each displacement burst event, and the unit is $\mu m/s$. Here a dash line was also drawn to indicate the stage 1 and 2. The displacement burst was found to increase with increasing strain, and the burst size is independent of strain rate. The magnitude of the displacement bursts ranges from 0 to $\sim 4\mu m$. This measurement results agrees with measurements provided in Ref.[144]. We should point out here that although the trend is almost the same for the displacement burst size at different strain rates, the population of the displacement bursts is reduced in stage 1 with increasing strain rate. With the highest strain rate($1 \times 10^{-2} s^{-1}$), displacement burst has almost disappeared in stage 1. As we

have discussed previously, with increasing strain rate, the first loading serration takes place at a higher stress level, and this is caused by the higher speed of the cross-head during the compressive loading process. At a strain rate $\dot{\epsilon} = 1 \times 10^{-2} s^{-1}$, the speed of the cross-head is about $60 \mu m/s$, which is equivalent to the displacement burst speed of the individual shear band in stage 1 shown in the left hand side of Figure 14 with a lower strain rate.

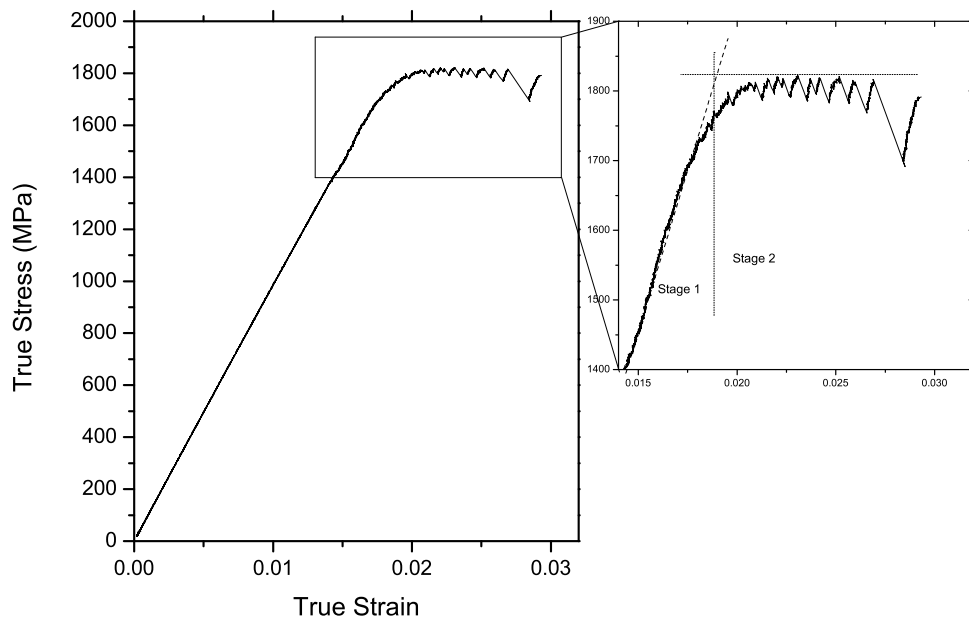


Figure 13: True stress-strain curve for the Zr-based BMG under uniaxial compression at a strain rate $5 \times 10^{-4} s^{-1}$. Serrated flow is obvious. The plastic portion of the stress-strain plot has been enlarged in the right hand side plot to see the flow serration more clearly.

The shear band propagation speed is calculated based on the displacement-time curves, and all the values are plotted in the left hand side of Figure 14. It clearly shows that, when the strain rate is low, the speed of the shear band propagation was around $100 \mu m/s$, which is lower than the speed of $800 \mu m/s$ measured by Song et

al.[144]. But at the highest quasi-static strain rate we have attempted, the largest displacement burst has a speed of $5000\mu m/s$, and this value is comparable to the speed measured by high-speed camera[146].

To further understand the deformation mechanism during the quasi-static compressive loading of bulk metallic glasses, the adiabatic temperature rise caused by the serrated flow and the fracture process needs to be discussed. The temperature rise caused by the plastic shear during the compressive loading can be calculated by the following formula[90, 23]:

$$\Delta T = \frac{\Delta\tau\dot{v}}{\lambda} \sqrt{\frac{\alpha\Delta t}{\pi}} \quad (7)$$

In the above equation, \dot{v} is the velocity of the plastic shear displacement. Since the angle between the shear band and the loading axis is about 41° , the value of \dot{v} in this equation should equal to $\cos(41)$ times the speed values in the left hand side of Figure14. λ is the thermal conductivity (in $Wm^{-1}K^{-1}$) and α is the thermal diffusivity(in m^2s^{-1}), and Δt is the escape time of an individual serration. The thermal conductivity can be represented as $\lambda = \alpha\rho c_p$, where ρ is the density of the metallic glass, which from Table 2, for the Zr-based metallic glass is $6.84g/cm^3$, c_p is the specific heat estimated to be $380Jkg^{-1}K^{-1}$ for Zr-based BMGs[23]. Table 3 has listed the temperature increase during the serrated flow corresponding to different strain rates. Calculation results of the temperature change show that the temperature effect during the shear banding event can be neglected since the temperature increase is very small.

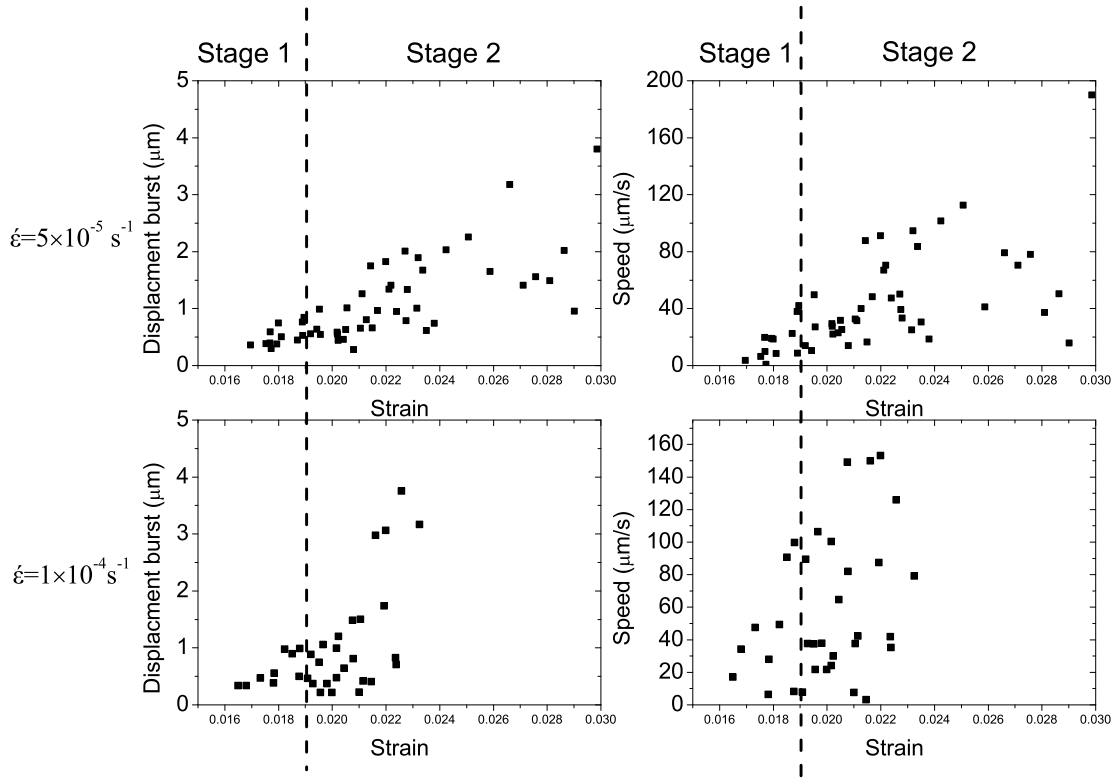
Table 3: Calculated temperature increase of Zr-based bulk metallic glasses associated with a serration event at room temperature at different quasi-static strain rate.

| Strain Rate | $\Delta t(ms)$ | | $v(\mu m/s)$ | | $\Delta\tau(MPa)$ | | $\Delta T(K)$ | |
|--------------------|----------------|---------|--------------|---------|-------------------|---------|-----------------------|-----------------------|
| | Stage 1 | Stage 2 | Stage 1 | Stage 2 | Stage 1 | Stage 2 | Stage 1 | Stage 2 |
| 1/s | | | | | | | | |
| 5×10^{-5} | 60 | 20 | 7.4 | 140 | 7.4 | 42.18 | 1.63×10^{-3} | 1.01×10^{-1} |
| 1×10^{-4} | 60 | 20 | 5.29 | 113 | 5 | 33 | 8.81×10^{-4} | 6.41×10^{-2} |
| 5×10^{-4} | 40 | 10 | 11 | 133 | 5.6 | 27 | 1.50×10^{-3} | 4.36×10^{-2} |
| 1×10^{-3} | 10 | 5 | 40 | 136 | 5.77 | 12.9 | 2.80×10^{-3} | 1.51×10^{-2} |
| 5×10^{-3} | 2 | 2 | 111 | 310 | 1.65 | 10 | 9.95×10^{-4} | 1.68×10^{-2} |
| 1×10^{-2} | N/A | 0.65 | N/A | 1400 | N/A | 16.7 | N/A | 7.24×10^{-2} |

Taking the sample's shear angle of 40.9° measured from Figure 8 and the shear band thickness to be about 10nm [50], the shear strain rate during the shear banding event can be calculated, where propagation of the shear bands is represented by the displacement burst events. The local shear strain rates associated with these shear banding events are calculated to be from $1 \times 10^2 s^{-1}$ to $4 \times 10^5 s^{-1}$ for all the serrated flow events. Knowing the shear strain rate and the shear stress within the shear band, the viscosity inside the shear band can then be calculated with the following equation:

$$\eta = \frac{\tau}{\dot{\gamma}} = \frac{\sigma \cos\theta \sin\theta}{(\Delta L / \cos\theta) / \Delta t d} \quad (8)$$

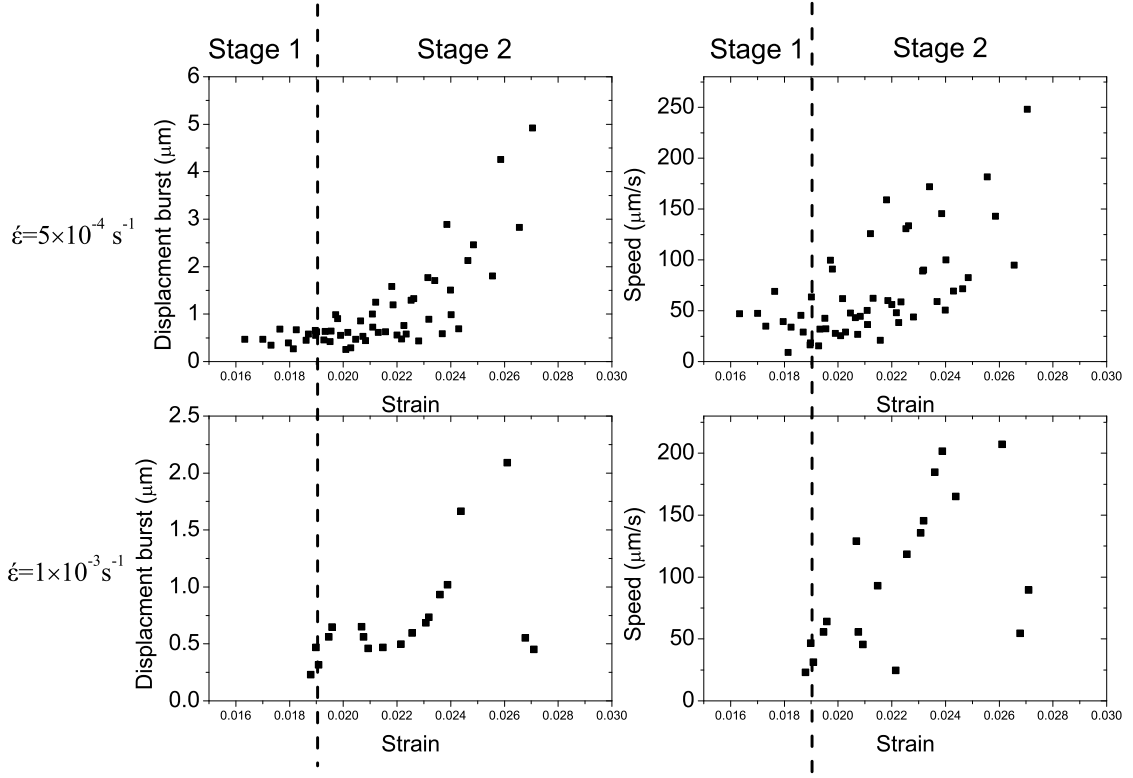
where σ is the applied stress, θ the shear angle, ΔL and Δt the displacement and the time of the burst events, respectively, and d is the shear band thickness. A typical viscosity versus strain relationship is plotted in Figure 15. We can see that there is a general trend in that viscosity decreases as the compressive strain increases. This trend indicates that the shear resistance decreases with increased strain. According to Song et al.[144], this apparent strain softening effect of metallic glass is caused by the random shear events during Stage 1. However during Stage 2, shear band formation is preferred on an existing shear band in the BMG sample. Figure 16 shows an SEM



(a) Figure14

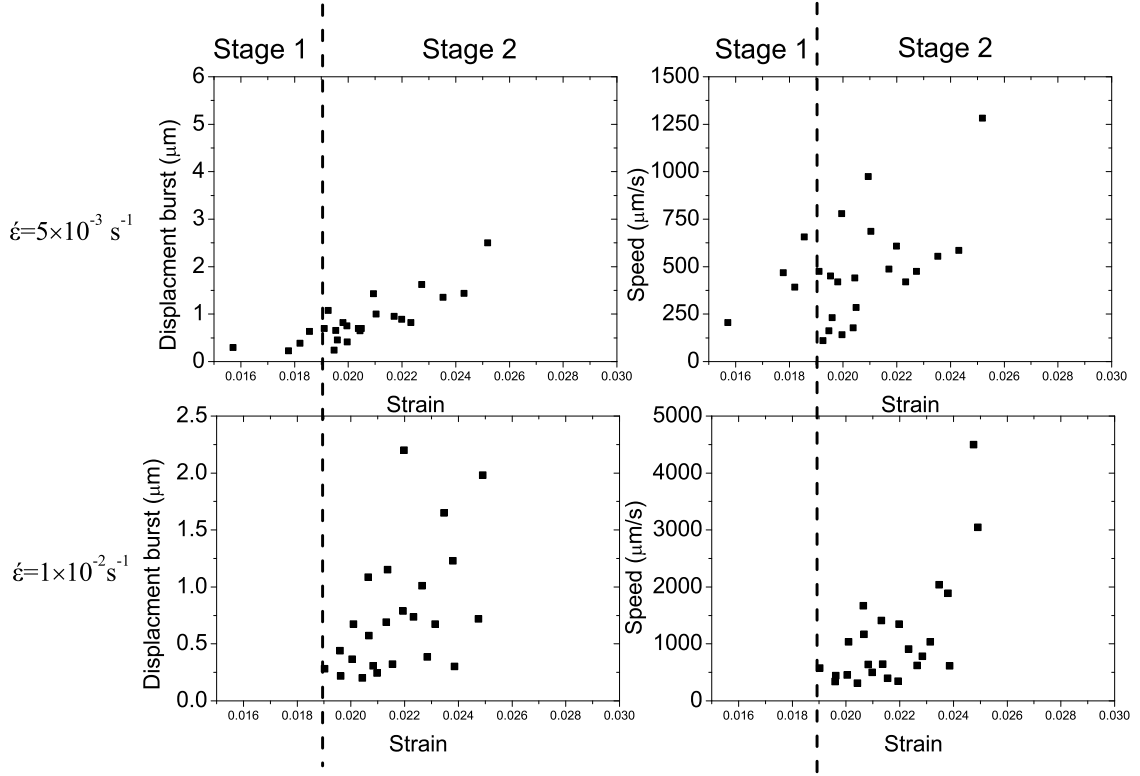
image of post-loading surface of the Zr-based bulk metallic glass. Two shear bands can be clearly observed, and they intersected each other. Apparently one shear band has formed first, followed by the other one, whose formation has caused the shear offset of the first shear band. The offset magnitude was measured to be $12\mu m$. If we consider the shear angle of the Zr-based metallic glass, 40.9° , the total offset in the loading axis direction should be about $9\mu m$. This value is larger than any displacement burst from our data, which indicated that, several shear bands have formed in the same location. Since during the quasi-static compressive loading, the shear band forms individually, the offset observed on Figure 16 is a result of preferential shear band formation on an existing shear band.

At different imposed quasi-static strain rates, the viscosity within each shear band



(b) Figure14 continued

during each burst event was calculated using Equation 8. The viscosity is within the range of $2 \times 10^3 - 7 \times 10^5 \text{ Pas}$, which is quite low. Such low viscosity values are in a similar range to those measured at the temperature in the supercooled liquid region of Zr-based metallic glasses[105]. However, it is noted that the experiments here were all performed at room temperature, which is only $0.43T_g$, well below the supercooled liquid region. As we have discussed above, the temperature increased within the shear band was calculated to be less than $1K$, which means the low viscosity is a result of the local stress introduced structure change. Recently, simulation results have suggested that, the shear stress induced structure evolution inside the shear band has a consequence similar to the temperature-induced structure evolution[129].



(c) Figure14 continued

Figure 14: The displacement burst during the compressive test of Zr-based metallic glass ($Zr_{55}Al_{10}Ni_5Cu_{30}$) at different quasi-static strain rates.

2.4.2 Strain rate sensitivity of bulk metallic glasses at quasi-static strain rate

The plastic deformation of crystalline metals is generally considered to be a thermally activated process. According to the Arrhenius-type equation for the thermally activated processes at large[80], the shear strain rate $\dot{\gamma}$ can be written as

$$\dot{\gamma} = \dot{\gamma}_0 \exp\left(\frac{-\Delta G}{kT}\right) \quad (9)$$

where ΔG is the activation energy to initialize the plastic flow, k is the Boltzmann constant, T is the absolute temperature, and the $\dot{\gamma}_0$ is a constant (the pre-exponential factor). And according to the cooperative shear motion(CSM) model proposed by

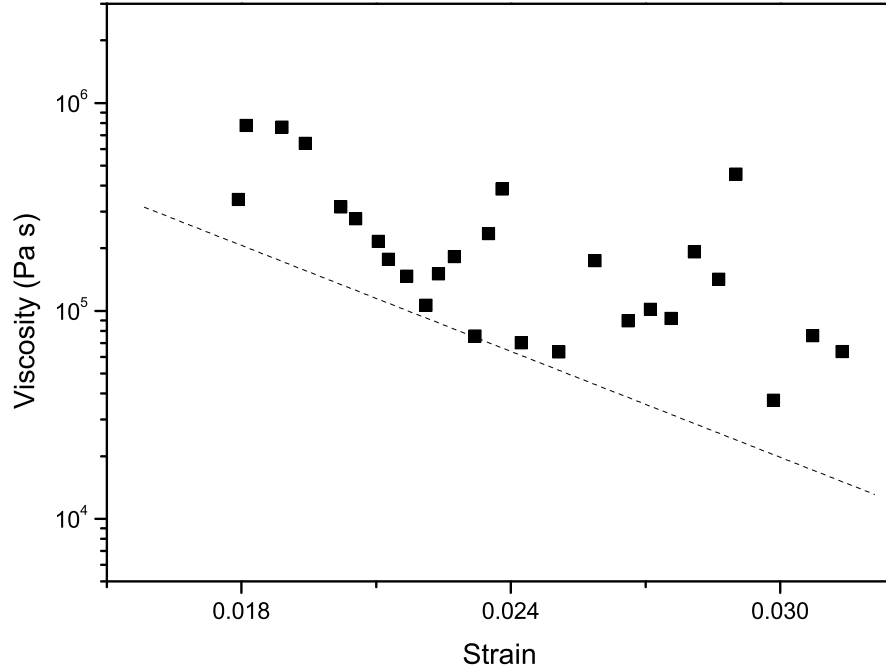


Figure 15: Viscosity in the shear band during the uniaxial compressive experiments as a function of the compressive strain at an imposed strain rate of $5 \times 10^{-5} s^{-1}$.

Johnson and Samwer[68], the activation energy $\Delta G = 4RG_0\gamma_C^2(1 - \tau/\tau_C)^{3/2}\zeta\Omega$. The parameters G_0 and τ_C are the shear modulus and the threshold shear resistance of the metallic glasses at 0 K and R and ζ are constants and their values are 1/4 and 3[68], respectively. The factor γ_C is the average elastic limit with a value of about 0.0267[68]. The activation volume of the plastic flow can be defined in terms of the derivative of activation energy with respect to the shear stress [150], $v^* = -(\partial\Delta G/\partial\tau)_T$. We have measured the fracture surface angle of the quasi-static compressive samples to be less than 45° , which means the fracture does not happen along the maximum shear stress plane. Then we can believe that the critical shear stress should depend on the normal stress component according to the Mohr-Coulomb criterion. But the normal

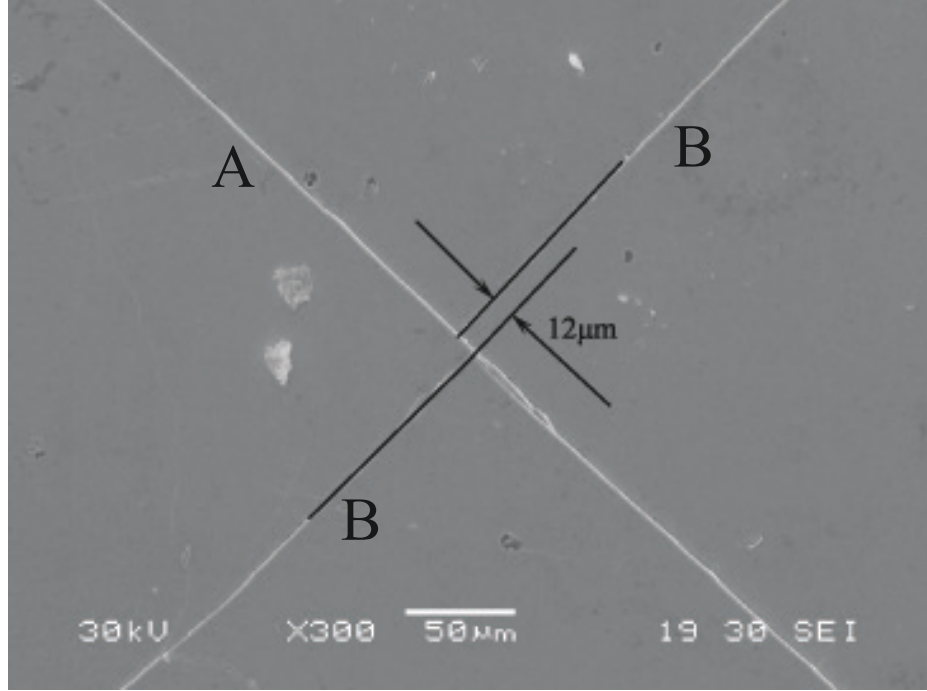


Figure 16: SEM image of the quasi-static loaded Zr-based metallic glass ($Zr_{55}Al_{10}Ni_5Cu_{30}$) sample. Shear band A formed after shear band B, which caused the shear offset of shear band B with a distance of $12\mu m$.

stress dependence coefficient is about 0.07 [183] under uniaxial compressive loading, which can be neglected. In this case the activation volume in the CSM model can be represented as:

$$v^* = - \left(\frac{\partial \Delta G}{\partial \tau} \right) = \frac{6RG_0\gamma_C^2 \left(1 - \frac{\tau}{\tau_C}\right)^{\frac{1}{2}} \zeta \Omega}{\tau_C} \quad (10)$$

As we have described previously, the strain rate sensitivity of a viscoplastic material can be calculated by Equation 4. Furthermore, the relationship between the strain rate sensitivity m and the activation volume of the plastic flow v^* is show as follows:[161]

$$m = \frac{kT}{\tau v^*} \quad (11)$$

Under uniaxial compressive loading, the yield stress $\sigma_y = \sqrt{3}\tau_y$. Then by combining Equations 10 and 11, we can represent the STZ volume as:

$$\Omega = \frac{kT}{2\sqrt{3}R\frac{G_0}{\tau_C}\gamma_C^2 m\zeta\sigma_y \left(1 - \frac{\tau}{\tau_C}\right)^{\frac{1}{2}}} \quad (12)$$

The critical yield shear stress of the metallic glass at temperature T can be expressed as $\tau = (\gamma_{C0} - \gamma_{C1}(T/T_g)^{2/3})G$, where γ_{C0} and γ_{C1} are two constants, and curve fitting of data from other metallic glasses data gives the values as $\gamma_{C0} = 0.036$ and $\gamma_{C1} = 0.016$ [68]. The shear modulus, G , only has a weak temperature dependence. Then we have $\tau/\tau_C = 0.742$ and $G_0/\tau_C = 27.78$. The yield stress of the specimen is taken from the average value of all the quasi-static tests, and $\sigma_y = 1634$ MPa. Since the activation energy defined in the CSM model is the energy needed to initialize the plastic flow, instead of the fracture stress, the yield stresses of $Zr_{55}Ni_5Al_{10}Cu_{30}$ are plotted in Figure 17. The yield stresses are plotted vs. the quasi-static strain rate, and both axes are in logarithmic scale. A simple curve fitting is performed to these data points, and the slope of the curve is found to be 0.022, which means the strain rate sensitivity of $Zr_{55}Ni_5Al_{10}Cu_{30}$ is 0.022. Taking this value together with other parameters into Equation 12, we can calculate the volume of the shear transformation zone to be $\Omega = 4.404nm^3$.

According to Ref.[16], the average atomic radius of the metallic glasses is about 1.459 Å. The number of the atoms inside one individual STZ size can then be calculated to be $N = 3\Omega/4\pi r^3 = 338$. This measured STZ volume with about 300 atoms is in good agreement with the theoretical analysis[68] and the simulation results from

[185, 114]. For the same material, Pan et al.[128] also measured the average size of STZ using nanoindentation method, and we can see that their STZ volume of $Zr_{55}Ni_5Al_{10}Cu_{30}$ is lower than the value from this study. This might be because the yield stress of the work of Pan and co-workers in Equation 12 is derived from the nano-hardness value with a confinement factor of 3, which may overestimate the yield stress of the material, lead to a lower value of the STZ volume by Pan and co-workers.

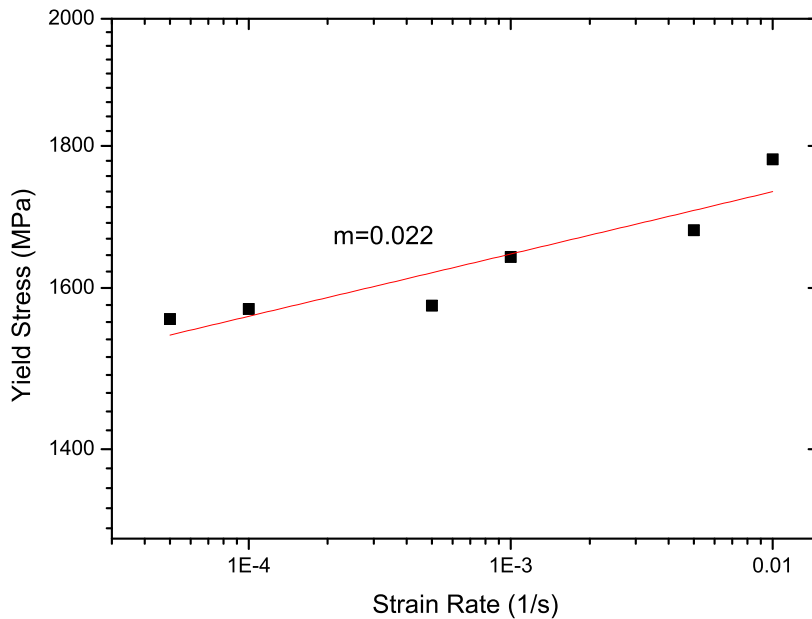


Figure 17: Logarithmic yield stress vs. logarithmic strain rate of $Zr_{55}Ni_5Al_{10}Cu_{30}$ metallic glass based on the quasi-static uniaxial compressive experiments. The SRS value is given as the m value shown in the figure.

2.4.3 Negative strain rate sensitivity based on dynamic experiments

Two alternative mechanisms for the initialization of the shear bands in metallic glasses have long been proposed: the structural changes and the localized heating[50, 90, 68, 13]. Temperature increase during the shear band mediated plastic deforma-

tion has been reported[50, 90]. Hufnagel and co-workers reported that light emission occurred during the dynamic experiments, which suggests that the lower fracture stress of dynamic test was caused by adiabatic heating. However, during the mechanical loading experiments of this thesis work, we have observed light emission both in the quasi-static and dynamic experiments. This indicates that significant adiabatic temperature heating might not be involved, at least under quasi-static loading, as the time scale there is sufficient for the heat to be dissipated out of the specimen under such conditions. From the point of view of structural changes, Argon et al.[2] proposed shear transformation zone as a basic plastic deformation unit of metallic glasses. In this context, the yielding strength of a metallic glass should be related to the average energy barriers of the STZs. Based on the STZ concept and thermodynamics and kinetics of a general plastic flow process, Johnson and Samwer[68] proposed a cooperative shear model to predict the various correlations associated with the plastic deformation of BMGs. In their model, it is suggested that if the energy input by the external force is equal to the energy barrier of the STZ, yielding should occur right after the first STZ becomes unstable. A universal law for shear yielding of metallic glasses is given by[68]:

$$\tau_{CT} = \tau_{C0} - \tau_{C0} \left(\frac{k}{\beta} \frac{G_{0T}}{G_{0T_g}} \frac{T}{T_g} \ln \frac{\omega_0}{C\dot{\gamma}} \right)^{2/3} \quad (13)$$

In the above equation, τ_{CT} is the shear yield stress at a finite temperature T , τ_{C0} the shear yield stress at $T = 0K$, $\dot{\gamma}$ the shear strain rate which is introduced by the external force, T_g the glass transition temperature, k the Boltzmann constant

and ω_0 the attempt frequency. G_{0T}/G_{0T_g} is the ratio of the shear modulus at finite temperature T and at T_g . Parameters C and β are some constants.

According to Equation (13), the yielding shear stress is determined by the temperature of the STZ (T) and the shear strain rate ($\dot{\gamma}$) applied to the STZ. In our case, if we assume no notable thermal effect during the initialization of shear band, the temperature T will not change, and the only dependence of the yielding shear stress will be related to the applied shear strain rate. For uniaxial compression experiments, the shear strain rate can be replaced by $2\dot{\epsilon}$, and when the strain rate increases, the shear yield stress will increase based on Equation (13). In other words, a positive strain rate sensitivity is predicted by Equation (13) if adiabatic thermal effect is not included. Even though the explanation is more or less phenomenological, without details of the atomic processes involved in the formation and evolution of STZs, it does provide some insight into the visco-plastic behavior of the BMGs under quasi-static loading. Our results of the quasi-static experiments can therefore be interpreted using this cooperative shear model as we have discussed in section 2.4.2.

However, results from our Kolsky bar experiments show consistently that the fracture stresses of the investigated BMGs have decreased compared to the fracture stresses of the same materials at quasi-static strain rate. This is unlikely to be due to the stress-concentration effects from irregularities of the specimens and the elastic bars, since first the data is quite consistent and reproducible and secondly we have carefully conditioned both the specimens and the elastic bars before dynamic loading. In this case, apparently the CSM model proposed by Johnson and Samwer [68] cannot be used to explain the dynamic behavior of the BMG materials investigated. Other

factors and effects should be taken into account when considering the constitutive behavior of BMGs within this strain rate regime. The uneven fracture surface shown in Figure 4 reveals that the failure process did not start from one location. Under dynamic loading, the stress level inside the specimen increases so rapidly that many defect sites can initiate shear band simultaneously, or even cracks can be formed right after the initialization of the shear band. Li et al.[92] argued that the decreased fracture strength of metallic glasses is caused by the concurrent processes of the formation of those shear bands and the cracks within the BMG sample. But as we have discussed previously based on the CSM model of Johnson and Samwer[68], the yield strength of a metallic glass can be treated as the average strength of the STZ barriers, and therefore the simultaneous formation of shear bands may not necessarily decrease the yield strength of the specimen. This can also be inferred from the absence of any serrated flows of the high strain rate stress-strain curves presented in Figure 7.

Recently, Liu et al.[101] have proposed that each STZ can be treated as a heat source for the nearby STZ. The elastic energy stored inside the STZ before yielding will be transformed into heat when yielding occurs under high strain rate loading. Since the short time scale allows little or no heat to be dissipated into the surroundings, there will be a thermally affected zone(HAZ) with a size similar to that of the STZ. The adiabatic temperature rise caused by the energy release inside the shear band can then be expressed as[101]:

$$\Delta T = \frac{\zeta \Omega \eta \dot{\gamma}^2}{8\pi \kappa r_0} \quad (14)$$

where ζ is a correction factor, Ω the STZ volume, η the viscosity of the STZ, κ the thermal conductivity and r_0 the radius of the STZ. The value of ζ can be taken to be 2-4[68], and the STZ volume is about $5 \times 10^{-27}m^3$ [128]. The viscosity of the STZ at room temperature can be assume to be the viscosity of a solid which is $10^{15}Pa \cdot s$ and κ is about $20W/(m \cdot K)$ and $r_0 = 10^{-9}m$. If we plot the temperature increase versus the shear strain rate, we can observe that when the shear strain rate is less than $\sim 10^3s^{-1}$, the temperature increase will be very limited. However, when we further increase the shear strain rate, the temperature increase will become noticeable, and the localized temperature will be greater than T_g . At this point, the metallic glass has entered into the super-cooled region, and the viscosity value in Equation (14) will be decreased precipitously. As is well known the viscosity of a metallic glass can be expressed by $\eta = \eta_0 \exp(DT_0/(T - T_0))$, where η_0 is the viscosity limit and D is a constant. After the change of viscosity, the temperature increase will slow down again. Because of the noticeable temperature increase which brings the local temperature into the super-cooled region of the metallic glass, the strength should also experience a sudden drop. If the adiabatic temperature rise effect is considered in the constitutive description of the materials, Equation (13) can be rewritten as[101]:

$$\tau_{CT} = \tau_{C0} - \tau_{C0} \left(\frac{k G_{0T}}{\beta G_{0T_g}} \frac{T_r + \frac{\zeta \Omega \eta_0 \exp(DT_0/(T-T_0)) \dot{\gamma}^2}{8\pi\kappa r_0}}{T_g} \ln \frac{\omega_0}{C \dot{\gamma}} \right)^{2/3} \quad (15)$$

This equation predicts that at dynamic (high) strain rate, the adiabatic temperature rise associated with the STZs will render the strength of the BMG to become lower. In other words, under high strain rate loading, a negative strain rate de-

pendence should be expected because of local adiabatic heating. From Figure (10), we can see that the fracture surface of the dynamic specimen has many melted areas which are largely missing from the quasi-static specimen. Such fracture surface features further confirm that the local temperature increase is much larger during dynamic loading than that of quasi-static loading, which leads to a lower fracture strength.

2.5 Summary and concluding remarks

In this chapter, the uni-axial compressive plastic deformation behavior of four different Zr/Hf-based metallic glasses has been characterized at quasi-static and dynamic strain rates to investigate the strain rate dependence of these BMGs. Serrated plastic flows during the quasi-static compressive experiments suggest that individual shear band formation at each serration is the primary mechanisms of plasticity of these BMGs. Local temperature increase can be neglected from the calculated results for quasi-static loading. Localized decreasing of viscosity is caused by the stress induced structural change. We have found that the high strain rate compressive fracture strength is lower than that of quasi-static strain rate for all the specimens investigated. However, multiple strain rate quasi-static compressive experiments point to positive strain rate sensitivity . Therefore we have envisaged a change in the deformation mechanism at high strain rate which involves significant local adiabatic thermal effect. Fractography of the dynamic samples shows numerous areas that might have gone through local melting. We have adopted a modified cooperative shear model proposed recently by Liu and co-workers [34] to provide a consistent explanation

of the experimental observations. This model suggests that in the low strain rate regime, the temperature increase inside the STZ is insignificant, and the shear rate dominates the yield stress of the materials, which leads to a positive strain rate dependence within the quasi-static loading regime. However, when the strain rate is increased into the dynamic regime, the temperature will increase very quickly within some local regions(STZs and their close neighboring areas) and eventually reach the glass transition temperature of the metallic glass. This will decrease the local viscosity of the material and lead to decreased fracture strength under dynamic loading, thus an apparently negative strain rate sensitivity.

CHAPTER 3: UNIAXIAL COMPRESSIVE BEHAVIOR OF BULK METALLIC GLASS UNDER ELEVATED TEMPERATURE

3.1 Introduction

The mechanical properties, including strength, ductility and plastic deformation mechanisms of bulk metallic glasses (BMGs) have attracted considerable attention and interest from researchers in recent years since these materials exhibit numerous attractive properties [135, 52, 158, 156]. Previous research results suggest that the mechanical behavior of metallic glass depends on the environmental temperature and the imposed strain rate. At low temperature (in the context of the temperature compared to the glass transition temperature), the material would present inhomogeneous deformation (see the general discussion in Chapter 1), and the strain rate effect is different during the quasi-static region and the dynamic region. For the high temperature properties of metallic glasses, Lu et al. [105] have reported a transition from inhomogeneous to homogeneous deformation for Vitreloy 1 when the testing temperature was increased beyond a certain level, and they also found a transition from Newtonian flow to non-Newtonian flow when the strain rate is increased beyond a critical value.

Generally speaking, the plastic deformation mechanism of metallic glasses can be classified into two modes, namely, homogeneous and inhomogeneous deformation. As the temperature increases, a metallic glass can exhibit homogeneous plastic de-

formation, showing considerable inelastic strain. In the past decades, homogeneous deformation of several metallic glasses around their glass transition temperature were investigated. Kawamura et al.[73, 72] performed some high temperature tensile tests of $Zr_{65}Al_{10}Ni_{10}Cu_{15}$ and $La_{55}Al_{25}Ni_{20}$ metallic glass ribbons. Instead of inhomogeneous deformation at room temperature, the tensile test of those metallic glass at glass transition temperature has revealed large plastic strain accompanied by necking. Uniaxial compressive experiments have been performed by Kato et al.[71, 70] on $Zr_{55}Al_{10}Ni_5Cu_{30}$ and $Pd_{40}Ni_{10}Cu_{30}P_{20}$ within their homogeneous deformation regime. However, the strain rate was limited to the quasi-static range, and less data on the mechanical behavior of metallic glasses at elevated temperature at high strain rate is available.

In order to describe the plastic deformation behavior of bulk metallic glasses, several models and theories have been proposed. Argon developed a model based on the notion of shear transformation zone (STZ), to describe the homogeneous and inhomogeneous flow of Pd-Si metallic glass[2]. Spaepen[147] proposed the free volume concept based on the pioneer work of Turnbull and Cohen[151, 17, 152, 153], and attributed the free volume creation and annihilation to the applied stress and diffusion, respectively. The free volume concept will be discussed in detail later. Kato et al.[70] adopted a simple model based on the fictive stress to simulate the stress-strain behavior of metallic glasses at elevated temperatures. Based on the shear transformation zone model, Johnson et al.[68] has developed a cooperative shear model(CSM) to describe the relationship between the yield stress, temperature and the strain rate.

In this chapter, we will investigate the mechanical behavior of the $Zr_{55}Al_{10}Ni_5Cu_{30}$

metallic glass with wide ranges of temperatures and strain rate (both quasi-static and dynamic strain rates). Quasi-static uniaxial compression will be conducted with the MTS high temperature test system. High strain rate and high temperature uniaxial compression experiments will be performed with an improved synchronically assembled heating system along with the Kolsky bar system. The homogeneous deformation behavior was discussed and simulated with the free volume model, and the relationship between the temperature and the failure stress will also be discussed.

3.2 Experimental procedures

To establish a comprehensive understanding of the mechanical behavior of the bulk metallic glasses, in this chapter we will examine their mechanical properties over a wide range of loading rates and temperatures. In what follows, we will describe the experimental details of the work, including the quasi-static loading experiments, dynamic loading experiments with Kolsky bar technique facilitated with a heating unit, and the associated cold contact time issue.

3.2.1 Quasi-static loading experiments

The quasi-static compression (strain rate $10^{-3}s^{-1}$) experiments were performed on an MTS 810 hydro-servo loading system. The Model 680 high temperature hydraulic grips were used to perform the high temperature tests. Tungsten carbide platens were inserted into the ends of the grips to protect the grip surface from damage under the high stress level. The Model 652 high temperature furnace with the MIC2000 controller system was used to heat up the samples during the tests. The heating speed was controlled to be at $20K/min$ and the temperature was held at the target

point for about 2 minutes before applying the load. A K-type thermocouple is placed next to the specimen located at the center of the furnace to ensure the accuracy of the temperature measurement. Due to the thermal lag between the furnace and the sensor, temperature overshoot and undershoot may be unavoidable, especially at the moment when a target temperature is reached. However, with the MIC 2000 PID controller, the temperature fluctuations could be reduced. The metallic glass rods were cut with a low speed diamond saw into compression specimen with dimensions of 3.0×6.0 mm (6.0 mm is for the gauge length), so that the length-to-diameter aspect ratio is close to 2:1. The loading faces of the specimens were carefully polished using 1200 grit polishing paper before mechanical loading to ensure the parallelism of the two faces. The interface between the loading faces and the compression platens were carefully lubricated to mitigate friction with high temperature lubricant. The strain rate was controlled by the crosshead speed, and the strain was calculated based on the displacement of the crosshead and therefore we did not attempt to derive the elastic modulus from such quasi-static compression due to the machine compliance issue.

3.2.2 Dynamic loading experiments

The traditional Kolsky bar system (or split Hopkinson pressure bar) shown as Figure 5 has been widely used to investigate the dynamic or high strain rate mechanical properties of materials at room temperature. But in many important applications, knowledge of the mechanical behavior of the material at elevated temperatures is important. Compared to measuring the dynamic mechanical properties of materials

at room temperature, high strain rate testing at elevated temperatures with the Kolsky bar technique becomes challenging. The major difficulty is how to avoid heating up the elastic bars before the loading wave arrives at the specimen/input bar interface. Equation 5 has demonstrated that the stress wave profiles obtained from Kolsky bar experiments are related to the Young's modulus and mass density of the elastic bars (the elastic modulus and the mass density together determine the mechanical impedance of the material). In a traditional high temperature Kolsky bar system, the specimen is usually sandwiched between the two elastic bars (the input and output bars), and the furnace will heat up the specimen together with the ends of the two elastic bars. But, from the research results of Latella and Humphries[82], the Young's modulus of 2.25Cr-1Mo high strength steel decreased from 212.4 GPa at room temperature to 169 GPa at 600°C. In order to avoid the significant temperature increase within the elastic bars, various methods have been proposed. Liu et al. placed two water tanks in the middle part of the two elastic bars to decrease the heat effect of the whole bars[100]. Although this method can decrease the temperature within the elastic bars, the two ends of the elastic bars were still within the furnace, and temperature effect will still be a problem within that section. In order to prevent or at least mitigate the preheat of the elastic bars, researchers have been trying to use some advanced techniques to bring the bars in contact with the specimen right before the stress wave has arrived at the interface between the specimen and the incident bar. Nemat-Nasser and Isaacs [121] at the University of California at San Diego (UCSD) applied the UCSD technique to a traditional Kolsky bar system; Lennon et al. [86] has simplified the UCSD technique by using a gas-pressure-driven system instead of

the stiff-bar-driven system of the UCSD design. The technique used in this work is based on the design of Lennon's work.

Although the synchronically assembled heating system which can in principle bring the bars into contact with the specimen shortly before the stress wave reaches the end of the incident bar, a critical issue with this system is how to control the time gap between the time point when the specimen is in contact with two bars and the point when the stress wave reaches the interface of the incident bar and the specimen. Usually we can call this time gap the cold-contact-time (CCT)[1, 86, 95, 141]. Based on the results from prior researchers, there is still uncertainty regarding the optimum value of the critical CCT value. Lennon et al.[86] suggested that the critical CCT should be 5ms from their finite element simulation results. Seo et al.[141] used experimental method to measure the CCT. They inserted two thermocouples into the specimen to measure the temperature gradient within the specimen. Their results suggested that the critical CCT was about 1s, which was much larger than the results from the work of Lennon and co-author[86]. However, the large CCT value may be caused by the temperature delay between the specimen and the thermal couples. Li et al.[95] used both finite element method (ABAQUS) and experimental method to evaluate the critical CCT. They tested Ti specimens at elevated temperature with different CCT values, and compared the experimental results against their simulation results. Based on their experimental and simulation results they stated that the critical CCT value for compression Kolsky bar experiments should be around 50ms.

In order to perform the high temperature dynamic experiments, in our work a synchronically assembled heating system was added to traditional Kolsky bar system,

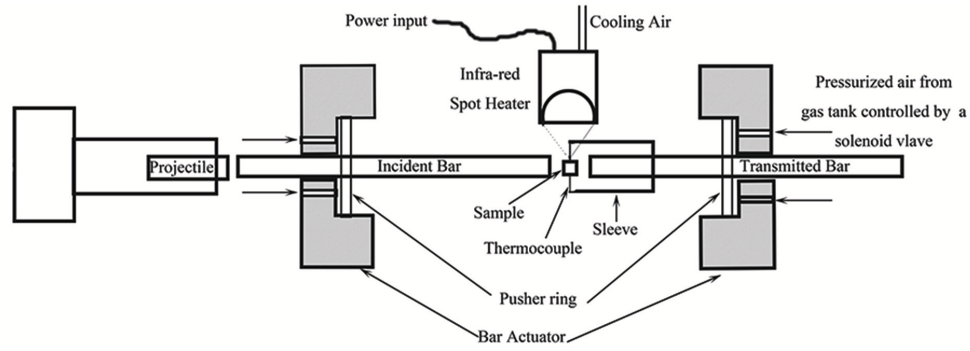


Figure 18: Schematic drawing of the High-temperature compressive Kolsky Bar with a synchronically assembled heating system. The projectile and the bar actuation is controlled by labview together with a programmable DC supply. Specimen temperature is controlled by a PID temperature controller.

as shown in Figure 18. The major parts of this synchronically assembled heating system include two bar actuators, two pusher rings, and an infra-red spot heater. The specimen is separated from the incident bar and transmitted bar with a distance about 4mm before loading, since the heating area of the spot heater is about 10mm in diameter. The specimen is held at the prescribed position with the thermocouple which is wired on the sleeve. The sleeve can be freely moved along the axial direction of the bars. The specimen is heated up with the spot heater, and a PID controller from Omega Inc. is used to control the temperature. After the specimen temperature has reached the target temperature, the incident and transmitter bars are brought to contact with the specimen using the two bar actuators. Two pusher rings are attached to the incident and transmitter bars, which is fixed at the position. Two separate gas tanks controlled by solenoid valves are used to supply pressurized air. The pressurized air released from the gas tanks will go through the bar actuators and push the pusher rings together with the bars and bring the bars into contact with the specimen. Another solenoid valve is used to control the fire time of the

projectile. In order to obtain the proper launch time, calibrations need to be done with the synchronically assembled heating system. Figure 19 shows the calibration results. Figure 19 (a) shows the signals of the activation voltage of the solenoid valve controlling the gas gun, and the strain gage signals from the incident bar and the transmitter bar. In the first step of the calibration, two bars were in contact with each other without specimen, and a voltage was supplied to the solenoid valve to fire the projectile. The time duration between the voltage supply and the stress wave traveled through the incident bar strain gage was recorded as Δt_2 . The second step of the calibration result is shown in Figure 19 (b), where the incident bar and transmitter bar were separated with a distance of 8mm. A voltage was given to the solenoid valves to release the pressurized gas to push the pusher rings. The two bars will contact each other, and during the contact, a small stress wave will be generated and captured by the strain gages. The time duration of these steps can be measured by the oscilloscope as shown on Figure 19 (b) as Δt_1 . Calibration results show that the projectile should be fired before launching the bar actuators. The time gap can be calculated by $\Delta t = \Delta t_2 - \Delta t_1$. The Rigol DP1308A programmable DC supply is used to provide power to the solenoid valves, and the time gap between the bar actuation and the projectile launch is controlled by LabView program connected to the DC supply.

We also used scanning electron microscopy (SEM; model No. JEOL JSM 6480) to evaluate the postmortem specimens. The purpose of this is to reveal the fracture surface information to investigate the plastic deformation mechanisms associated with the bulk metallic glasses tested both under quasi-static and high rate loading at

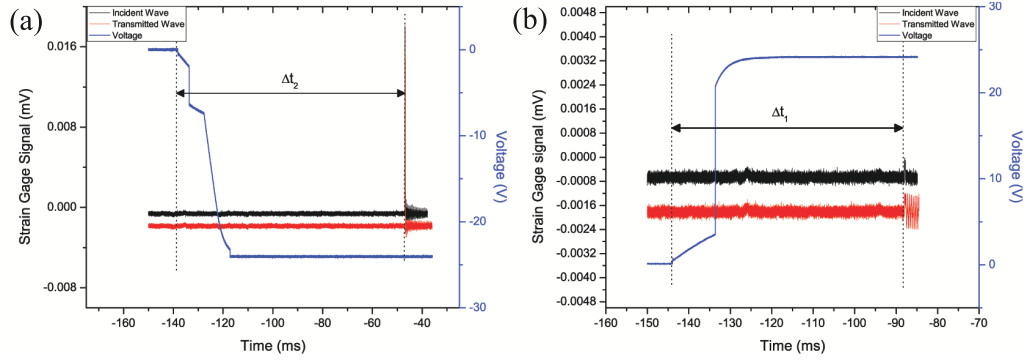


Figure 19: Calibration needed to calculate the firing delay. (a) shows the duration time between the launch of projectile to the stress wave travel through the incident strain gage. (b) shows the duration time between launch of the bar actuator to bar closure.

various temperatures. The SEM analysis was performed on JEOL JSM 6480 operated at 20KV.

3.3 Experimental Results

Figure 20 displays the representative quasi-static compressive true stress-strain curves of the $Zr_{55}Ni_5Al_{10}Cu_{30}$ bulk metallic glasses samples tested at different temperatures. Except for the curve measured at room temperature, all other curves are shifted by a certain value of strain for a better view. It can be observed that for this Zr-based metallic glasses, the fracture stress decreases with increased temperature. There are almost negligible plastic deformation when the testing temperatures were below 678K. The samples fractured right after the elastic deformation through a highly localized shear banding event. However, on further increasing the testing temperature, the plastic deformation will be transformed from inhomogeneous shear band deformation to homogenous plastic deformation. It is noticed that, the specimens tested at 678K did not fail. The tests were stopped at a prescribed strain. In the temperature range of 678-718K, instead of deformation within the very nar-

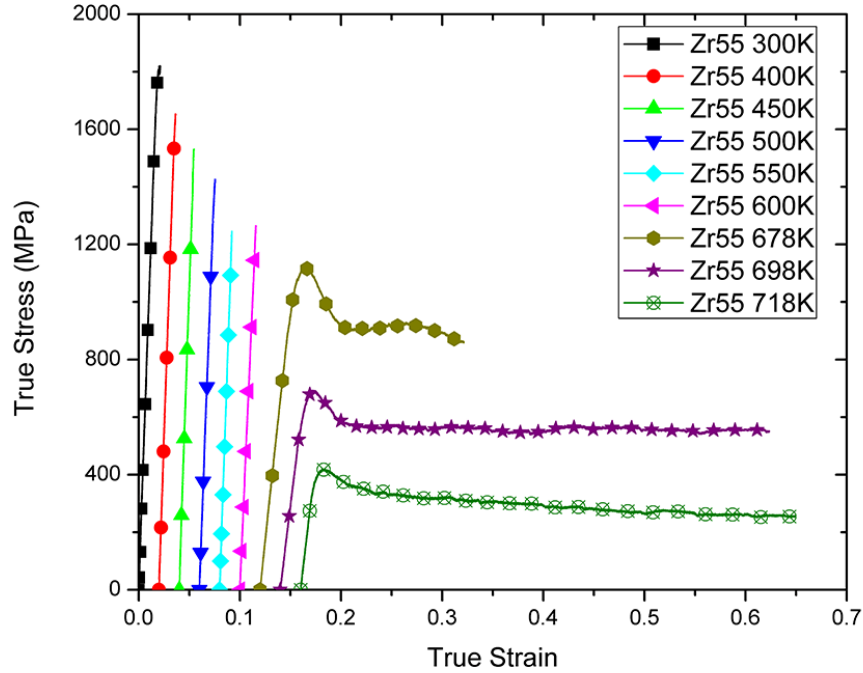


Figure 20: Quasi-static true stress versus true strain of the $Zr_{55}Ni_5Al_{10}Cu_{30}$ bulk metallic glasses from room temperature to the temperature around its glass transition temperature. The curves are shifted with certain value of strain to distinguish from each other.

row shear bands, the specimens deformed in a homogenous way, which can also be verified through the stress-strain curves. The maximum strain value of each curve for the specimens exhibiting homogenous plastic deformation data was limited by the prescribed strain of the compressive experiments. In these specimens tested at temperature higher than 687K, there were no indications of any possible impending catastrophic failure. All the specimens tested at temperatures above 678K deformed uniformly and no macroscopic shear localization has been observed. The initial slopes of the stress-strain curves decrease with increased temperature, especially when the temperature is above 678K. This decreasing trend of the initial slope indicates the

the Young's modulus decreases with temperature, similar to the behavior of crystalline metallic alloys. Stress overshoots, which are the difference between the peak stress and flow stress have been observed when the testing temperature is greater than 678K. The same phenomenon has also been reported by Lu et al.[105]. The magnitude of the stress overshoot decreases with increased temperature.

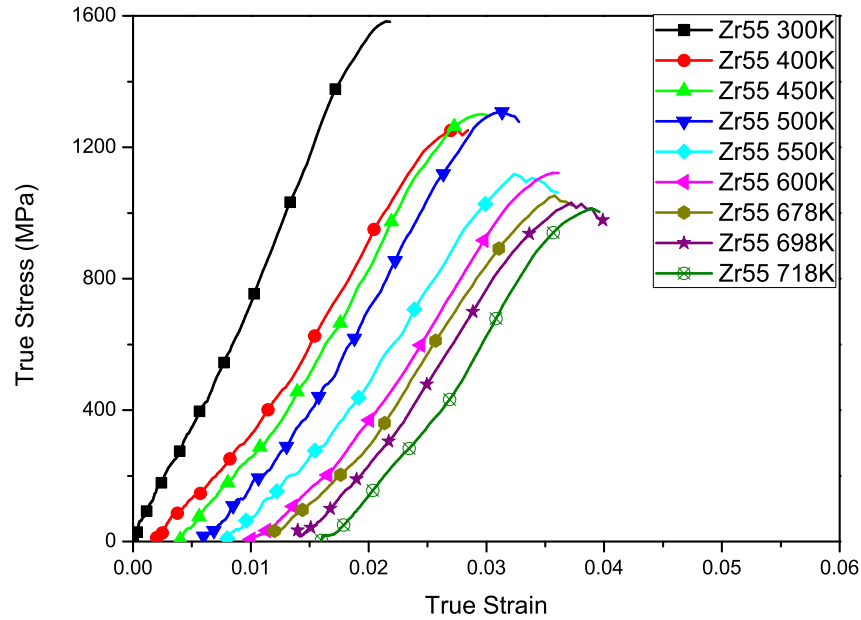


Figure 21: Dynamic true stress versus true strain of the $Zr_{55}Ni_5Al_{10}Cu_{30}$ bulk metallic glasses from room temperature to the temperature around its glass transition temperature. The curves are shifted with certain value of strain to distinguish from each other.

The dynamic true stress strain curves of the Zr-based bulk metallic glass at different temperatures have been plotted in Figure 21. The maximum stress of the specimens decreases with increased temperature, which has also been observed in the quasi-static compressive experiments. But when the temperature is around the glass transition temperature, there is no transition from inhomogeneous deformation to homogenous

deformation. Instead, the specimens failed right after elastic deformation even when the testing temperature was 718K. The stress dropped to zero immediately after it reached its maximum value, typical of "brittle" failure. Compared with Figure 20, the specimens exhibited a transition from homogeneous flow to inhomogeneous deformation as the imposed strain rate is increased.

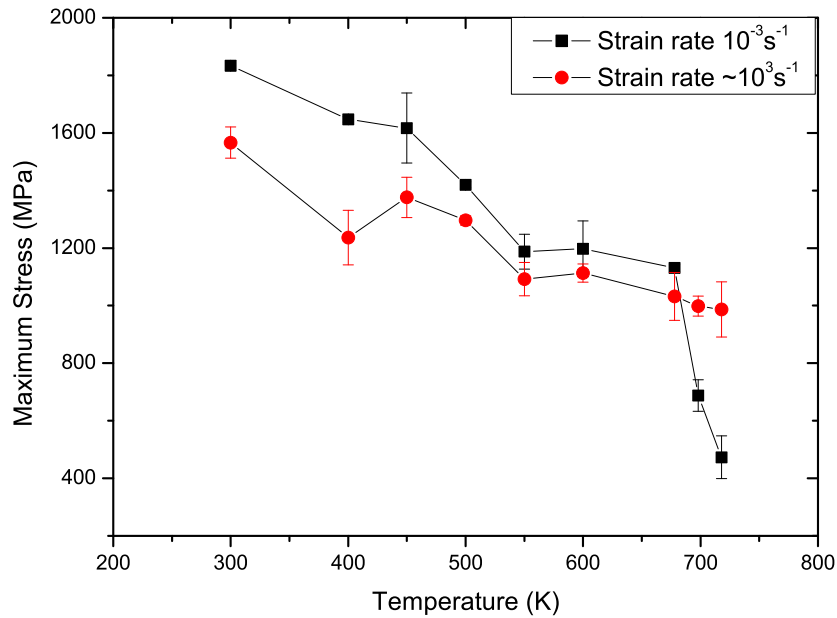


Figure 22: Maximum stresses of the $Zr_{55}Ni_5Al_{10}Cu_{30}$ bulk metallic glasses were plotted as a function of temperature. The black solid circle represented the quasi-static strain rate, $\dot{\epsilon} = 10^{-3} s^{-1}$, and the red solid square represented the dynamic strain rate, $\dot{\epsilon} \sim 10^3 s^{-1}$.

The maximum stress, which is one of the principal parameters used to characterize the strength of a bulk metallic glass, is plotted as a function of temperature in Figure 22. In the inhomogeneous plastic deformation region, the variation of the maximum stress with respect to temperature is small compared to its variation in the homogeneous region when the strain rate is $10^{-3} s^{-1}$. The average maximum stress has been

decreased from around 1830 MPa at room temperature to around 1130 MPa at 678K. When temperature is beyond 678K, a remarkable drop in maximum stress occurred. For instance, with increasing temperature of only 20 K, the maximum stress drops from 1130 MPa at 678 K to 690 MPa at 698 K. However, there is no significant stress drop with respect to temperature when the strain rate is in the dynamic region ($\dot{\epsilon} \sim 10^3 s^{-1}$) even in the supercooled temperature region. The maximum stress was reduced from around 1550 MPa at room temperature to about 1000 MPa at about 718K when the strain rate is about $10^3 s^{-1}$. Comparing the maximum stress with respect to the imposed strain rate, we can find that the maximum stress decreases when the strain rate is increased at low temperature. However, when the testing temperature is within the super-cooled liquid temperature region, the strain rate effect will be opposite. That is to say, the maximum stress during the dynamic test is higher than its counterpart under the quasi-static loading condition.

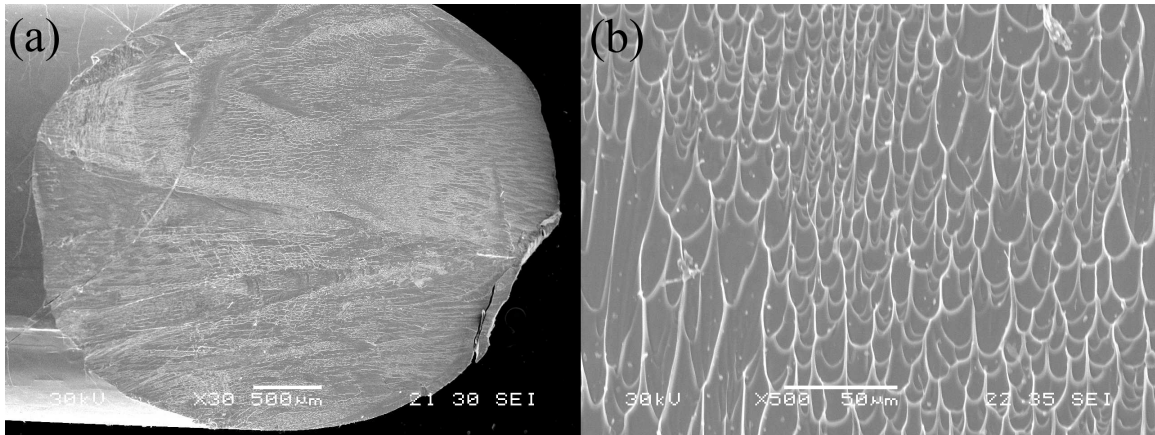


Figure 23: SEM images of the fracture surface of the $Zr_{55}Ni_5Al_{10}Cu_{30}$ bulk metallic glass tested at strain rate of $10^{-3} s^{-1}$ with room temperature. (a) is the overview of the fracture surface and (b) is the high magnification of the vein patterns.

Except for the specimens tested at high temperatures and quasi-static strain rate,

all other specimens in the current work fractured into two pieces, and the fracture specimens were observed by SEM. Figure 23 presents the SEM micrographs of the fracture specimen after quasi-static loading at room temperature. It can be seen that the fracture surface is flat, and the well-known vein like patterns can be observed with a uniform distribution. However, compared with the room temperature quasi-static tested samples, the fracture surface of the specimen tested at 550K at strain rate of $10^{-3}s^{-1}$ exhibits an uneven surface, as shown by Figure 24. Although vein like pattern can be seen on the fracture surface, the distribution is no longer uniform and the vein like patterns are discontinuous and accompanied by small bands. At dynamic strain rates and when the specimens were tested at room temperature, the fracture surface has the same morphology as we have discussed in Chapter 2. But, when the testing temperature is high, for example, 698K (Figure 25), the vein like pattern almost disappeared, and the surface is very rough and the high magnification of the fracture surface exhibits a large melted area, which might be caused by the high environmental testing temperature. It also suggests that severe local melting has occurred during the test. It is noted that, even when the test temperature is 698K, which is higher than the glass transition temperature of $Zr_{55}Ni_5Al_{10}Cu_{30}$, there is yet no crystallization phenomenon found. Liu et al.[100] has reported crystallization during the high temperature dynamic tests, and the crystallization is mainly caused by the long heating time during their test. The heating time in the current work is less than 5 minutes, which is not long enough to activate the crystallization of the tested metallic glass.

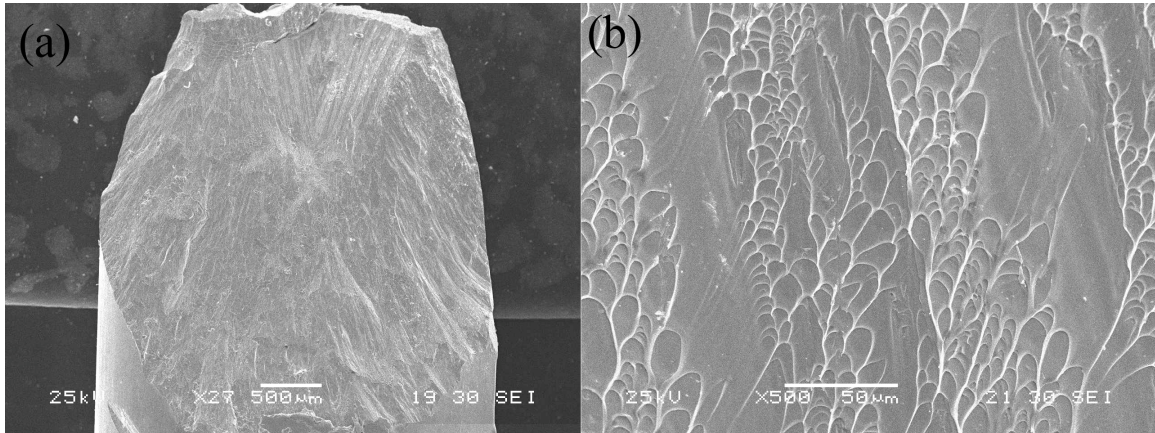


Figure 24: SEM images of the fracture surface of the $Zr_{55}Ni_5Al_{10}Cu_{30}$ bulk metallic glass tested at strain rate of $10^{-3}s^{-1}$ with temperature of 550K. (a) is the overview of the fracture surface and (b) is the high magnification of the vein patterns, compare to the room temperature sample, the vein pattern is not continuous.

3.4 Discussion

3.4.1 Homogeneous Deformation

Homogeneous deformation has been found during the low strain rate and high temperature mechanical testing, particularly around the glass transition temperature, T_g , which involves a viscoelastic behavior. The deformation involves a viscoelastic behavior, which is similar to other glassy materials. The deformation behavior strongly depends on the testing temperature and the imposed strain rate. With respect to different testing environment, the homogeneous deformation can be divided into two modes, linear and nonlinear viscoelasticity. The former features elastic deformation followed by a steady-state Newtonian viscous flow, while the latter exhibits a stress overshoot and then attains a steady-state non-Newtonian flow. The overshoot during the non-linear viscoelastic deformation has been attributed to the free volume induced structure relaxation[71, 147].

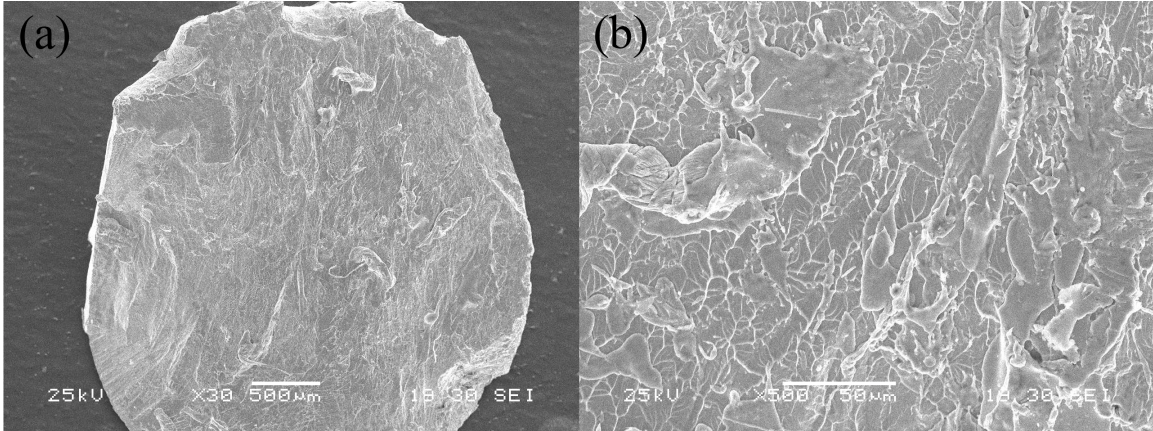


Figure 25: SEM images of the fracture surface of the $Zr_{55}Ni_5Al_{10}Cu_{30}$ bulk metallic glass tested at strain rate of $\sim 10^3 s^{-1}$. (a) is the overview of the fracture surface and (b) is the high magnification of the fracture surface with large melted area.

The free volume model had been proposed by Spaepen[147] in 1977 to describe the homogeneous and inhomogeneous deformation of metallic glasses. In this work, we will apply this model to the analysis of the deformation behavior of the bulk metallic glass at high temperature. In his work, Spaepen has modeled the macroscopic strain rate as a result of accumulation of many events of local atomic rearrangement, or local atomic jumps. The shear strain rate is defined by the following equation:

$$\dot{\gamma} = f \times n \quad (16)$$

where f is the fraction of potential jump sites of the tested material, and n is the net number of forward jumps on each of those sites per second. Here, according to Spaepen's[147] assumption, the strain produced at each jump site equals to 1. The fraction of potential jump sites can be calculated according to Cohen and Turnbull's[17, 152, 153] free volume theory as follows:

$$f = \exp\left(-\frac{\alpha v^*}{v_f}\right) \quad (17)$$

where α is a geometrical factor, and its value can be taken as $\alpha = 0.5$ [147], v^* is the critical volume, which equals to $6.5 \times 10^{-30} m^3$ [16], v_f is the average free volume per atom inside the material. During the homogeneous deformation process, we assume that the free volume distribution within the material is uniform. If the energy barrier of the atomic jump is denoted by ΔG^m , and there is no stress applied to the specimen, the number of successful jumps per second can be calculated by a simple rate theory according to the general Arrhenius equation such as:

$$n_0 = v \exp\left(-\frac{\Delta G^m}{kT}\right) \quad (18)$$

where v is the frequency of atomic vibration, and the value can be taken as $10^{13} Hz$ [88], k is the Boltzmann's constant, and T is the absolute temperature. If a stress is applied, the jump number will increase because of the decreasing of the potential energy by the applied stress. Under the uniaxial compression test condition, we can assume that there is no effect of the atomic jump caused by the mean stress, as the study of Lowhaphandu et al.[104] of a Zr-based metallic glass showed that the flow stress and the fracture strain are independent of the imposed mean stress. So the total number of successful jumps in a uniaxial compressive system with a compressive stress σ is:

$$n = 2v \exp\left(-\frac{\Delta G^m}{kT}\right) \sinh\left(\frac{\sigma \Omega}{2\sqrt{3}kT}\right) \quad (19)$$

where Ω is the atomic volume, and here we can assume $\Omega = v^*$. Therefore, the macroscopic strain rate of the specimen caused by the applied stress σ can be represented by combining the production of Equation 17 and 19 as:

$$\dot{\epsilon} = 2v \exp\left(-\frac{\alpha v^*}{v_f}\right) \exp\left(-\frac{\Delta G^m}{kT}\right) \sinh\left(\frac{\sigma \Omega}{2\sqrt{3}kT}\right) \quad (20)$$

If the imposed strain rate is a constant, Equation 20 reveals that the stress profile of the specimen under homogeneous deformation is strongly related to the free volume v_f of the material. Spaepen[147] divided the free volume change into two parts: one is the free volume creation caused by the applied stress, and another part is the free volume annihilation caused by the atomic jump and relaxation. The net rate of the free volume change can be calculated by taking the difference between the creation and annihilation as follows:

$$\frac{dv_f}{dt} = v^* v \exp\left(-\frac{\alpha v^*}{v_f}\right) \exp\left(-\frac{\Delta G^m}{kT}\right) \times \left[\frac{2\alpha kT}{v_f S} \left(\cosh\frac{\sigma \Omega}{2\sqrt{3}kT} - 1 \right) - \frac{1}{n_D} \right] \quad (21)$$

where n_D is the number of atomic jump needed to annihilate a free volume of v^* , and the value can be taken as 3[148]. S can be represented by the shear modulus and Poisson's ratio of the material as $S = \frac{2}{3}\mu \frac{1+\nu}{1-\nu}$.

In Equation 20, the strain rate corresponds to plastic deformation. For a metallic glass that undergoes homogeneous deformation, the elastic strain is also needed to be included in the final representation. The total strain rate during the deformation can then be represented as:

$$\dot{\epsilon} = 2v \exp\left(-\frac{\alpha v^*}{v_f}\right) \exp\left(-\frac{\Delta G^m}{kT}\right) \sinh\left(\frac{\sigma \Omega}{2\sqrt{3}kT}\right) + \frac{\dot{\sigma}}{E} \quad (22)$$

In Equation 22, E is the elastic modulus at a given temperature. Numerical solving of the coupled Equation 21 and 22 allows reproduction of the stress-strain relationship during the compression tests. In stead of using v_f as the free volume, we can represent the free volume concentration by a dimensionless parameter, $\xi = v_f/v^*$. According to Huang et al.[47], the initial free volume concentration can be taken as 0.008. The typical energy barrier for atomic jump is $\Delta G^m \sim 10^{-19} J$; the imposed strain rate is a constant with a value of 0.001 1/s (quasi-static). For testing temperature at 698K, using the experimental elastic modulus value ($\sim 30\text{GPa}$) and the shear modulus $\mu = 10\text{GPa}$ from Hojo's work[45], we can compared the model prediction with our mechanical test result as Figure 26.

Figure 26 is the comparison of model prediction with experimental data at temperature of 698K. In this figure, the black solid line is the experimental result, while the red dashed line is the numerical solution based on Equation 21 and 22. We can see that the free volume model is able to describe the appearance of the stress overshoot after the elastic deformation. The stress oscillation demonstrated by the model after the stress overshoot is also reported by Johnson et al.[67]. But the oscillation reported by Johnson occurred at strain rate of $\sim 10^{-2} s^{-1}$. The disappearance of the stress oscillation during the experiment may be caused by the viscoelastic behavior of the material deformed at high temperature. The existence of the anelastic part will eliminate the oscillation.

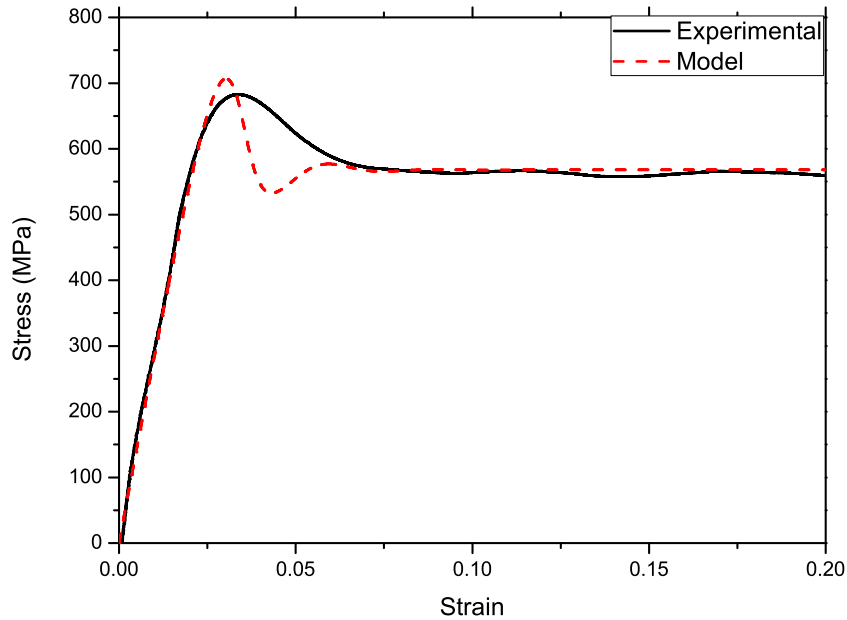


Figure 26: Experimental and simulated true stress-strain quasi-static compression result of $Zr_{55}Ni_5Al_{10}Cu_{30}$ bulk metallic glass at testing temperature of 698K. The black solid line is the experimental result, while the red dash line is the numerical solution from the free volume model.

In order to understand the reason for the stress evolution during the high temperature uniaxial compression test, the free volume concentration and the stress versus the strain relationship from the free volume model are plotted in Figure 27. Because of the small value of the applied stress, we can see that free volume annihilation dominates the beginning of the compression test compared to the free volume creation caused by the applied stress. The free volume concentration decreases as the stress increases. However, when the stress is larger than a certain value, the free volume creation part in Equation 21 becomes larger than the annihilation part $1/n_D$, and the free volume concentration will begin to increase as revealed by Figure 27. After that, the free volume concentration is controlled by the competition of the free volume

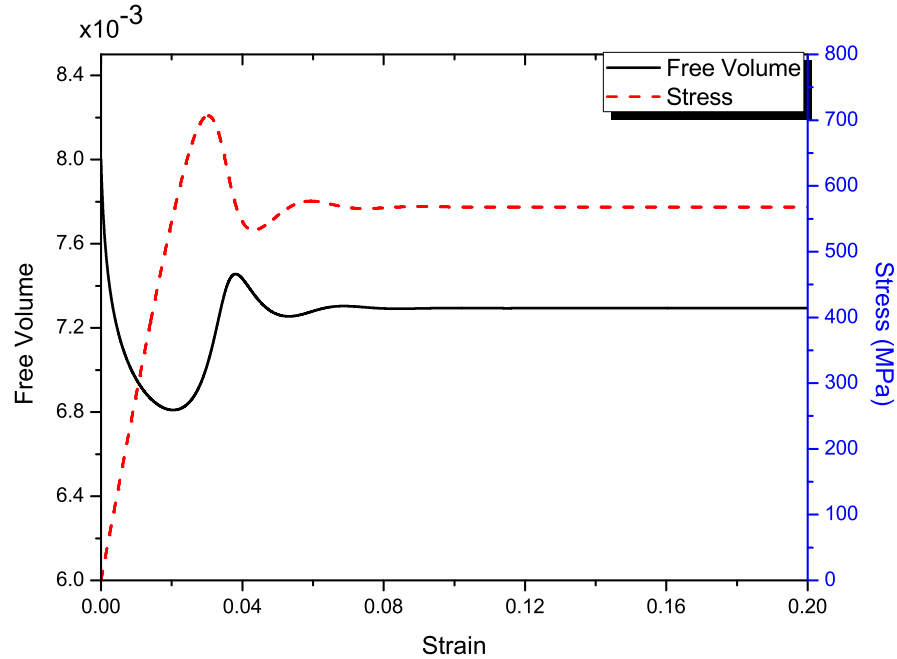


Figure 27: Free volume prediction of the free volume concentration and the stress versus strain of Zr-based bulk metallic glass at temperature of 698K. The black solid line is the free volume concentration, while the red dash line is the stress.

creation induced by the applied stress and the free volume annihilation caused by the structural rearrangements. Eventually, the system reaches a steady state, where both the free volume concentration and the stress are constant and the metallic glass flows like a liquid.

As Equation 20 and 21 show, the stress and the free volume concentration are coupled. The free volume concentration value depends on the prescribed strain rate, and the environmental temperature. Also the initial conditions, such as the initial free volume concentration and the free volume annihilation rate strongly depend on the system temperature. The value of those parameters change with the change of temperature.

3.4.2 Inhomogeneous deformation

As described by Schuh and Argon[135, 2], the stress-strain relations and the deformation modes depend on the loading condition and the environmental temperature. When the sample is under high temperature and low strain rate condition, the plastic deformation mechanism of the metallic glass is characterized by homogeneous deformation, which has been discussed in the previous section. The free volume concentration can reach a steady state, and the specimen deforms homogeneously. However, when the strain rate is in the dynamic region or the temperature is much lower than the glass transition temperature, the specimen go through inhomogeneous deformation. During the low temperature loading, the free volume distribution of the system is not uniform, which introduces the free volume perturbation inside the specimen. This free volume concentration perturbation and the high imposed strain rate induce a large free volume concentration increase, which causes the sample to have catastrophic failure. That is to say, in such a case, inhomogeneous plastic deformation occurs, and the specimen will fail through a fast propagation of the shear band.

Apart from the free volume model proposed by Spaepen[147], Argon[2] has introduced the shear transformation zone (STZ) model to explain the plastic deformation of metallic glasses. The plastic deformation of metallic glasses on the macroscopic scale is a process of accumulation of local strain through the operation of shear transformation zone and the redistribution of the free volume. The increase of the environmental temperature would assist in overcoming the energy barrier for the shear

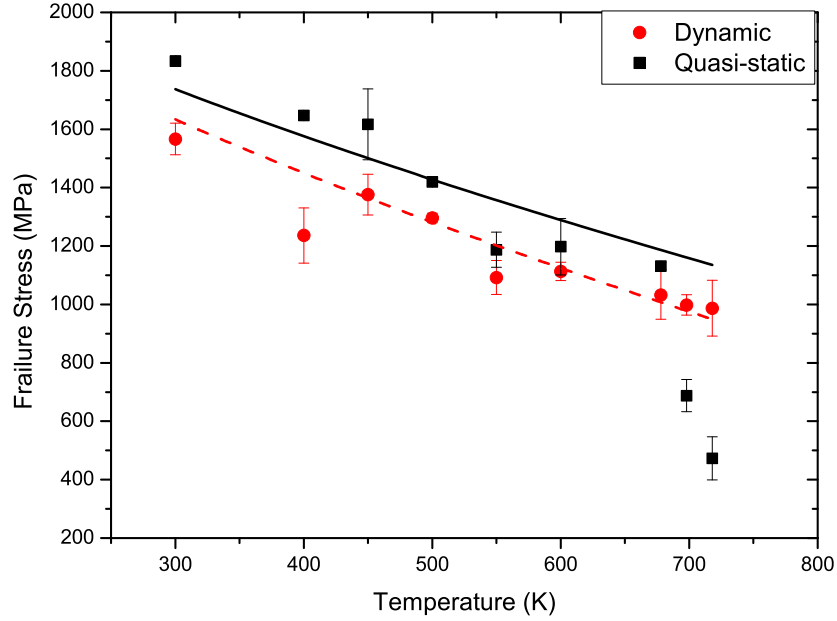


Figure 28: The failure stress of quasi-static and dynamic loading of $Zr_{55}Ni_5Al_{10}Cu_{30}$ at different temperatures, and the solid and dash lines denote the fit of Equation 24 for quasi-static and dynamic, respectively.

of STZ, and allow plastic yield to happen at a lower stress[135]. To identify the test environment effect such as temperature and strain rate on the fracture stress of metallic glasses, Johnson and Samwer[68] proposed a cooperative shear model (CSM) based on the idea of the shear transformation zone model. They related the yield shear stress of the metallic glass τ_{CT} to the temperature T and the shear strain rate $\dot{\gamma}$, and the relationship can be expressed by the following equation:[68]

$$\tau_{CT} = \tau_{C0} - \tau_{C0} \left(\frac{k}{\beta} \frac{G_{0T}}{G_{0T_g}} \ln \frac{\omega_0}{C\dot{\gamma}} \right)^{2/3} t^{2/3} \quad (23)$$

where τ_{C0} is the critical yield shear stress at $T = 0K$, $\dot{\gamma}$ is the shear strain rate, G_{0T} and G_{0T_g} are the shear modulus at a finite temperature and the glass transition

temperature, respectively. Parameter t in Equation 23 is the ratio of the finite temperature T (or temperature of interest) and glass transition temperature T_g , ω_0 is the atomic vibration frequency, and C and β are constants. From the stress-strain curve of the tested metallic glass specimens, there is no strain hardening found, and thus the failure stress is equivalent to the yield stress. Equation 23 is also suitable for the failure stress. Then the uniaxial compressive failure stress of the Zr-based metallic glass σ can be represented as:

$$\sigma = \sigma_0 (1 - Dt^{2/3}) \quad (24)$$

where σ_0 is the uniaxial compressive failure stress under quasi-static loading at temperature $T = 0K$, and $D = (k/\beta)\ln(\omega_0/C\dot{\gamma}) \times (G_{0T}/G_{0T_g})$. Using Equation 24, the experimental data from quasi-static and dynamic experiments was fitted with two different D values, as shown in Figure 28. It is found that the two points during the quasi-static loading at high temperature are far away from the fitting curve, which indicates that a different deformation mechanism may be responsible. Under this low strain rate and high temperature condition, the specimen deforms homogeneously as we have discussed in the previous section. The fitting results suggested that the critical uniaxial compressive failure stress at $T = 0K$ is about 2500 MPa. The D values for quasi-static and dynamic compressive experiments are fitted to be 0.6056 and 0.5332, respectively. These fitting results are in good agreement with the results reported by Liu et al.[100]. The discrepancy of the D values under the two loading conditions is caused by the different imposed strain rates. Since the parameter D is

related to the strain rate of the experiments, the value increases with decreasing the strain rate.

3.5 Conclusion

In this chapter we have investigated the coupled effects of strain rate and temperature on the mechanical behavior of $Zr_{55}Ni_5Al_{10}Cu_{30}$ bulk metallic glass. Mechanical testings were performed at various temperatures, from room temperature to elevated temperatures even above the glass transition temperature of the specific metallic glass, at both quasi-static and dynamic strain rates. The effect of the testing temperature on the failure stress of this Zr-based metallic glass was mainly discussed. The results show that the failure stress goes down with increasing environmental temperature, while the dynamic fracture stress is always less than that measured under quasi-static condition, except when the temperature is around the glass transition temperature.

A transition from inhomogeneous to homogeneous plastic deformation has been observed during the quasi-static compressive experiments when the testing temperature is elevated to the glass transition temperature. The free volume model has been successfully applied to simulate the homogeneous deformation behavior under such condition. The deformation is found to be controlled by the competition between the stress induced free volume and the free volume annihilation caused by the atomic jumps. Free volume concentration will reach a steady state and so does the stress profile of the specimen.

When temperature is low or the strain rate is high, the specimen will deform inhomogeneous by shear banding processes. The cooperative shear model[68] was

used to fit the experimental results. A temperature dependence of the failure stress of the specimen is found and the fitting parameter is related to the imposed strain rate.

CHAPTER 4: INSTRUMENTED NANOINDENTATION EXPERIMENTS OF BULK METALLIC GLASS

4.1 Introduction

4.1.1 Instrumented Nanoindentation

Since its advent, the instrumented nanoindentation technique has been widely used to characterize the mechanical properties of different materials at nanometer scale, such as very thin films. In what follows, we will review the basic working principle of the nanoindentation, and the cautions and caveats associated with this technique.

The elastic contact problem plays an essential role in analyzing the process and data treatment of nanoindentation as well as other indentation experiments. Hertz had analyzed the problem of the elastic contact between two spherical surface with different radius and Young's modulus. His results provided a fundamental framework for further and later studies on the general problem of nanoindentation[125]. The Hertz equation which establishes the relationship between the displacement of the indentation and the load is:

$$P = \alpha h^m \tag{25}$$

where P is the load applied to the indenter tip, h is the elastic displacement of the indenter and α is a constant. The exponent m is a constant determined by the

geometry of the indenter. For example, $m = 1$ for a flat punch indenter; $m = 1.5$ for a spherical indenter and $m = 2$ for a conical indenter.

With the excellent force and displacement resolution of modern nanoindentation, the load vs. displacement curve for a nanoindentation experiment can be obtained by the load and displacement sensors based on various principles and devices. A typical load-displacement curve is shown in Figure 29. The unloading part of the curve is assumed to be elastic and the stiffness of the initial part of the unloading curve is given by[125]:

$$S = \frac{dP}{dh} = \frac{2}{\sqrt{\pi}} E_r \sqrt{A} \quad (26)$$

where S is the initial slope of the unloading curve shown in Figure 29, E_r is the reduced modulus which is related to the Young's modulus of the the sample and the indenter, and the A is the projected area of the elastic contact. According to Pharr and Oliver, the contact area A can be determined by the area function of the indentation tip which is related to the displacement h and the area function of a specific indenter tip can be calibrated with standard specimens on a regular basis to ensure its accuracy. From Equation 26, the reduced modulus E_r can be calculated and then the Young's modulus of the specimen can be obtained by the following equation:

$$\frac{1}{E_r} = \frac{(1 - \nu^2)}{E} + \frac{(1 - \nu_i^2)}{E_i} \quad (27)$$

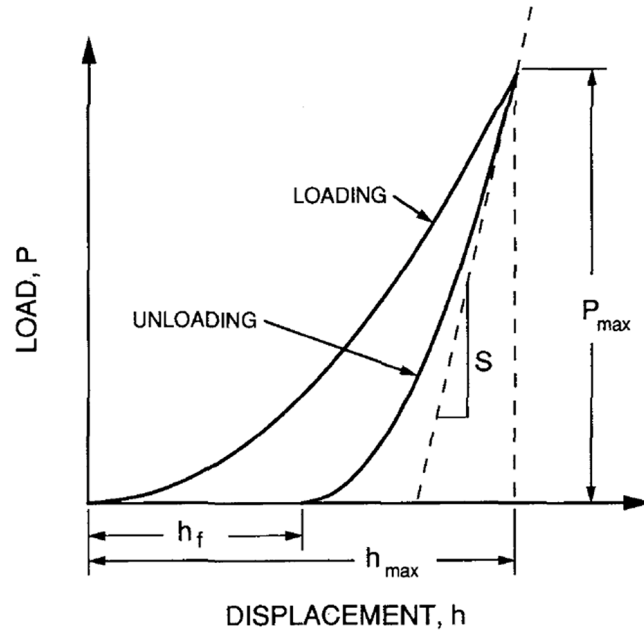


Figure 29: A typical load-displacement curve of nanoindentation result[125].

$$H = \frac{P_{max}}{A} \quad (28)$$

where E and ν are the Young's modulus and Poisson's ratio of the specimen and E_i and ν_i are the same parameters for the indenter. Also the hardness of the specimen can be determined by Equation 28, where P_{max} is the peak load during the indentation process.

4.1.2 Applications of Instrumented Nanoindentation

With the ability of acquiring high resolution load and displacement data, instrumented nanoindentation has been widely used to probe the hardness and elastic modulus of small volumes[125, 126]. It has also been applied to evaluation of other mechanical properties such as creep parameters[108, 34] and strain rate sensitivity[128, 30]. Because of the small volume of the material tested in a nanoindentation experi-

ment and the high resolution load and displacement data, the fundamental of material's mechanical behavior can be revealed at nanometer scale. The initial deviation from elastic contact shown as a "pop-in" event during the nanoindentation process has been observed on (0001)-oriented single crystals of 4H-SiC,[137], which indicates the transition from elastic deformation to plastic deformation. Similar displacement burst events have also been observed in different bulk metallic glasses systems[132, 134, 97, 119, 48]. The discrete displacement bursts have been related to the operation of individual shear banding events, which are similar to the stress serrations, observed during quasi-static uniaxial compression test of bulk metallic glass specimens.

The serrated flow during the nanoindentation test has been found to be strongly related to the alloy composition and the applied strain rate[132]. The transition from discrete plastic flow to continuous plastic deformation when the imposed indentation strain rate is increased beyond a certain level has been explained in Schuh's work[132]. The hardness evolution during nanoindentation has been reported by Huang et al.[48], in whose work a strain softening effect has been observed. Huang and coworkers attributed this strain softening to the accumulation of free volume inside the material. However, strain hardening effect has been reported by Yang et al.[175]. In the work of Yang and coworkers, cyclic indentation load was applied to the specimen and hardening effect happened during each reloading cycle. What is more, the hardening effect is independent of the loading rate.

In this work, we will applied the instrumented nanoindentation technique to a Zr-based bulk metallic glass. Different test methods were applied to reveal the load-

displacement relationship and to also examine the hardness profiles of the specimen. Serrated flow has been found in the low strain rate nanoindentation experiments. A clear transition from discrete to continuous plastic deformation has been observed due to the transition of the plastic deformation mode. Hardness evolution was found during the low strain rate nanoindentation test, suggesting that the deformation mechanism difference between the low strain rate and high strain rate loading conditions.

4.2 Experimental Procedure

To achieve a better understanding of the mechanical behavior, particularly the plastic deformation mechanisms associated with the bulk metallic glasses, we have examined the material using the MTS (now Agilent) Nano Indenter G200 system with different test methods. The cylindrical bars of Zr-based bulk metallic glass was cut into 2mm thick disks and polished with sand paper followed by diamond polish paper. A final surface finish is about $0.1 \mu\text{m}$ and then the sample was polished on a polishing cloth with $0.03 \mu\text{m}$ alumina suspension. In what follows, we will describe the experimental details, especially the experimental methods we have used, including the loading-control, displacement-control and the strain rate jump experiments. Two workspaces have been used during the tests. One is the XP workspace, where a Berkovich diamond indenter tip was used, and the displacement resolution is better than 0.01nm while the load resolution is about 50nN . Compared to the XP workspace, the DCM workspace has an improved resolution in both the force and the displacement. In addition, it has decreased the sensitivity to environmental noise

such as mechanical vibration and thermal fluctuation. The displacement resolution for the DCM is about 0.0002nm and the load resolution is about 1.0 nN. A smaller Berkovich diamond indenter tip has been used for the DCM workspace.

4.2.1 Load Control DCM Method

The DCM workspace has been chosen to perform the load control Nanoindentation experiment. The area function of the Berkovich tip is calibrated using fused silica as a standard sample. After the calibration, the tip was brought into contact with the Zr-based bulk metallic glass specimen surface before the prescribed 0.05nm/s drift rate has been reached. A maximum load of 10mN has been setup for the loading process with different loading time in order to produce different loading rates. Loading rates from 0.005 to 10mN/s have been applied. After the maximum load has been achieved, the tip was held for 10 s at the maximum load before unloading. Then the tip was unloaded to 90% of the maximum load, and then the tip was held there for 10s to measure the thermal drift. After that, the tip was further unloaded to zero load. At each loading rate, eight indents have been made. The time, load and displacement information has been recorded by the system for subsequent data processing.

4.2.2 Displacement-Control CSM Method

In addition to using the load control method, the displacement-control continuous stiffness measurement (CSM) method has also been applied to reveal the load and displacement relationships. It is also used to evaluate the hardness and modulus profiles of the specimen. Compared to the load-control method, in which the hardness and modulus values are obtained from the initial part of the unloading curve, as we have

described in the previous section, the displacement-control CSM method will produce a continuous hardness and elastic modulus profiles as a function of the displacement into the specimen. This method will generate more accurate hardness and modulus results vis-a-vis the load-control approach. The same DCM workspace has been used to perform the displacement control experiments. The maximum displacement and the strain rate are pre-defined. In an instrumented nanoindentation experiment, the indentation strain rate can be calculated by the following equation[108]:

$$\dot{\epsilon} = \frac{\dot{h}}{h} = \frac{1}{2} \left(\frac{\dot{P}}{P} - \frac{\dot{H}}{H} \right) \approx \frac{1}{2} \frac{\dot{P}}{P} \quad (29)$$

where \dot{h} is the displacement rate, h is the indentation depth (displacement of the tip into the specimen surface), \dot{P} is the loading rate, P is the load on specimen, \dot{H} is the rate of hardness change during the indentation process, and H is the hardness value of the specimen at this depth. The loading rate of the instrument is controlled in order to satisfy the pre-described strain rate. Five different strain rates were used with the displacement control method, which are 0.0005, 0.001, 0.01, 0.05 and 0.1 1/s. The maximum displacement was set at 400nm for all the strain rates. The thermal drift was also measured when the indenter was unloaded to 90% of the maximum load.

4.2.3 Strain Rate Jump XP Method

A strain rate jump technique[111] has been developed and applied to determine the strain rate sensitivity (SRS) of the Zr-based bulk metallic glass of this work. The method is based on the XP workspace. The larger tip size utilized in this method

will allow a larger indentation depth to be reached during the experiment. The CSM method was used during the experiment, but instead of using a constant strain rate during each indentation, abrupt strain rate change (strain rate jump) was conducted several times in order to produce an in-situ hardness versus strain rate data. The XP Berkovich diamond tip was set up to indent into the specimen with an initial depth of 1400 nm with a constant strain rate of 0.05 1/s. In this step, the long travel distance of the indenter tip is to ensure the stabilization of the system. After the system is stabilized, the strain rate will be changed to 0.014 1/s, and the penetration depth at this strain rate is 300 nm. Then the strain rate jumps back to 0.05 1/s, so as to compare the hardness value with the previous value at the same strain rate, in order to obtain a reliable data. After the indenter tip travels another 300 nm, the strain rate down jumps to a lower value, 0.004 1/s for another 300 nm. Then the strain rate jumps back to 0.05 1/s again for yet another 300 nm. At the end, the strain rate will be changed to the minimum value, 0.001 1/s, and after 300 nm displacement, the strain rate will jump back to 0.05 1/s again. All the hardness values will be recorded using the CSM method, and the relationship between the strain rate and the indentation displacement into specimen relationship is shown in Figure 30.

4.3 Experimental Results

A series of indentations were made with different test methods listed below with a Berkovich indenter. Figure 31 is the topographic image of a typical nanoindentation site, and the right hand side is the profile of the cross section of the indentation site shown on the left hand side measured from atomic force microscopy (AFM).

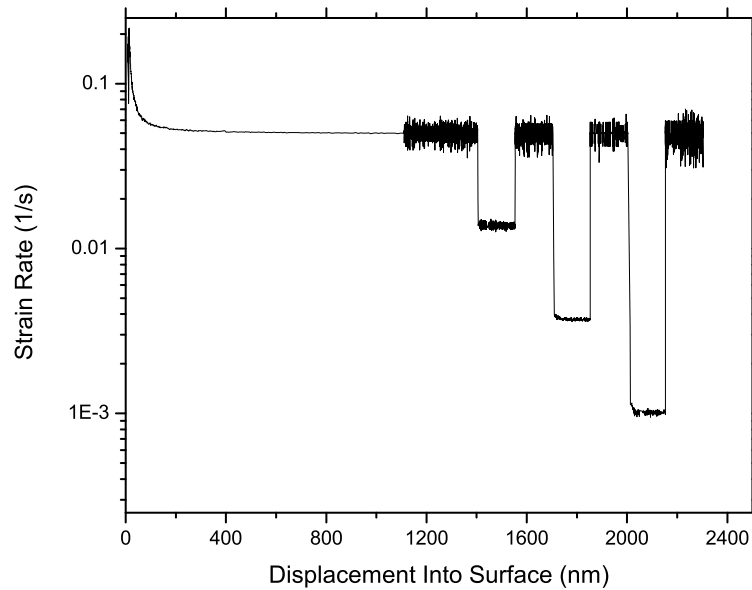


Figure 30: Strain rate is plotted as a function of the displacement into specimen during the strain rate jump test using nanoindentation.

Pile-up is clearly observed with the profile curve, and the topographic image of the indentation shows pile-up on each side of the indentation site. And the topographic image shows multiple pile-up events occurred around the indenter. Since the material is amorphous, there should be no strain hardening; it is much easier for the material to flow up around the indenter tip than to displace under the tip[115]. The details of the experimental results using different nanoindentation protocols will be presented and discussed below.

4.3.1 Results from Load-control DCM Method

The load-displacement (P-h) curves from nanoindentation experiments on the Zr-based bulk metallic glass are plotted in Figure 32. In this figure, the origin of each curve has been offset in the horizontal axis with a certain value so that multiple curves

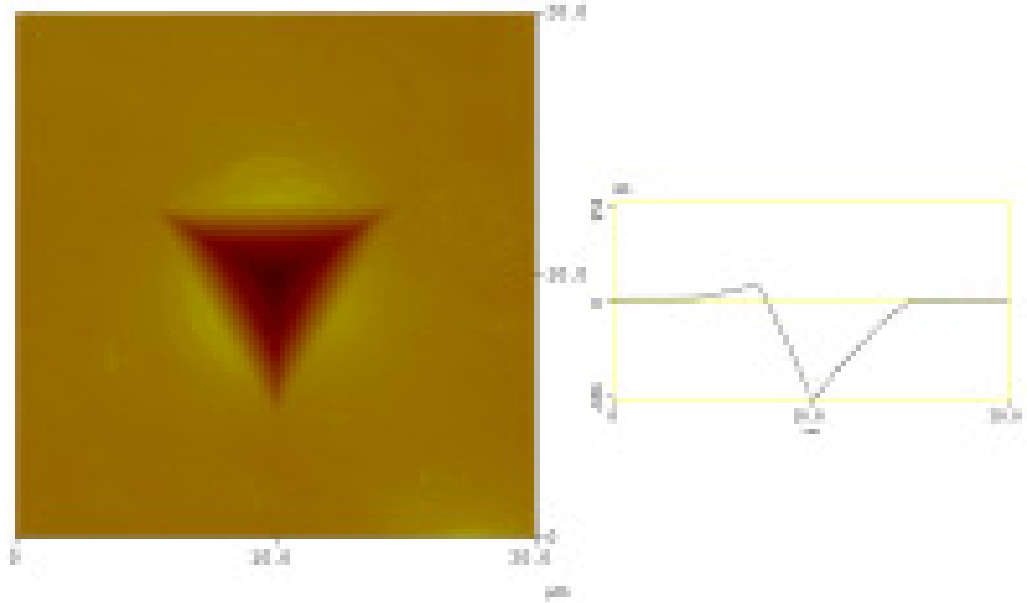


Figure 31: An typical AFM image of an indentation site is shown on the left. AFM profile of the the cross-section of the indentation is shown on the right. Both images show the material pile-up along the side of the triangular indentation.

can be displayed on a single graph, and the unloading portions of the experiment are not plotted for clarity. The left most curve represents the result from the smallest loading rate, 0.005mN/s. From left to right, the loading rate increases, with the right most curve having the highest loading rate of 10mN/s. The results in Figure 32 show discrete and rapid bursts of displacement at constant load at relatively low loading rates. This behavior is reminiscent of the serrated flow during the uniaxial compressive test on the same alloy, which has been discussed in Chapter Two of this thesis. In a compression experiment, usually displacement control mode is employed, and the serration or fluctuation of the applied force corresponds to the operation of individual shear band that quickly accommodates the applied strain. During nanoindentation tests such as in this work, usually the load is controlled by the system during the experiment, and therefore the serrated flow manifests itself by the displacement bursts.

Similar pop-ins events during the nanoindentation of bulk metallic glasses have also been reported by many other researchers [37, 132, 175].

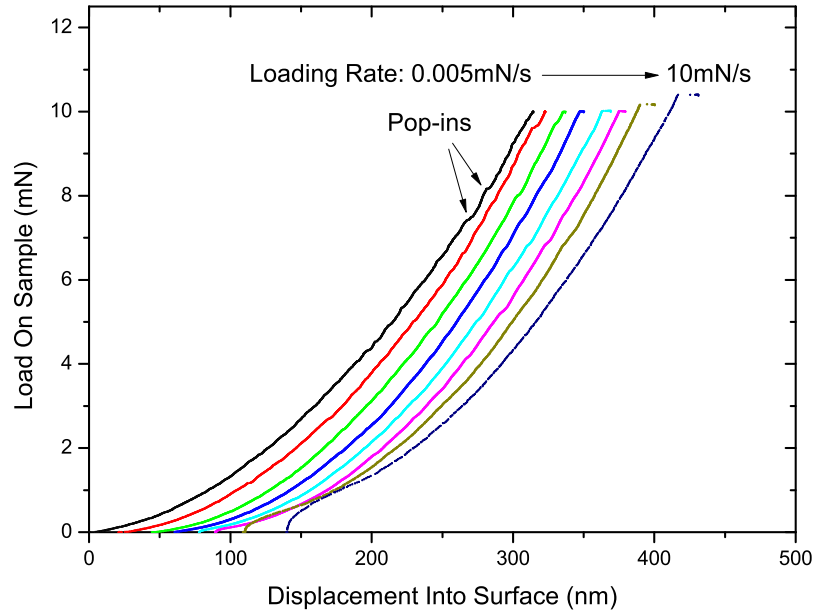


Figure 32: Typical load-displacement (P-h) curves measured on the loading portion of nanoindentation experiments for Zr-based metallic glass. Curves are offset from the origin for clear viewing and the loading rate most left curve represent the smallest loading rate and the most right curve represented the highest loading rate.

From Figure 32, we can find that the displacement burst during each pop-in event is a function of the indentation depth. According to Schuh et al.[132], this is a result of the increasing length scale of the indentation geometry. The number of the pop-in event is a function of the loading rate. When the loading rate is small, more discrete bursts on the load-displacement curve can be observed. However, when the loading rate is high, as shown in Figure 32, for example when loading rate is 10mN/s, a smooth parabolic curves is measured.

The maximum displacement during each test segment has also been recorded, and

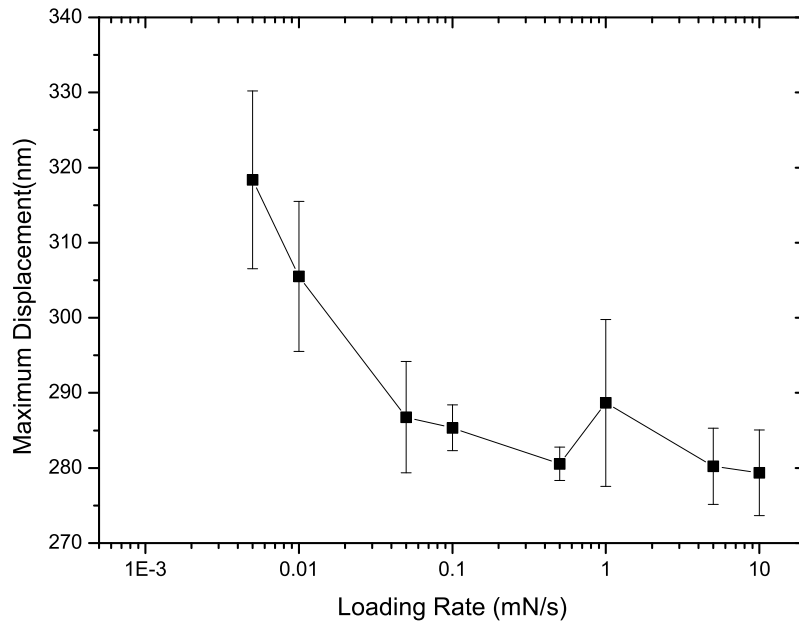


Figure 33: Maximum displacements were plotted as a function of loading rate for the Zr-based bulk metallic glass. The Maximum load at each loading rate was the same, i.e., 10mN. The general trend is that the maximum indentation depth decreases with increased indentation rate. According to the definition of indentation hardness, it then suggests that the hardness of the Zr-based bulk metallic glass has a significant loading rate effect.

the average values corresponding to each loading rate with the error bars are plotted as a function of the loading rate. Figure 33 suggests that the maximum displacement decreases as the loading rate increases. Furthermore, when the loading rate is greater than 0.5 mN/s, the maximum displacement will fluctuate. This trend is still true even after the tip has been held at the maximum load for 10 seconds. Since at the same maximum load, a shallow indentation depth points to a smaller contact area, and in turn, according to the definition of indentation hardness, a smaller hardness value, therefore, Figure 33 is suggesting a significant strain rate effect on the hardness of the Zr-based bulk metallic glass.

4.3.2 Results from Displacement-control CSM Method

Figure 34 and 35 display the plots of hardness and loading histories as a function of displacement into the specimen at two different strain rates, $1 \times 10^{-3} s^{-1}$ and $1 \times 10^{-1} s^{-1}$, respectively. When the strain rate is $1 \times 10^{-3} s^{-1}$, both the hardness and load curves are serrated. The loading history is similar to the loading curve at a lower loading rate condition. The displacement bursts here should represent the formation of single shear band. The hardness serration happens at the same time as the displacement burst takes place, which can be observed in Figure 34 on the right hand side. When a displacement burst occurs, it is followed by an immediate drop in the hardness value. However, right after the hardness drop, the value increase back to a high value. The overall trend of the hardness at this strain rate shown in Figure 34 reveals that the hardness increases as indenter depth is increased.

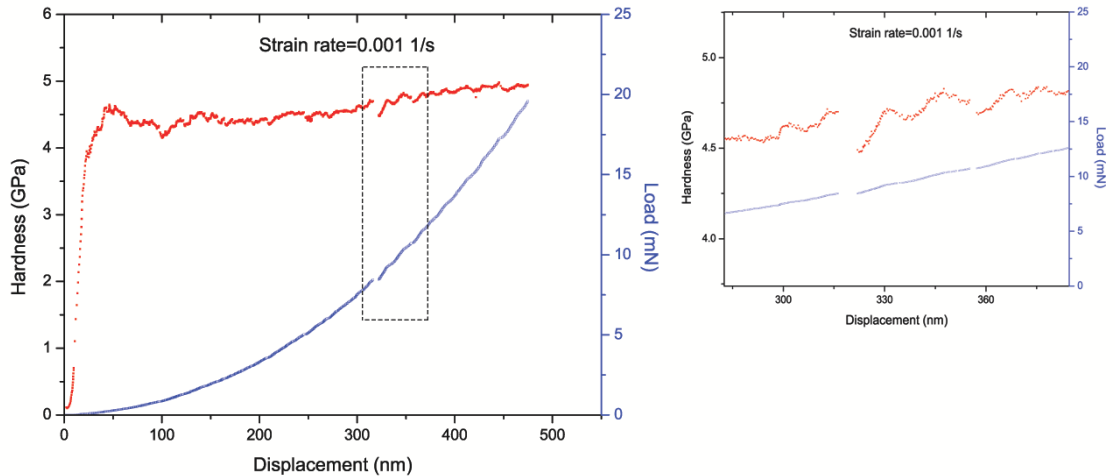


Figure 34: Hardness (red curve) and load (blue curve) profiles are plotted as a function of the displacement from the nanoindentation experiment using displacement control CSM method. The strain rate of the indentation experiment is $1 \times 10^{-3} s^{-1}$. The right hand side plot is the enlarged view of the boxed region of the left hand side plot.

When the imposed strain rate of the nanoindentation test was increased to 0.1 1/s, unlike the increased hardness in the profile from the low strain rate test shown in Figure 34, the hardness value as a function of the displacement was quite uniform. Actually, after 150 nm, the hardness will not change with further increase in the displacement (Figure 35). The hardness serration has disappeared, and gives way to the smooth load-displacement curve presented in Figure 35. Therefore, here we have observed a transition from discrete plastic activities to continuous plastic deformation in the Zr-based bulk metallic glass when the imposed indentation strain rate is increased beyond a critical level. The same transition from discrete to continuous yielding has also been observed during the load control nanoindentation test. The hardness measured from the high strain rate nanoindentation is larger than that from lower strain rate. From the results of the three nanoindentation experiments at different strain rates, the strain rate sensitivity has been calculated using Equation 4. For the Zr-based bulk metallic glasses investigated in this thesis, the m value is calculated to be 0.064, which is quite remarkable, as it compares to the SRS values of annealed metals of body center cubic (bcc) structure, which are known to be strongly rate dependent[160, 164]. Compared to the strain rate sensitivity obtained from the quasi-static compressive experiments, this m value is significantly larger, the reason for which will be discussed in the following section.

4.3.3 Results from Strain Rate Jump XP Method

Nanohardness values have also been obtained from nanoindentation experiments with strain rate jumps using an XP tip. With four different imposed strain rates dur-

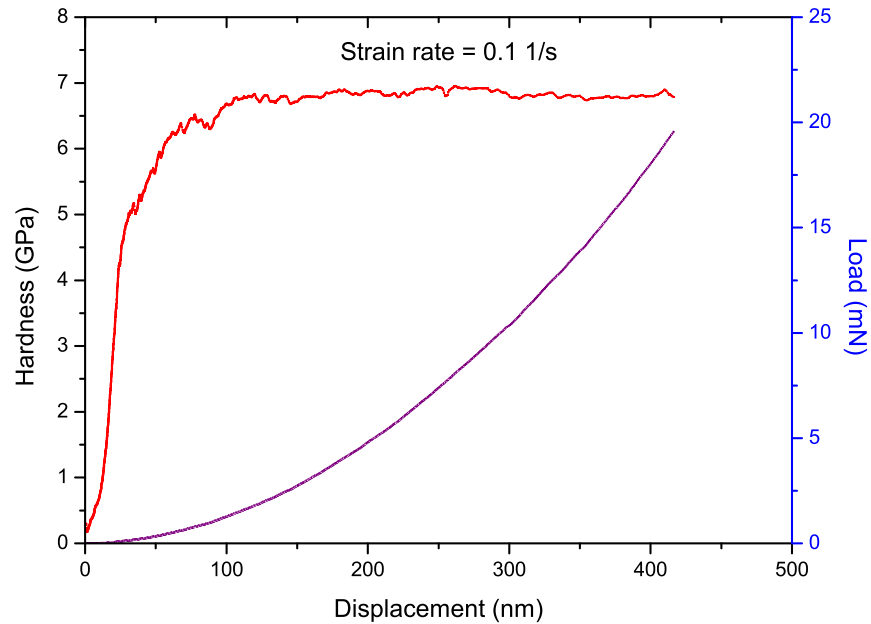


Figure 35: Hardness (red curve) and load (purple curve) profiles are plotted as a function of the displacement from the nanoindentation experiment using the displacement control CSM method. The strain rate of the indentation experiment is $1 \times 10^{-1} s^{-1}$. Compared to the results presented in Figure ??, here no obvious serration can be observed either in the hardness curve or the load curve, indicating that plastic deformation is continuous and uniform.

ing a single pre-designed experimental protocol, the hardness values can be measured as a function of the imposed indentation strain rate. Some results from such experiments are plotted as a function of strain rate shown in Figure 36. Both axes are in logarithmic scale, and the strain rate sensitivity based on the strain rate jump experiments is calculated to be $m = 0.0103$. Compared to the experimental results from the constant strain rate test of nanoindentation and quasi-static compressive test, this strain rate sensitivity value is much lower. And this value is also almost identical to the m value reported by Pan et al.[128], also using instrumented nanoindentation.

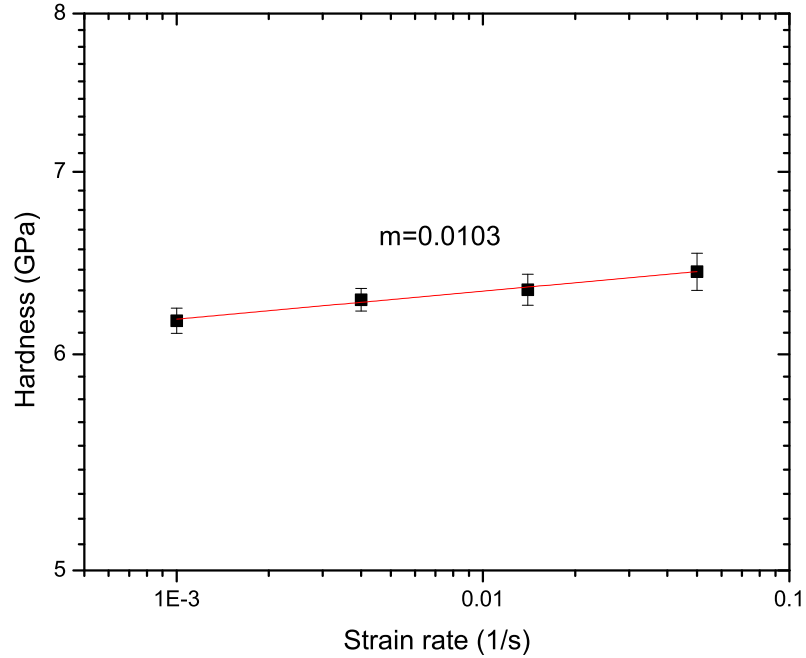


Figure 36: Hardness values are plotted as a function of the imposed strain rate from the nanoindentation strain rate jump experiments. Note that in the figure, both the strain rate and the hardness are in logarithmic scale. All the data points fall on the red straight line, and therefore, the slope of the straight line is the strain rate sensitivity of the specimen.

4.4 Discussion

4.4.1 Flow Serration

Nanoindentation experiments have been performed on various bulk metallic glasses by different researchers. Serration in the load-displacement curves has been reported with different BMG system with different indentation tips by these researchers. The first such report was published by Golovin et al.[37] who conducted nanoindentation experiments on the Pd-based metallic glass. Bei et al.[5] have reported serrated flow during the nanoindentation test of Vit 1 with a spherical indenter. How-

ever, Vaidyanathan et al.[154] suggested that there was no serration in the load-displacement data when using a Berkovich tip. Schuh et al.[134, 132] have studied the serrated flow during nanoindentation as a function of the loading rate. They found that a transition from serrated flow to a continuous deformation mode occurred during the nanoindentation experiments as the loading rate increased beyond a certain level. But, Greer and his co-workers[38] suggested that the absence of serrated flow at high loading rate was not due to the deformation transition; instead, the apparent absence of the steps was caused by the instrumental inaccuracy.

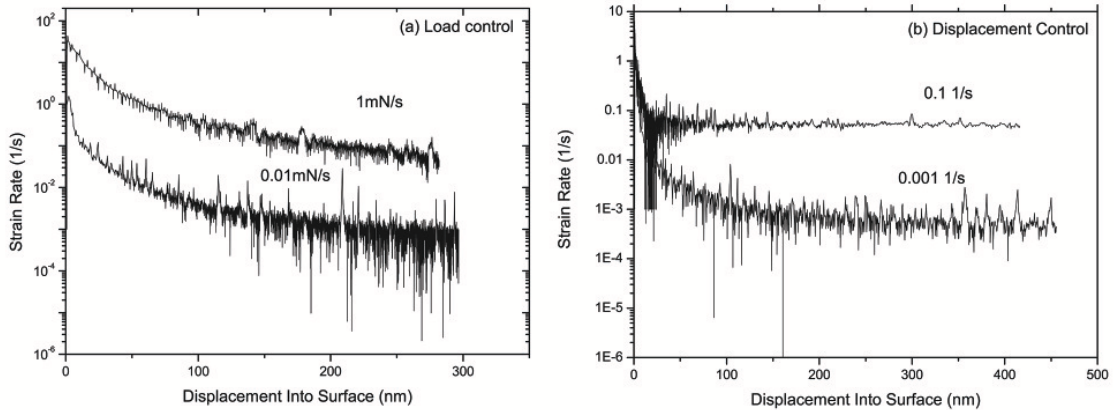


Figure 37: The nanoindentation strain rate plotted as a function of displacement into sample for (a) load control method and (b) displacement control method. The loading rate or the pre-described strain rate indicated by the insert text. Strain rate peaks are observed at both method with low rate, those strain rate peaks correspond to the serration flow observed in Figure 32 and 34.

In this work, however, serration in the load-displacement curves has indeed been observed both in the constant loading rate mode, and in the constant strain rate control tests, as shown in Figure 32 and 34. According to Equation 29, the indentation strain rate is calculated and plotted as a function of the displacement into the specimen surface in Figure 37. At the beginning of each experiment, since $h = 0$, the

initial strain rate is effectively infinite. However, as h increases, the strain rate during the loading control test decreases. As demonstrated by Figure 37, numerous short strain rate spikes appear at the low loading rate (and accordingly, low strain rate experiments). Those short strain rate spikes represented rapid displacement during the tests, which are the same pop-in events shown in the load-displacement curves. Both the quantity and the magnitude of the bursts are related to the strain rate and the loading rate. As Figure 37(b) illustrates, when strain rate $\dot{\epsilon} = 0.1s^{-1}$, the strain rate burst almost disappears. The same trend also stands when we increase the loading rate. It is worth noting that the strain rate or loading rate needed to suppress the serrated flow is not a constant value for all metallic glasses, as Liu et al.[97], Schuh et al.[132] and Wei et al.[159] have suggested that the serrated flow phenomenon is also related to the chemical composition of the material.

The transition from serrated flow to continuous flow during the nanoindentation tests suggests a change in the nature of plastic deformation of the metallic glass. The serrated flows exhibited in Figures 32 and 34 and the strain rate bursts shown in Figure 37 represent the formation of single shear band at low strain rates. On the other hand, as the strain rates increases, more smooth curves suggest simultaneous operation of multiply shear bands at higher strain rates. The same transition has been reported by Drozd and co-workers [29] also in nanoindentation experiments. Mukai et al.[117] have investigated the Pd-based metallic glass under tensile load, and they found that the specimen failed with a single shear band under quasi-static condition, while simultaneous operation of multiple shear bands was observed during dynamic strain rate experiments.

As explained by Wright et al.[165], during the nanoindentation of a metallic glass specimen, the initial response of the material is elastic, and the duration of elastic deformation depends on both the material and also the shape of the indentation tip. Once the stress state satisfies the critical stress defined by Mohr-Coulomb criterion, a shear band is initiated. The first displacement burst is found at a displacement of 20 nm when the loading rate is 0.005 mN/s. When the strain rate is low, the initial single shear band can rapidly accommodate the imposed strain, which produces the distinct strain burst shown in Figure 37. In contrast, if the applied strain rate has exceeded the strain rate of relaxation of the single shear band, then the individual operation of one shear band will not satisfy the imposed strain rate, as the first shear band is still propagating. When the stress level exceeds the yield criterion again, and another shear band is initiated, which means multiple shear bands were activated simultaneously, leading to the disappearance of serration.

The above explanation is consistent with the observation from our uniaxial compressive experiments, as well as the previous work performed by other researchers. Although investigations on the Zr-based metallic glasses using nanoindentation by other researchers[154, 165] have not reported about the serrated flow, it could be argued that it is because of the high applied loading rates in those efforts. We believe that at sufficiently low strain rates, the strain burst will be observed. However, Greer et al.[38] argued that the disappearance of the serrated flow at relatively high strain rate is due to the limited resolution of displacement and load, as well as data acquisition rate associated with the nanoindenters available to the research community. In the present thesis work, the maximum data acquisition rate is $4 \times 10^3 Hz$, which should

produce sufficient data points even at the highest loading and strain rate. However, still no serrated flow has been observed at such loading rates. The strain rate due to the operation of a single shear band is not expected to be a single value, which is also reported by Schuh et al.[132]. The strain rate within the shear band is a strong function of the local arrangements of atoms within the metallic glass, i.e. the free volume concentration. The change of the free volume concentration inside the metallic glass may be caused by temperature increase or the stress-strain field change[147]. First, we consider the temperature increase inside the shear band. For nanoindentation test, the temperature increase within the shear band can be estimated by Eshelby and Pratt's equation[31]:

$$\Delta T = \frac{H\dot{\gamma}_b h}{6\pi k} \sqrt{\frac{\pi k \Delta\gamma_b}{c_p \dot{\gamma}_b}} \quad (30)$$

where H is the nanohardness value measured from the nanoindentation experiments, k and c_p are the thermal conductivity and specific heat of the metallic glass, respectively, $\dot{\gamma}_b$ is the shear strain rate inside the shear band and the h and $\Delta\gamma_b$ are the thickness of the shear band and the total shear strain inside the band, respectively. For the bulk metallic glass $Zr_{55}Al_{10}Ni_5Cu_{30}$ used in this work, the average hardness is about 6.2 GPa, which is taken from the average value of all the nanoindentation results. The strain rate inside the shear band can be approximately taken as $10^3 s^{-1}$ [122], and the thickness of the shear band can be measured directly from the AFM image of the indentation site (Figure31), which yields approximately a value of 20 nm, which is consistent with the measurement results from Refs.[97, 76]. The shear

strain inside the shear band can be calculated as $\Delta\gamma_b = \Delta h/h$, with a result of 0.1, where $\Delta h = 2nm$ for the magnitude of the displacement burst. The thermal conductivity and the specific heat of the metallic glass can be taken as $3.5 Jm^{-1}s^{-1}K^{-1}$ and $5.5 \times 10^6 Jm^{-3}K^{-1}$ for this specific Zr-based metallic glass[2, 96]. The temperature increase within the shear band can then be calculated to be only 0.03 K. Such estimates of negligible adiabatic temperature rise are also consistent with the calculation from our quasi-static compressive experiments. The negligible temperature increase within the shear band indicates that the change of free volume concentration should not be induced by the thermal effect but by the pressure effect.

4.4.2 Hardness Evolution

Hardness values of the Zr-based bulk metallic glass have been investigated at different strain rates. Two different methods have been used to reveal the strain rate effect on the metallic glass. The first method is indentation at different constant strain rates, and the second one is strain rate jump method in a pre-designed single indentation experiment. With both methods, the hardness shows a increase trend as the applied strain rate is increased. However, the strain rate sensitivity obtained from the constant strain rate method is about six times larger than the one measured by the strain rate jump test. To evaluate the accuracy of those data and explain this discrepancy, we have to use CSM model[68]. As discussed in Chapter 2, the shear transformation zone volume Ω can be represented by Equation 12. Here, the experimental results of the strain rate sensitivity from the constant strain rate and strain rate jump tests using the instrumented nanoindentation are 0.064 and 0.0103,

respectively. Plugging these two values into Equation 12, the shear transformation zone volume is calculated to be $0.79nm^3$ and $4.91nm^3$, respectively. According to the experimental results from Pan et al.[128] and the theoretical analysis of the shear transformation zone by Johnson and Samwer[68], the shear transformation zone is composed of about several hundreds of atoms, which will give a volume of the STZ on the order of about several nm^3 . In view of this, it seems that the constant strain rate nanoindentation has over estimated the strain rate sensitivity of this Zr-based bulk metallic glass. Our uniaxial compression experimental results also suggest the inaccuracy of the constant strain rate nanoindentation tests, and our compression experiments give a strain rate sensitivity $m = 0.022$, which is close to the value obtained from the strain rate jump test with nanoindentation.

The main reason of the inaccuracy during the constant indentation strain rate experiments is because of the thermal drift of the instrument. At the smallest imposed strain rate, $\dot{\epsilon} = 1 \times 10^{-3}$, the loading time is about 3000 s. With the allowable maximum drift rate of $0.05nm/s$, the total drift during the whole loading process is about 150nm, which is about 20% of the total displacement. This larger thermal drift effect will produce a lower hardness value during the low strain rate experiments and therefore spuriously increase the strain rate sensitivity. In contrast, the strain rate jump method only requires about 660 s to complete the experiment, which will significantly mitigate the thermal drift effect.

As discussed in Chapter 2, the typical stress-strain curve under compression does not exhibit any strain hardening. The absence of strain hardening was mainly caused by the absence of dislocations in the intrinsic amorphous structure of the metallic

glass material. However, the nanohardness profile from the low strain rate indentation experiments reveals increased hardness values as the displacement into specimen surface is increased (Figure 34). Prior researchers also reported such apparent strain hardening during the different test configurations of metallic glasses.

For example, Yang et al.[175] reported the observation of strain hardening and recovery in a Zr-based bulk metallic glass at room temperature. They applied cyclic instrumented nanoindentation loading to the specimen, and an increased hardness value was observed when the sample was reloaded immediately after unloading then gradually reduced to a stable value. Das and his co-workers[25] also reported the observation of significant increase in flow stress during the uniaxial compression test of a Cu-based metallic glass with a large plastic strain of 18%. Recently, Deng and Schuh[27] applied molecular dynamic (MD) simulation for nanoindentation test of Cu-based metallic glass. They also suggested the strain hardening effects during the test. The experimental results also suggested the hardening effect under the cyclic loading[127]. In contrast, Bei et al.[6] reported softening caused by the formation of profuse shear bands in a Zr-based metallic glass with a low glass transition temperature. They control the compressive strain of the specimen and performed hardness tests with respect to different compressive strains. They found that the hardness value decreased as the plastic strain is increased.

In this work, nanoindentation with the CSM method at a constant strain rate was used. At relatively low strain rates, such as 1×10^{-3} and $1 \times 10^{-2} \text{ s}^{-1}$, the hardness profile of the material shows an increase trend as the displacement is increased. Figure 34 shows the hardness as a function of the displacement, and the strain rate plot of

corresponding experiment shows that the system becomes stable after an indentation depth of 150 nm. The hardness value increases 11.7% compare the value from 200 nm and the hardness value from the maximum displacement. It is noted that the hardness increasing accompanied by the hardness serrated flow . Serrated flows are observed which happened at the same depth as the displacement burst occurred (Figure 34). Hardness value dropped suddenly with the formation of a single shear band and its subsequent propagation. After the shear band is arrested, the hardness value will increase to a higher level and then it is followed by another shear offset. This process is very similar to the deformation stage 1 shown in the uniaxial compressive results of Figure 13, although Song et al.[145] stated that the curvature during this stage was caused by random formation of shear bands, instead of any kind of hardening mechanism.

In order to describe the hardening mechanism during the low strain rate nanoindentation experiments, we need to understand the inhomogeneous deformation process associated with a metallic glass. It is well known that the plastic deformation of BMGs is through the formation of localized shear bands. It has been demonstrated that the mechanical plastic instability due to the formation of shear band was governed by the free volumes inside the metallic glass material[147, 2, 35, 32]. When the concentration of the free volume is larger than a critical value, shear band will form and propagate. The free volume evolution process can be described by the following equation proposed by Spaepen[147]:

$$\dot{v} = \nu^* f \exp\left(-\frac{\Delta G^m}{kT}\right) \exp\left(-\frac{\alpha_g \nu^*}{\nu_f}\right) \times \left[\frac{2\alpha_g kT}{\nu_f S} \left(\cosh \frac{\tau\Omega}{2kT}\right) - \frac{1}{n_D} \right] \quad (31)$$

where ν^* is the critical free volume required for an atomic jump, f is the jump frequency, ΔG^m is the activation energy of an atomic jump, k is the Boltzmann's constant, T is the temperature, α_g is the geometrical factor on the order of unity, S is related to the Poisson ratio ν and the shear modulus μ , Ω is the atomic volume and n_D is the number of diffusive jumps necessary to annihilate a free volume equal to ν^* . In Equation 31, the free volume change is a competition between the creation and annihilation of the free volume represented by the terms of $\frac{2\alpha_g kT}{\nu_f S} \left(\cosh \frac{\tau\Omega}{2kT}\right)$ and $\frac{1}{n_D}$, respectively.

In Equation 31, it is noticed that the free volume concentration is related to the temperature T and the free volume annihilation rate. Previous calculation has shown that the temperature increase during the shear band process at nanoindentation is very small, and the free volume annihilation rate at room temperature is always small compared with the free volume creation induced by the applied stress. Therefore the hardening effect may need to be considered from the structure evolution aspect. Since the applied strain rate is low enough to trigger the shear band individually (suggested by the displacement burst on the P-h curve), the hardness evolution can be explained by the individual shear banding process. Once the applied stress overcomes the initial activation energy of the structure barrier, flow dilatation will take place. Although the temperature effect is negligible, the shear-induced dilatation inside the actively deforming shear band will increase the local free volume and decrease the viscosity

significantly. As a consequence, the local atomic features and mobility characteristics may become similar to those at T_g of the alloy, which results in a large reduction of the interatomic interaction. The uniaxial compressive test results suggested that the viscosity value inside individual shear band during its formation process is equivalent to that under the condition of T_g . With the lowered viscosity, the shear band will propagate until the imposed strain has been accommodated, and then the shear band will be arrested and recovered. During the final stage of plastic deformation, the local atoms will rearrange, and Kim et al.[76] suggested that nanocrystallization will occur at the recovery stage. The formation of the nanocrystalline particles will increase the hardness of the material, which results in an increased hardness curve shown in Figure 34. The same deformation induced nanocrystallization and its influence on the work hardening in metallic glass composite under quasi-static compression tests has been reported by Lee et al.[84].

As to the observed hardness profile at relatively high strain rate (Figure 35), the disappearance of the hardening effect is due to the immaturity of the shear band process during the high strain rate indentation. As the applied strain rate exceeds the rate of relaxation of a single shear band, the first band will still be operating and has no time to go through recovery and as a consequence the atoms will have no time to rearrange themselves to form nanocrystalline particles. As the stress level exceeds the yield stress again, a second shear band is initiated. The absence of the nanocrystalline phase upon the high strain rate loading gives a uniform hardness profile. The immaturity of the shear band process under high strain rate loading is also proved by Figure 33, where during the low rate loading, the fully developed

shear bands produced a large displacement compared to that of high loading rate. It is worth of pointing out that the hardening during the nanoindentation may also be caused by the high density and the interaction of the shear bands beneath and around the sharp indenter[133, 25].

4.5 Conclusions

In this chapter, we have described and discussed the results from instrumented nanoindentation experiments of the Zr-based bulk metallic glass. Three different test methods have been used, including load control, displacement control and strain rate jump. During both the load control and displacement control experiments, serrated flow is manifests itself as a series of displacement burst. The discontinuities in the load-displacement curves suggest the operation of an individual shear band. Serrated flow is found to be a strong function of the applied strain rate. At relatively high loading and strain rate, flow serration is suppressed.

Strain rate sensitivity has been measured with different methods. The results suggested that the commonly used constant strain rate nanoindentation test produces an overestimate of the m value. Compared to results from the constant strain rate experiment, those from strain rate jump test via instrumented nanoindentation is more accurate.

Strain hardening has been observed during the low strain rate nanoindentation tests. The continuously increased hardness profile suggests the structure change during the plastic deformation process upon nanindentation. Nanocrystallization during the individual shear band formation can be used to explain the increased hardness

during the low strain rate indentation tests.

CHAPTER 5: MECHANICAL BEHAVIOR OF TUNGSTEN PARTICLE REINFORCED METALLIC GLASS COMPOSITE

5.1 Introduction

At room temperature, metallic glasses exhibit a high yield stress compare to their crystal counterpart. However, in most cases, this kind of material fails catastrophically under uniaxial loading, particularly in tension, due to localized shear banding. As a result, the plastic strain that a metallic glass specimen can sustain during either compressive or tensile loading is very limited, and the value is almost zero upon the tensile loading[62, 183]. As has been described in Chapter 2 of this thesis, the plastic strain prior to failure is less than 2% under quasi-static loading, and there is no strong evidence for significant plastic strain when the imposed strain rate is in the dynamic region (strain rate $\sim 10^3 s^{-1}$). The very much limited plastic strain has become the Achilles' heel of metallic glass. Various methods have been proposed to develop metallic glass based composite materials consisting of a metallic glass matrix with reinforcement of ductile second phase[42, 44, 15, 19, 33]. For example, Hays et al.[42] first reported a ductile metal reinforced bulk metallic glass matrix composite containing in situ formed dendrite dispersions. The plastic strain was significantly increased, which was attributed to the organized shear band patterns developed throughout the samples upon mechanical loading. Hofmann et al.[44] also reported that metallic glass matrix reinforced with ductile dendrite dispersions could exhibit significantly

increased toughness and tensile ductility. Beside in situ forming the second phase reinforcement, researchers have reported mixing a ductile material with the metallic glass matrix[15, 19]. Conner et al.[19] used tungsten and steel fibers as reinforcement; Jiao et al.[65] and Li et al.[93] reported a simultaneous increase in strength and ductility with the introduction of tungsten into Zr-based metallic glasses.

In general, introducing reinforcement in the form of particle, wire or fiber into metallic glass matrix enhances the toughness and ductility of bulk metallic glass composites. So far, most of the research efforts in this area have been focused on Zr-based metallic glasses as the metallic glasses matrix because of their excellent glass-forming ability which in turn renders manufacturing of BMG-based composites an easy process.

In this chapter, we will examine the mechanical behavior under uniaxial compression of a metallic glass composite material consisting of the amorphous phase of $Hf_{52.5}Ti_5Cu_{17.9}Ni_{14.6}Al_{10}$ (Hf105) reinforced with 72.5 vol% tungsten particles. The strain rates used in this work ($10^{-4}s^{-1}$ to $4 \times 10^3s^{-1}$) covers both the quasi-static and dynamic (high strain rate) loading conditions. The experimental results suggest an increase of total plastic strain under compression. Compared to the un-reinforced amorphous alloy, for which the strength decreases with strain rate in the dynamic region, the strength increases with strain rate for the metallic glass composite. The reasons behind this significant change in mechanical behavior by the introduction of reinforcements have been discussed.

Table 4: Physical and mechanical properties of tungsten reinforced Hf-BMG matrix composite.

| Material | Density(g/cm ³) | Young's modulus(GPa) | Hardness(GPa) | Melting temperature(K) |
|-------------|-----------------------------|----------------------|---------------|------------------------|
| Hf105-W72.5 | 17.85 | 333 | 6.2 | N/A |
| Hf105 | 11.1[75] | 128 | 7.8 | 1300[74] |
| W | 19.3 | 411 | 3.4 | 3695 |

5.2 Materials and experimental procedure

The BMG-based composite material used in this work was prepared by US Army Research Laboratory (Aberdeen Proving Ground, MD) using a hot isostatic pressing(HIPing) system for the consolidation of tungsten and the metallic glass powders. The Hf-based metallic glass powder was atomized at Ames Laboratory. A specially designed HIPing system was used which was equipped with an in-situ sensor to monitor the shrinkage of the HIPing can in order to prevent the formation of the HfW₂ inter-metallic phase. The tungsten and Hf-BMG powders were mixed together in the HIPing can, and the initial temperature was held at around 730K to allow rearrangement and partial consolidation of the powders. Then the temperature was increased to about 1300K with a pressure of 206MPa to allow the powder to achieve further consolidation. Afterwards the temperature was increased to the liquidus temperature of the metallic glass phase of $Hf_{52.5}Ti_5Cu_{17.9}Ni_{14.6}Al_{10}$ (1330K)[74, 75]. The powders were consolidated at this temperature until a change was observed in the sensor signal that indicates the completion of the consolidation process. Then the system is shut off to lower the temperature and pressure inside the HIP can. The basic properties of the composite and its components are listed in Table 4.

The as received composite material was electric discharge machined(EDM) to small specimens of cylinders with a diameter of 2.5 mm and a length of 2.5mm. The loading

surfaces were polished down to $0.5 \mu\text{m}$ before mechanical loading. The Vicker hardness value was measured using a microhardness tester. Scanning electron microscopy (SEM) was used for the morphology and fracture surface characterization. SEM was performed on a JEOL 6480 microscope operated at 15kV.

Quasi-static strain rate jump test was conducted using an MTS hydro-servo system. The initial imposed strain rate was $8 \times 10^{-4} \text{s}^{-1}$, and after the sample entered plastic deformation region, the strain rate was increased to $1.6 \times 10^{-3} \text{s}^{-1}$ for a further deformation of 2.5% strain. Then the strain rate was jumped to the final value $3.2 \times 10^{-3} \text{s}^{-1}$ until the prescribed strain was obtained. Dynamic compressive loading at strain rates of around $4 \times 10^3 \text{s}^{-1}$ was performed using a desktop Kolsky bar system. Compared to the conventional Kolsky bar system, the desktop bar can be used to test smaller samples and provide higher strain rate.

5.3 Experimental results

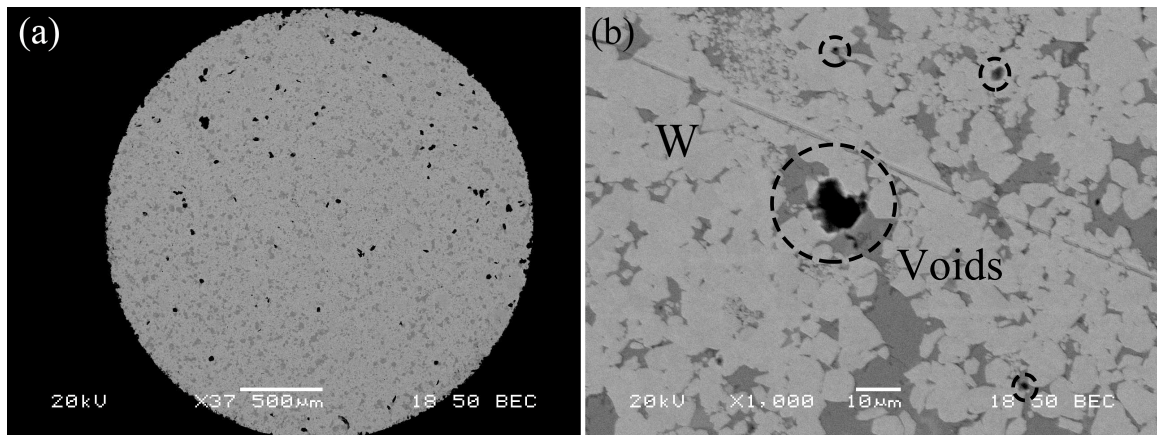


Figure 38: SEM characterization of the as received tungsten reinforced Hf-based metallic glass composite. (a) low magnification of the polished surface. (b) high magnification of the surface. The bright area is tungsten particles and the grey area is the Hf-BMG matrix, the black areas which are circled out in (b) are voids formed during the HIP process.

The morphology of the composite was characterized by SEM. Figure 38 shows the microstructure of the polished surface of the as received composite material. The bright areas denote the tungsten particles, while the grey areas are the metallic glass matrix. This micrograph suggested that the tungsten reinforcing particles are uniformly distributed in the amorphous matrix. Because of the large volume fraction (72.5 vol%) of the tungsten particles, it seems that the Hf-based metallic glass matrix is surrounded by the tungsten phase. Micro-voids are observed on the surface of the as received composite, which has been cycled out in Figure 38(b). Since the preform of the BMG-based composite has been produced through an initial HIP technique, the material may not be fully dense and voids may exist after the initial HIP. Additionally, the BMG may not fully amorphous. It is also possible that the difference between the coefficients of thermal expansion of W and Hf-BMGs may have caused the formation of the micro-voids during the cooling stage.

Figure 39 shows the representative true stress-strain curves of the metallic glass composite and the Hf-BMG under quasi-static compression. For comparison, the quasi-static compression result of pure W is also included [164]. The yield stress of the composite is comparable to the yield stress of pure W, but is lower than that of Hf105 metallic glass. It can be inferred that the W reinforcement plays a dominant role during the quasi-static loading. The stress-strain curve of the BMG-based composite also exhibit a significantly increase in the total compressive plastic strain compared to the stress-strain curve of the metallic glass. It should also be noted that the experiments were stopped at a prescribed strain, and no failure has been observed. The quasi-static stress-strain curve also includes the strain rate jump

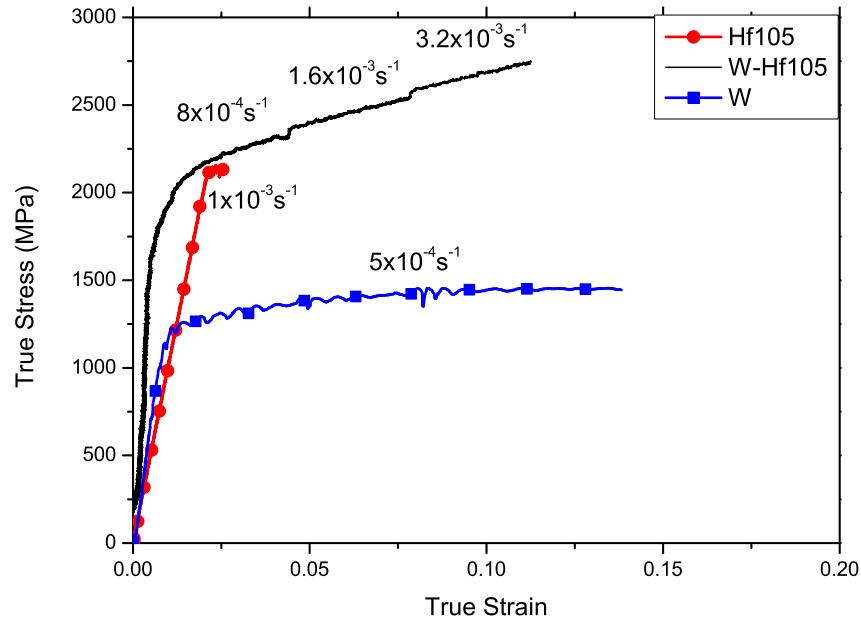


Figure 39: True strain-stress curves for metallic glass composite and the pure amorphous Hf105 metallic alloy under quasi-static compression.

information, and a value of strain rate sensitivity $m = 0.023$ was obtained. The strain rate sensitivity of the composite is very close to the value of the tungsten, which is about 0.025[162]. This m is also higher than the number reported by Jiao et al.[65] for W reinforcing Zr-BMG composite. We believe that this is a result of the high W volume fraction in the material studied in this work. Compared to other W reinforced metallic glass composite[93, 65], the quasi-static compression test in this work shows a strong strain hardening effect. The detail will be discussed in the following section.

Figure 40 shows the representative true stress-strain curve for the metallic glass composite under dynamic loading condition together with that of Hf105 metallic glass. For comparison, the dynamic behavior of pure tungsten is also included[164].

The stress-strain curve suggests that the BMG-based composite reaches the maxi-

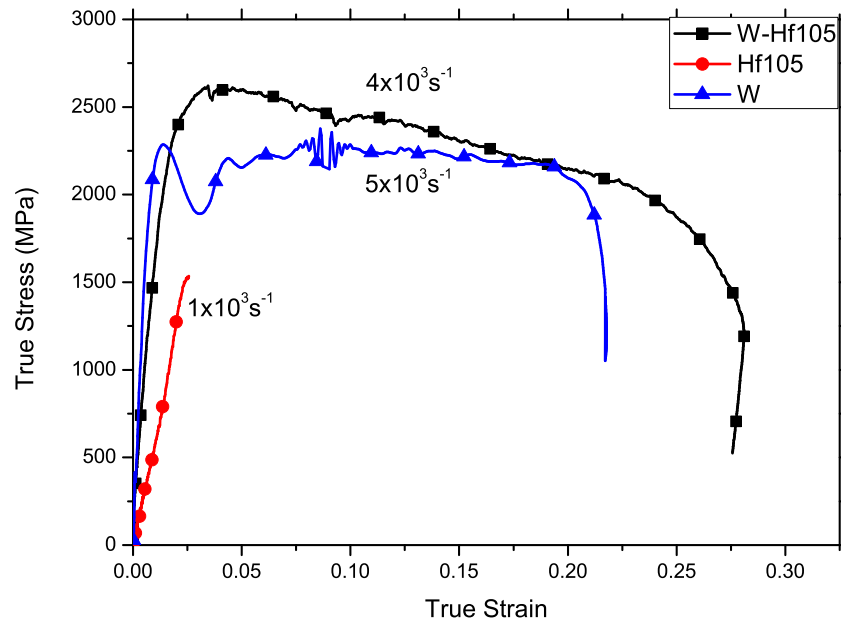


Figure 40: True strain-stress curves for metallic glass composite and the pure amorphous Hf105 metallic alloy under dynamic compression.

imum stress and then starts to show flow softening behavior, which is similar to the dynamic deformation behavior of ultrafine grained (UFG) W reported by Wei and co-workers[162, 164]. More than 20% plastic strain is observed from the dynamic compression experiments of the BMG-based composite.

Compared to the quasi-static results, the yield stress of the composite is greater under dynamic loading. This is in sharp contrast to the behavior of the un-reinforced bulk metallic glass which shows an opposite trend. This positive strain rate sensitivity of the W-reinforced BMG composite, which is also proved by the strain rate jump test, can be attributed to the high volume fraction of the W reinforcement. The similar behavior of W and W reinforced Hf-BMG composite suggests that the BMG based composite behavior is dominated by the W particles.

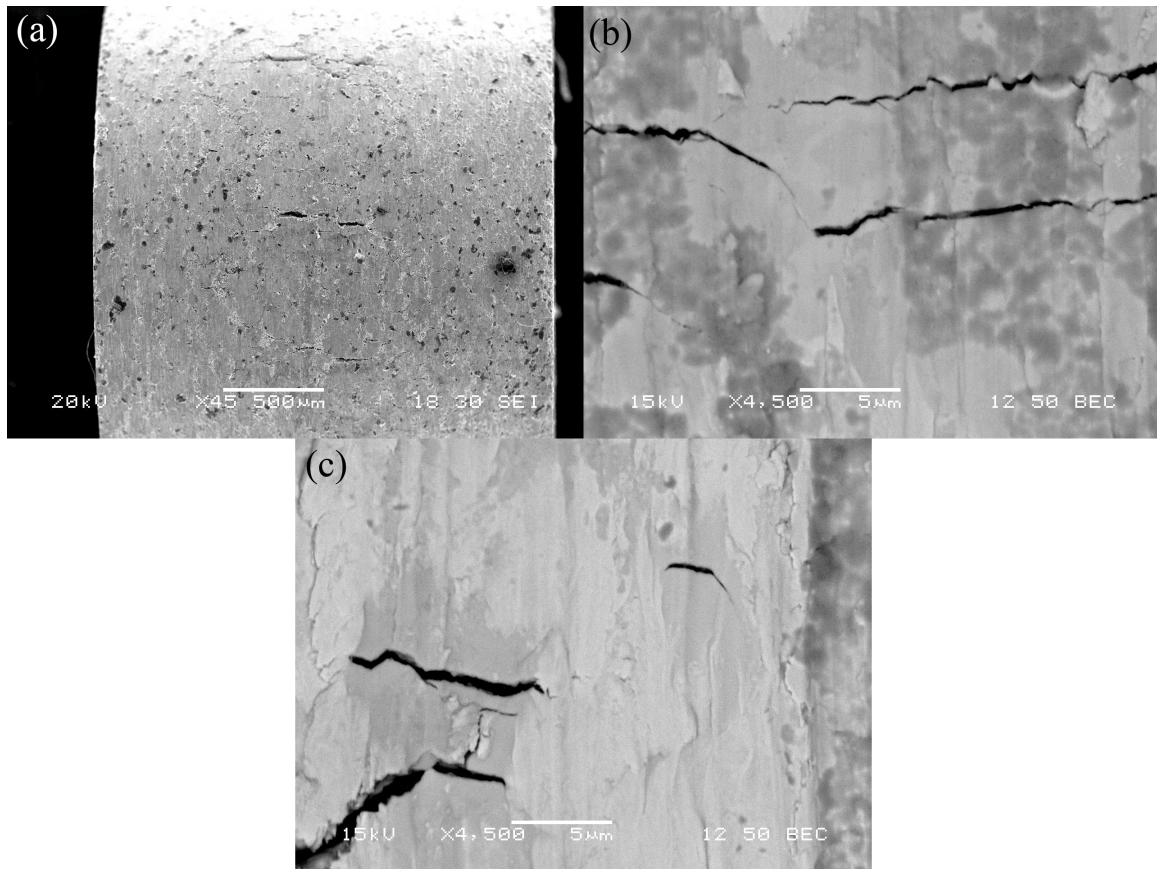


Figure 41: Post-mortem SEM images of the composite specimen under quasi-static loading. (a) is the overview of the tested sample, the loading axial is horizontal, several large cracks with numerous microcracks can be observed. (b) Cracks propagate through the phase boundaries with changing direction and (c) microcracks are mostly inside the glass.

Figure 41 displays the micrographs revealing the deformation mechanism of the W-reinforced BMG composite under quasi-static loading. The tested specimen did not fail at the prescribed strain. Several large cracks are observed on the side surface, and numerous microcracks can also be observed. Most of the cracks propagated along the loading axis. The cracks appear to have been initialized inside the glass phase, and the interface between the glass matrix and the W particles stopped the cracks or at least changed the propagation direction. No shear band on the sample surface was observed, which is different from the observation of other research work[93, 65, 167].

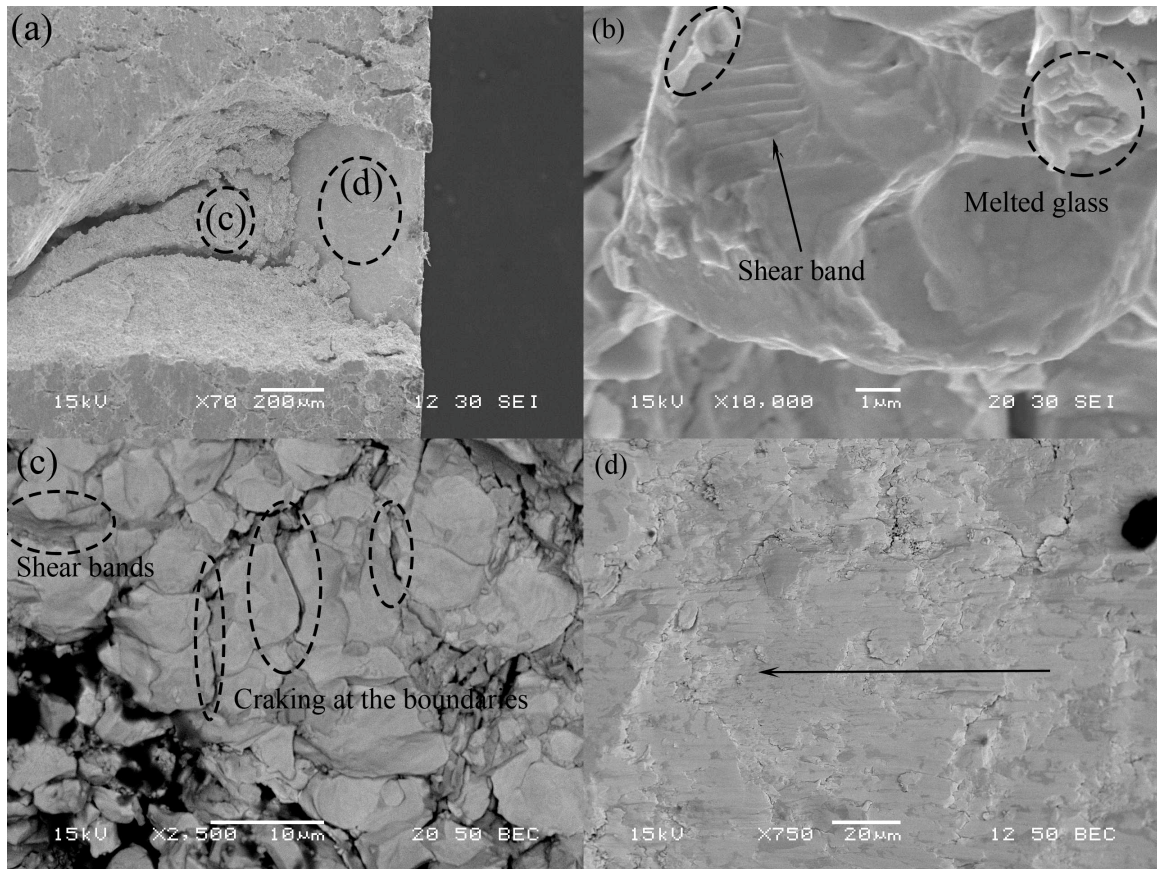


Figure 42: Post-mortem SEM images of the composite specimen under dynamic loading. (a) is the overview of the fracture surface, two different fracture surfaces were observed, (b) enlarge view of the fracture surface shows shear bands formed and melted glass. (c) magnification of the area (c) in Figure (a) reveals shear bands and the cracks and (d) high magnification view of area (d) in Figure (a), indicates the flow of metallic glass over the W particles and the flow direction is denoted by the arrow.

During the dynamic compression, all specimens failed into several fragments. Figure 42 shows the SEM micrograph of the fracture surface of the BMG composite. The deformation features shown here are similar to those under quasi-static compression, in that the inter-phase boundaries suppress the propagation of the cracks. However, shear band and local melting of the metallic glass phase are observed on the fracture surface, which indicates that more severe plastic deformation has occurred during dynamic loading. When the fracture surface is close to 45° , the surface is more smooth

compared to other fracture areas, indicating a large area of the flow of the melted glass over the W particles, as shown in Figure 42(d). The same flat shear surface was also reported by Choi-Yim et al.[14] for a tungsten reinforced Zr-based metallic glass composite. Another example of the fracture surface morphology is shown in Figure 42(d). Here, axial split fracture can be observed which might have been caused by the splitting of the W phase. The same shearing/splitting, smooth/rough fracture surface is also observed by Xue et al.[172] and Leng et al.[85].

5.4 Discussion

The sporadic voids observed on the surface of the as-received composite is most likely introduced during materials processing. The different coefficients of the thermal expansion of the bulk metallic glass matrix and the tungsten reinforcement introduce thermal strains during the cooling from the consolidation temperature. The thermal strain can be calculated by $\varepsilon_t = \Delta\alpha\Delta T$, where $\Delta\alpha$ is the thermal expansion coefficient difference between the W phase and the Hf-BMG, and ΔT is the temperature difference between the consolidation temperature and room temperature. The thermal expansion coefficient for the Hf-based metallic glass is found to be about $12 \times 10^{-6} K^{-1}$ [113], and the value for W is about $4.5 \times 10^{-6} K^{-1}$. The temperature change during the processing is about 1000K. According to the equation, the total strain caused by the thermal expansion mismatch is about 0.75%, which is quite significant and may induce micro-voids during the cooling stage during the HIPing process. Also the residual stress left at the interface of the W and metallic glass matrix typically lowers the tensile yield and ultimate strengths[3].

Another reason that may cause the micro-voids in the as received composite is the HIP run number. The run number of the HIP process determines whether the specimen is fully dense or not. Since the specimens tested in this work have only gone through the initial HIP run, and the high temperature was removed once the HfW2 inter-metallic phase was detected. The specimen may not be fully dense at the time when the high temperature and pressure are removed. More HIP runs maybe needed to produce BMG-based composites with higher density.

Unlike other metal matrix composites (MMC) (e.g. magnesium-based MMCs[142]), metallic glass composite contains the amorphous phase alloy which does not have dislocations, and therefore cannot undergo extensive plastic deformation upon mechanical loading. Nevertheless, the reinforcement W particles should have good ability to deform plastically. It is assumed that yielding begins when the stress level inside the specimen is larger than the yield stress of the W particles. This is also revealed by Figure 39, where the true stress-strain curve bends over when the stress level reaches the yield stress of the W. This indicates the initial yielding of the composite is indeed triggered by the yielding of the reinforcement phase.

The large compressive plastic strain of the composite was caused by the confinement of the crack propagation inside the metallic glass matrix. The large difference in elastic modulus between the metallic glass matrix and the tungsten reinforcement particles creates stress concentrations that may promote the shear band and crack initialization in the matrix, as shown in Figure 41(c). The Poisson's ratio difference between the matrix and the particle will refine the cracks and promote multiple micro-cracks to be initialized inside the matrix and as a consequence, increase the plastic strain of

the composite.

Strain hardening has been observed during the quasi-static compressive test of the composite experiment of the BMG-based composite. Experimental results reported by other researchers on the quasi-static compressive experiments of W reinforced metallic glass matrix composites all exhibit steady plastic flow after yielding[130, 20, 24, 18], which is different from our result. It should also be noted that numerous pre-existing pores can be found inside the specimen as shown in Figure 38. It has been widely reported that the porous alloys and MMCs exhibit strain hardening during the quasi-static and the dynamic compressive tests[22, 77]. The strain hardening effect of the tested composite is caused by the micro-voids inside the composite. Since compressive test is a highly constrained test, the density of the porous composite increases as the plastic strain increases. The overall strain hardening is a consequence of the progressive compacting of the voids during the compressive deformation of the specimen.

The yield stress of the BMG composite under dynamic compressive loading is significantly greater than that under quasi-static compressive loading. The increase of the yield stress with increasing strain rate can be attributed to the high volume fraction of the W particles. Both W and W-composite are well known to exhibit a positive strain rate sensitivity[162, 163, 173]. However, compared to quasi-static experimental results, a strain softening was observed during the dynamic loading of the BMG composite. The flow softening of the BMG composite material indicates that during the dynamic loading, the density increases caused by the compressive strain will not play the dominant role on the flow stress of the material, and other

deformation mechanism may cause the stress decrease during the dynamic loading. SEM observation of the fracture surface of the dynamically loaded specimen suggests that the specimen undergoes more severe plastic deformation during the dynamic loading, and multiple shear bands and melting of the glass phase can be seen on the fracture surface beside the propagation of the cracks. The shear band formation and the melting of the glass phase suggest that significant adiabatic temperature rise might have taken place during the short loading time. Like other bcc metals, the strength of tungsten decreases rapidly with increasing temperature[87], and the viscosity of the metallic glass also decreases significantly when the temperature increases to the super-cooled liquid temperature region. Therefore, during the dynamic loading, the thermal softening effect is stronger than the increased density effect, and this will produce a strain softening as shown on the true stress-strain curve.

5.5 Conclusions

In this chapter, we investigated the deformation and failure behavior of 72.5% vol% W particle reinforced $Hf_{52.5}Ti_5Cu_{17.9}Ni_{14.6}Al_{10}$ metallic glass matrix composite under both quasi-static and dynamic compressive loading. The results and discussion suggest that:

1. The addition of the W reinforcement can significantly increase the plastic deformation ability of the metallic glass. The large plastic strain is mainly attributed to the plastic deformation refinement between the W and the glass matrix.
2. Strain rate jump experiments reveal a positive strain rate sensitivity of the BMG composite with a value of 0.023, which is very close to the value of tungsten.

It suggests that the yielding of the composite can be mainly attributed to the high volume fraction of the tungsten reinforcement. A significant yield stress increase during the dynamic compressive loading is also observed for the composite which is similar to W and W-composite.

3. Pre-existing voids inside the specimen cause the strain hardening during the quasi-static test. However, under dynamic loading, adiabatic thermal effect plays a key role in the flow stress of the composite, which decreases the stress with increased strain.

4. No failure has been observed for the quasi-static specimen. Instead, only cracks can be seen on the sample surface, presumably propagating along the loading axis. Samples failed during the dynamic loading after 25% strain. The crack propagation and the shear of the glass matrix are the main reasons for the failure of the BMG-composite based on the SEM observation of the post-loading specimens.

CHAPTER 6: CONCLUSIONS AND FUTURE WORK

The mechanical behavior of $Zr_{55}Al_{10}Ni_5Cu_{30}$ and a few other BMGs was studied by MTS and Kolsky bar system at quasi-static and dynamic uniaxial compressive loading at room temperature. Quasi-static true stress-strain curves showed serrated plastic flow before failure, and the serrated flows was found to be associated with the formation of individual shear band during the compression. Stress induced local viscosity decrease was found during the serrated flow. Compressive experiments at different quasi-static strain rates have been performed to evaluate the strain rate sensitivity of the bulk metallic glass, and the strain rate sensitivity of the Zr-based bulk metallic glass is found to be positive. Based on this, the volume of the shear transformation zones has been calculated with the strain rate sensitivity value. However, at the dynamic (high) strain rates, the fracture stresses were lower than those in the quasi-static compressive experiments. Temperature increase in the specimen in the dynamic experiments was found to be the main reason for the strength drop at the high strain rates.

A synchronically assembled heating system was successfully attached onto the Kolsky bar system to perform the high temperature and high strain rate uniaxial compressive experiments of the Zr-based bulk metallic glass. A transition from inhomogeneous plastic deformation (i.e., shear banding process) to homogeneous plastic

deformation has been observed when the ambient temperature was close to the glass transition temperature of the specimen. The specimen deformed uniformly when the temperature was greater than 678K, and no failure was observed over even at 40% strains. However, no transition has been observed at dynamic strain rate even when the testing temperature was 718K. The free volume model was successfully applied to explain the deformation mechanism of the material. The deformation mechanism relates to the free volume concentration inside the specimen, which is controlled by the stress induced free volume creation competing with the free volume annihilation caused by the atomic diffusion process. The maximum stresses were found to decrease with increasing temperature.

Nanoindentation experiments with three different testing methods have been performed on the Zr-based metallic glass. Constant strain rate experiments produced a high strain rate sensitivity compared to the result from the strain rate jump experiments with nanoindentation. Large thermal drift effect has been found at the low strain rate during the nanoindentation experiments, which renders the strain rate sensitivity value to be greater than that from the strain rate jump tests. Hardness evolution was found and discussed.

Finally, tungsten particle reinforced $Hf_{52.5}Ti_5Cu_{17.9}Ni_{14.6}Al_{10}$ bulk metallic glass matrix composite is tested under both quasi-static and dynamic uniaxial compressive loading. The over 70 vol.% addition of the W particles enhanced the plastic deformation ability of the bulk metallic glass significantly. The quasi-static strength is equivalent to the strength of the matrix, however, strain hardening has been observed after elastic deformation which is caused by the porous structure. The dynamic

strength was improved significantly, and the yield strength is about 2.5 GPa, much higher than the strength of the metallic glass matrix (~ 2 GPa). The increased strength with increasing strain rate of the composite is very similar to the behavior of tungsten, which indicates that the high volume fraction of the W reinforcing particles dominated the deformation behavior of the composite. Strain softening was observed in the high strain rate experiments caused by the local temperature increase and softening of the matrix.

Although the coupled thermo-strain-rate experiments have been conducted on the bulk metallic glasses, and the free volume model has been applied to explain the deformation mechanism, evaluation of the thermal effect at different quasi-static strain rates to fully characterize the mechanical behavior of the Zr-based metallic glasses at elevated temperature is yet to be done. The shear banding process has been found to be due to the low viscosity caused by the imposed stress, but a more detailed shear band characterization with hardness evaluation, and the transmission electron microscopy observation needs to be performed to reveal the detailed microstructure variation inside the shear band. Also, TEM investigation of the indentation area of the specimen, especially for the low strain rate indents, need to be conducted to reveal the crystallization and free volume migration during the plastic deformation process. The effect of the crystallization behavior during the deformation might be predicted. For the metallic glass matrix composite, more experiments need to be performed on the effect of the volume fraction on the mechanical behavior of the composite. The material processing can be improved to reduce the voids inside the material to eliminate the effect of the voids.

REFERENCES

- [1] APOSTOL, M., VUORISTO, T., AND KUOKKALA, V.-T. High temperature high strain rate testing with a compressive SHPB. *Journal de Physique IV (Proceedings) 110* (2003), 459–464.
- [2] ARGON, A. S. PLASTIC-DEFORMATION IN METALLIC GLASSES. *Acta Metallurgica 27*, 1 (1979), 47–58.
- [3] ARSENAULT, R., AND TAYA, M. Thermal residual stress in metal matrix composite. *Acta Metallurgica 35*, 3 (1987), 651–659.
- [4] ASHBY, M., AND GREER, A. Metallic glasses as structural materials. *Scripta Materialia 54*, 3 (2006), 321 – 326.
- [5] BEI, H., LU, Z., AND GEORGE, E. Theoretical strength and the onset of plasticity in bulk metallic glasses investigated by nanoindentation with a spherical indenter. *Physical review letters 93*, 12 (2004), 125504.
- [6] BEI, H., XIE, S., AND GEORGE, E. P. Softening caused by profuse shear banding in a bulk metallic glass. *Physical review letters 96*, 10 (2006), 105503.
- [7] BRUCK, H., ROSAKIS, A., AND JOHNSON, W. The dynamic compressive behavior of beryllium bearing bulk metallic glasses. *JOURNAL OF MATERIALS RESEARCH 11*, 2 (FEB 1996), 503–511.
- [8] CALIN, M., ECKERT, J., AND SCHULTZ, L. Improved mechanical behavior of *Cu–Ti*-based bulk metallic glass by in situ formation of nanoscale precipitates. *Scripta Materialia 48*, 6 (2003), 653–658.
- [9] CHEN, H. Thermodynamic considerations on the formation and stability of metallic glasses. *Acta Metallurgica 22*, 12 (1974), 1505 – 1511.
- [10] CHEN, H. S. Glassy metals. *Reports on Progress in Physics 43*, 4 (1980), 353.
- [11] CHEN, M. Mechanical Behavior of Metallic Glasses: Microscopic Understanding of Strength and Ductility. *Annual Review of Materials Research 38*, 1 (2008), 445–469.
- [12] CHEN, W., AND SONG, B. *Split Hopkinson (Kolsky) Bar*. Springer, 2011.
- [13] CHENG, Y. Q., HAN, Z., LI, Y., AND MA, E. Cold versus hot shear banding in bulk metallic glass. *Physical Review B 80*, 13 (10 2009), 134115–.
- [14] CHOI-YIM, H., CONNER, R. D., SZUECS, F., AND JOHNSON, W. L. Quasistatic and dynamic deformation of tungsten reinforced $Zr_{57}Nb_5Al_{10}Cu_{15.4}Ni_{12.6}$ bulk metallic glass matrix composites. *Scripta materialia 45*, 9 (2001), 1039–1046.

- [15] CHOI-YIM, H., AND JOHNSON, W. Bulk metallic glass matrix composites. *Applied physics letters* 71, 26 (1997), 3808–3810.
- [16] CLEMENTI, E., AND RAIMONDI, D. L. Atomic Screening Constants from SCF Functions. *The Journal of Chemical Physics* 38, 11 (1963), 2686–2689.
- [17] COHEN, M. H., AND TURNBULL, D. Molecular transport in liquids and glasses. *The Journal of Chemical Physics* 31 (1959), 1164.
- [18] CONNER, R., CHOI-YIM, H., AND JOHNSON, W. Mechanical properties of $Zr_{57}Nb_5Al_{10}Cu_{15.4}Ni_{12.6}$ metallic glass matrix particulate composites. *J. Mater. Res* 14, 8 (1999), 3293.
- [19] CONNER, R., DANDLIKER, R., AND JOHNSON, W. Mechanical properties of tungsten and steel fiber reinforced $Zr_{41.25}Ti_{13.75}Cu_{12.5}Ni_{10}Be_{22.5}$ metallic glass matrix composites. *Acta Materialia* 46, 17 (1998), 6089–6102.
- [20] CONNER, R., DANDLIKER, R., SCRUGGS, V., AND JOHNSON, W. Dynamic deformation behavior of tungsten-fiber/metallic-glass matrix composites. *International Journal of Impact Engineering* 24, 5 (2000), 435–444.
- [21] CONRAD, H. *The cryogenic properties of metals*, v ed. John Wiley and Sons, New York., 1964.
- [22] DA SILVA, M., AND RAMESH, K. The rate-dependent deformation and localization of fully dense and porous $Ti - 6Al - 4V$. *Materials Science and Engineering: A* 232, 1 (1997), 11–22.
- [23] DALLA TORRE, F. H., DUBACH, A., SCHÄLLIBAUM, J., AND LÖFFLER, J. F. Shear striations and deformation kinetics in highly deformed Zr -based bulk metallic glasses. *Acta Materialia* 56, 17 (2008), 4635–4646.
- [24] DANDLIKER, R., CONNER, R., AND JOHNSON, W. Melt infiltration casting of bulk metallic-glass matrix composites. *Journal of materials research* 13, 10 (1998), 2896–2901.
- [25] DAS, J., TANG, M. B., KIM, K. B., THEISSMANN, R., BAIER, F., WANG, W. H., AND ECKERT, J. Work-hardenable ductile bulk metallic glass. *Physical review letters* 94, 20 (2005), 205501.
- [26] DEMETRIOU, M. D., LAUNEY, MAXIMILIEN E. AND GARRETT, G., SCHRAMM, J. P., HOFMANN, D. C., JOHNSON, W. L., AND RITCHIE, R. O. A damage-tolerant glass. *Nat Mater* 10 (2011), 123 – 128.
- [27] DENG, C., AND SCHUH, C. A. Atomistic mechanisms of cyclic hardening in metallic glass. *Applied Physics Letters* 100, 25 (2012), 251909–251909.
- [28] DONOVAN, P. A yield criterion for $Pd_{40}Ni_{40}P_{20}$ metallic glass. *Acta Metallurgica* 37, 2 (1989), 445–456.

- [29] DROZDZ, D., KULIK, T., AND FECHT, H. Nanoindentation studies of Zr-based bulk metallic glasses. *Journal of alloys and compounds* 441, 1 (2007), 62–65.
- [30] ELMUSTAFA, A., KOSE, S., AND STONE, D. The strain-rate sensitivity of the hardness in indentation creep. *Journal of materials research* 22, 04 (2007), 926–936.
- [31] ESHELBY, J., AND PRATT, P. Note on the heating effect of moving dislocations. *Acta Metallurgica* 4, 5 (1956), 560–562.
- [32] FALK, M., AND LANGER, J. Dynamics of viscoplastic deformation in amorphous solids. *Physical Review E* 57, 6 (1998), 7192.
- [33] FAN, C., OTT, R., AND HUFNAGEL, T. Metallic glass matrix composite with precipitated ductile reinforcement. *Applied physics letters* 81, 6 (2002), 1020–1022.
- [34] FISCHER-CRIPPS, A. A simple phenomenological approach to nanoindentation creep. *Materials Science and Engineering: A* 385, 1 (2004), 74–82.
- [35] FLORES, K. M., AND DAUSKARDT, R. Mean stress effects on flow localization and failure in a bulk metallic glass. *Acta materialia* 49, 13 (2001), 2527–2537.
- [36] FOLLANSBEE, P. *ASM Metals Handbook*, vol. 8. ASM International, 1985.
- [37] GOLOVIN, Y. I., IVOLGIN, V., KHONIK, V., KITAGAWA, K., AND TYURIN, A. Serrated plastic flow during nanoindentation of a bulk metallic glass. *Scripta materialia* 45, 8 (2001), 947–952.
- [38] GREER, A., CASTELLERO, A., MADGE, S., WALKER, I., AND WILDE, J. Nanoindentation studies of shear banding in fully amorphous and partially devitrified metallic alloys. *Materials Science and Engineering: A* 375 (2004), 1182–1185.
- [39] GREER, A. L. Metallic glasses. *Science* 267, 5206 (1995), 1947–1953.
- [40] GU, X., MCDERMOTT, A., POON, S. J., AND SHIFLET, G. J. Critical Poissons ratio for plasticity in $Fe - Mo - C - B - Ln$ bulk amorphous steel. *Applied physics letters* 88, 21 (2006), 211905–211905.
- [41] GUO, H., YAN, P., WANG, Y., TAN, J., ZHANG, Z., SUI, M., AND MA, E. Tensile ductility and necking of metallic glass. *Nature materials* 6, 10 (2007), 735–739.
- [42] HAYS, C., KIM, C., AND JOHNSON, W. Microstructure controlled shear band pattern formation and enhanced plasticity of bulk metallic glasses containing in situ formed ductile phase dendrite dispersions. *Physical Review Letters* 84, 13 (2000), 2901–2904.

- [43] HIRATA, A., GUAN, P., FUJITA, T., HIROTSU, Y., INOUE, A., YAVARI, A. R., SAKURAI, T., AND CHEN, M. Direct observation of local atomic order in a metallic glass. *Nature materials* 10, 1 (2010), 28–33.
- [44] HOFMANN, D. C., SUH, J.-Y., WIEST, A., DUAN, G., LIND, M.-L., DEMETRIOU, M. D., AND JOHNSON, W. L. Designing metallic glass matrix composites with high toughness and tensile ductility. *Nature* 451, 7182 (2008), 1085–1089.
- [45] HOJO, M., AND NUMAKURA, H. Dynamic glass transition in $Zr-Al-Ni-Cu$ bulk metallic glass. *Materials Science and Engineering: A* 442, 1 (2006), 268–272.
- [46] HONEYCOMBE, R. W. K. *The plastic deformation of metals*. Edward Arnold., 1975.
- [47] HUANG, R., SUO, Z., PREVOST, J., AND NIX, W. Inhomogeneous deformation in metallic glasses. *Journal of the Mechanics and Physics of Solids* 50, 5 (2002), 1011–1027.
- [48] HUANG, Y., CHIU, Y. L., SHEN, J., CHEN, J. J., AND SUN, J. Nanoindentation study of Ti -based metallic glasses. *Journal of Alloys and Compounds* 479, 1 (2009), 121–128.
- [49] HUANG, Y., SHEN, J., AND SUN, J. Bulk metallic glasses: Smaller is softer. *Applied Physics Letters* 90, 8 (2007), 081919–081919.
- [50] HUFNAGEL, T., JIAO, T., LI, Y., XING, L., AND RAMESH, K. Deformation and failure of $Zr_{57}Ti_5Cu_{20}Ni_8Al_{10}$ bulk metallic glass under quasi-static and dynamic compression. *JOURNAL OF MATERIALS RESEARCH* 17, 6 (JUN 2002), 1441–1445.
- [51] ICHITSUBO, T., KAI, S., OGI, H., HIRAO, M., AND TANAKA, K. Elastic and anelastic behavior of $Zr_{55}Al_{10}Ni_5Cu_{30}$ bulk metallic glass around the glass transition temperature under ultrasonic excitation. *Scripta materialia* 49, 4 (2003), 267–272.
- [52] INOUE, A. Stabilization of metallic supercooled liquid and bulk amorphous alloys. *Acta Materialia* 48, 1 (2000), 279 – 306.
- [53] INOUE, A., NISHIYAMA, N., AND KIMURA, H. Preparation and thermal stability of bulk amorphous $Pd_{40}Cu_{30}Ni_{10}P_{20}$ alloy cylinder of 72 mm in diameter. *Materials Transactions-JIM* 38 (1997), 179–183.
- [54] INOUE, A., SHEN, B., KOSHIBA, H., KATO, H., AND YAVARI, A. Ultra-high strength above 5000MPa and soft magnetic properties of $Co - Fe - Ta - B$ bulk glassy alloys. *Acta Materialia* 52, 6 (2004), 1631–1637.

- [55] INOUE, A., SHINOHARAL, Y., YOKOYAMA, Y., AND MASUMOTO, T. Solidification Analyses of Bulky $Zr_{60}Al_{10}Ni_{10}Cu_{15}Pd_5$ Glass Produced by Casting into Wedge-Shape Copper Mold. *MATERIALS TRANSACTIONS JIM* 36 (1995), 1276–1281.
- [56] INOUE, A., SOBU, S., LOUZGUINE, D. V., KIMURA, H., AND SASAMORI, K. Ultrahigh strength Al-based amorphous alloys containing *Sc*. *Journal of materials research* 19, 05 (2004), 1539–1543.
- [57] INOUE, A., AND TAKEUCHI, A. High strength bulk amorphous alloys. *Mater. Trans. JIM* 43, 8 (2002), 1892–1906.
- [58] INOUE, A., AND TAKEUCHI, A. Recent development and application products of bulk glassy alloys. *Acta Materialia* 59, 6 (2011), 2243–2267.
- [59] INOUE, A., AND ZHANG, T. Fabrication of bulky Zr-based glassy alloys by suction casting into copper mold. *Materials transactions-JIM* 36 (1995), 1184–1187.
- [60] INOUE, A., ZHANG, T., AND MASUMOTO, T. Production of amorphous cylinder and sheet of $La_{55}Al_{25}Ni_{20}$ alloy by a metallic mold casting method. *Mater. Trans. JIM* 31, 5 (1990), 425–428.
- [61] INOUE, A., ZHANG, T., AND MASUMOTO, T. *Zr–Al–Ni* Amorphous Alloys With High Glass Transition Temperature and Significant Supercooled Liquid Region. *Mater. Trans., JIM* 31, 3 (1990), 177–183.
- [62] INOUE, A., ZHANG, W., ZHANG, T., AND KUROSAKA, K. High-strength *Cu*-based bulk glassy alloys in *Cu–Zr–Ti* and *Cu–Hf–Ti* ternary systems. *Acta materialia* 49, 14 (2001), 2645–2652.
- [63] JANG, D., AND GREER, J. R. Transition from a strong-yet-brittle to a stronger-and-ductile state by size reduction of metallic glasses. *Nature materials* 9, 3 (2010), 215–219.
- [64] JIANG, W. H., PINKERTON, F. E., AND ATZMON, M. Effect of strain rate on the formation of nanocrystallites in an Al-based amorphous alloy during nanoindentation. *Journal of Applied Physics* 93, 11 (2003), 9287–9290.
- [65] JIAO, T., KECSKES, L., HUFNAGEL, T., AND RAMESH, K. Deformation and failure of $Zr_{57}Nb_5Al_{10}Cu_{15.4}Ni_{12.6}/W$ particle composites under quasi-static and dynamic compression. *METALLURGICAL AND MATERIALS TRANSACTIONS A-PHYSICAL METALLURGY AND MATERIALS SCIENCE* 35A, 11 (NOV 2004), 3439–3444.
- [66] JOHNSON, W. L. Bulk Glass-Forming Metallic Alloys: Science and Technology. *MRS Bulletin* 24 (2009), 42 – 56.

- [67] JOHNSON, W. L., LU, J., AND DEMETRIOU, M. D. Deformation and flow in bulk metallic glasses and deeply undercooled glass forming liquids a self consistent dynamic free volume model. *Intermetallics* 10, 11 (2002), 1039–1046.
- [68] JOHNSON, W. L., AND SAMWER, K. A Universal Criterion for Plastic Yielding of Metallic Glasses with a $(T/T_g)^{2/3}$ Temperature Dependence. *Phys. Rev. Lett.* 95 (Nov 2005), 195501.
- [69] KATO, H., HIRANO, T., MATSUO, A., KAWAMURA, Y., AND INOUE, A. High strength and good ductility of $Zr_{55}Al_{10}Ni_5Cu_{30}$ bulk glass containing ZRC particles. *Scripta materialia* 43, 6 (2000), 503–507.
- [70] KATO, H., KAWAMURA, Y., CHEN, H.-S., AND INOUE, A. A fictive stress model calculation of nonlinear viscoelastic behaviors in a Zr-based glassy alloy: Stress growth and relaxation. *Japanese Journal of Applied Physics* 39 (2000), 5184.
- [71] KATO, H., KAWAMURA, Y., INOUE, A., AND CHEN, H. Newtonian to non-Newtonian master flow curves of a bulk glass alloy $Pd_{40}Ni_{10}Cu_{30}P_{20}$. *Applied physics letters* 73, 25 (1998), 3665–3667.
- [72] KAWAMURA, Y., NAKAMURA, T., KATO, H., MANO, H., AND INOUE, A. Newtonian and non-Newtonian viscosity of supercooled liquid in metallic glasses. *Materials Science and Engineering: A* 304 (2001), 674–678.
- [73] KAWAMURA, Y., SHIBATA, T., INOUE, A., AND MASUMOTO, T. Deformation behavior of $Zr_{65}Al_{10}Ni_{10}Cu_{15}$ glassy alloy with wide supercooled liquid region. *Applied physics letters* 69, 9 (1996), 1208–1210.
- [74] KECSKES, L. J., AND SZEWCZYK, S. T. Infiltration Processing of Tungsten-Reinforced Bulk-Amorphous Metal Matrix Composites.
- [75] KECSKES, L. J., WOODMAN, R. H., AND TREVINO, S. F. Dynamic Devitrification of Bulk Metallic Glasses (BMGs) and Composites of BMG With Tungsten. Tech. rep., DTIC Document, 2005.
- [76] KIM, J.-J., CHOI, Y., SURESH, S., AND ARGON, A. Nanocrystallization during nanoindentation of a bulk amorphous metal alloy at room temperature. *Science* 295, 5555 (2002), 654–657.
- [77] KIM, T.-W. Determination of densification behavior of Al—SiC metal matrix composites during consolidation processes. *Materials Science and Engineering: A* 483 (2008), 648–651.
- [78] KIMURA, H., AND MASUMOTO, T. A model of the mechanics of serrated flow in an amorphous alloy. *Acta Metallurgica* 31, 2 (1983), 231 – 240.
- [79] KLEMENT, W., WILLENS, R. H., AND DUWEZ, P. Non-crystalline Structure in Solidified Gold-Silicon Alloys. *Nature* 187 (Sept. 1960), 869–870.

- [80] KOCKS, U., ARGON, A., AND ASHBY, F. *Thermodynamics and Kinetics of Slip*. Argonne National Laboratory, 1973.
- [81] KUMAR, G., DESAI, A., AND SCHROERS, J. Bulk Metallic Glass: The Smaller the Better. *Advanced Materials* 23, 4 (2011), 461–476.
- [82] LATELLA, B. A., AND HUMPHRIES, S. R. Youngs modulus of a 2.25 Cr–1Mo steel at elevated temperature. *Scripta materialia* 51, 7 (2004), 635–639.
- [83] LEE, C., HUANG, J., AND NIEH, T. Sample size effect and microcompression of $Mg_{65}Cu_{25}Gd_{10}$ metallic glass. *Applied Physics Letters* 91, 16 (2007), 161913–161913.
- [84] LEE, J.-C., KIM, Y.-C., AHN, J.-P., KIM, H.-S., LEE, S.-H., AND LEE, B.-J. Deformation-induced nanocrystallization and its influence on work hardening in a bulk amorphous matrix composite. *Acta materialia* 52, 6 (2004), 1525–1533.
- [85] LENG, Y., AND COURTNEY, T. Fracture behavior of laminated metal-metallic glass composites. *Metallurgical Transactions A* 21, 8 (1990), 2159–2168.
- [86] LENNON, A., AND RAMESH, K. A technique for measuring the dynamic behavior of materials at high temperatures. *International Journal of Plasticity* 14, 12 (1998), 1279–1292.
- [87] LENNON, A., AND RAMESH, K. The thermoviscoplastic response of polycrystalline tungsten in compression. *Materials Science and Engineering: A* 276, 1 (2000), 9–21.
- [88] LEVITIN, V. *Atom Vibrations in Solids: Amplitudes and Frequencies*. Cambridge Scientific Publishers, 2004.
- [89] LEWANDOWSKI, J., WANG, W., AND GREER, A. Intrinsic plasticity or brittleness of metallic glasses. *Philosophical Magazine Letters* 85, 2 (2005), 77–87.
- [90] LEWANDOWSKI, J. J., AND GREER, A. L. Temperature rise at shear bands in metallic glasses. *Nature Materials* 5, 1 (2006), 15–18.
- [91] LEWANDOWSKI, J. J., AND LOWHAPHANDU, P. Effects of hydrostatic pressure on the flow and fracture of a bulk amorphous metal. *Philosophical magazine A* 82, 17-18 (2002), 3427–3441.
- [92] LI, H., SUBHASH, G., GAO, X.-L., KECSKES, L. J., AND DOWDING, R. J. Negative strain rate sensitivity and compositional dependence of fracture strength in Zr/Hf based bulk metallic glasses. *Scripta materialia* 49, 11 (2003), 1087–1092.
- [93] LI, H., SUBHASH, G., KECSKES, L. J., AND DOWDING, R. J. Mechanical behavior of tungsten preform reinforced bulk metallic glass composites. *Materials Science and Engineering: A* 403, 1 (2005), 134–143.

- [94] LI, N., CHEN, Q., AND LIU, L. Size dependent plasticity of a *Zr*-based bulk metallic glass during room temperature compression. *Journal of Alloys and Compounds* 493, 1 (2010), 142–147.
- [95] LI, Y., GUO, Y., HU, H., AND WEI, Q. A critical assessment of high-temperature dynamic mechanical testing of metals. *International Journal of Impact Engineering* 36, 2 (2009), 177–184.
- [96] LIU, C., HEATHERLY, L., HORTON, J., EASTON, D., CARMICHAEL, C., WRIGHT, J., SCHNEIBEL, J., YOO, M., CHEN, C., AND INOUE, A. Test environments and mechanical properties of *Zr*-base bulk amorphous alloys. *Metallurgical and Materials Transactions A* 29, 7 (1998), 1811–1820.
- [97] LIU, L., AND CHAN, K. Plastic deformation of *Zr*-based bulk metallic glasses under nanoindentation. *Materials letters* 59, 24-25 (2005), 3090–3094.
- [98] LIU, L., DAI, L., BAI, Y., WEI, B., AND YU, G. Strain rate-dependent compressive deformation behavior of *Nd*-based bulk metallic glass. *Intermetallics* 13, 8 (2005), 827–832.
- [99] LIU, M., HUANG, J., CHEN, K., LIN, J., LI, W., GAO, Y., AND NIEH, T. Is the compression of tapered micro-and nanopillar samples a legitimate technique for the identification of deformation mode change in metallic glasses? *Scripta Materialia* 66, 10 (2012), 817–820.
- [100] LIU, W., AND LIU, K. Mechanical behavior of a *Zr*-based metallic glass at elevated temperature under high strain rate. *Journal of Applied Physics* 108, 3 (2010), 033511–033511.
- [101] LIU, W. D., AND LIU, K. X. Notable internal thermal effect on the yielding of metallic glasses. *Applied Physics Letters* 100, 14 (2012), 141904.
- [102] LIU, W.-D., LIU, K.-X., XIA, X.-X., AND WANG, W.-H. The failure stress of bulk metallic glasses under very high strain rate. *JOURNAL OF MATERIALS RESEARCH* 25, 7 (JUL 2010), 1230–1234.
- [103] LIU, Y. H., WANG, G., WANG, R. J., PAN, M. X., WANG, W. H., ET AL. Super plastic bulk metallic glasses at room temperature. *science* 315, 5817 (2007), 1385–1388.
- [104] LOWHAPHANDU, P., MONTGOMERY, S., AND LEWANDOWSKI, J. Effects of superimposed hydrostatic pressure on flow and fracture of a *Zr – Ti – Ni – Cu – Be* bulk amorphous alloy. *Scripta materialia* 41, 1 (1999).
- [105] LU, J., RAVICHANDRAN, G., AND JOHNSON, W. Deformation behavior of the $Zr_{41.2}Ti_{13.8}Cu_{12.5}Ni_{10}Be_{22.5}$ bulk metallic glass over a wide range of strain-rates and temperatures. *Acta Materialia* 51, 12 (2003), 3429 – 3443.

- [106] LU, Z., AND LIU, C. A new approach to understanding and measuring glass formation in bulk amorphous materials. *Intermetallics* 12, 10 (2004), 1035–1043.
- [107] LU, Z., LIU, C., THOMPSON, J., AND PORTER, W. Structural amorphous steels. *Physical Review Letters* 92, 24 (2004), 245503.
- [108] LUCAS, B., AND OLIVER, W. Indentation power-law creep of high-purity indium. *Metallurgical and materials Transactions A* 30, 3 (1999), 601–610.
- [109] MA, H., XU, J., AND MA, E. Mg-based bulk metallic glass composites with plasticity and high strength. *Applied physics letters* 83, 14 (2003), 2793–2795.
- [110] MA, W., KOU, H., LI, J., CHANG, H., AND ZHOU, L. Effect of strain rate on compressive behavior of Ti-based bulk metallic glass at room temperature. *JOURNAL OF ALLOYS AND COMPOUNDS* 472, 1-2 (MAR 20 2009), 214–218.
- [111] MAIER, V., DURST, K., MUELLER, J., BACKES, B., HÖPPEL, H. W., AND GÖKEN, M. Nanoindentation strain-rate jump tests for determining the local strain-rate sensitivity in nanocrystalline Ni and ultrafine-grained Al. *Journal of Materials Research* 26, 11 (2011), 1421–1430.
- [112] MASUMOTO, T., AND MADDIN, R. The mechanical properties of palladium 20 at/o silicon alloy quenched from the liquid state. *Acta Metallurgica* 19, 7 (1971), 725 – 741.
- [113] MATTERN, N., KUHN, U., HERMANN, H., ROTH, S., VINZELBERG, H., AND ECKERT, J. Thermal behavior and glass transition of Zr-based bulk metallic glasses. *MATERIALS SCIENCE AND ENGINEERING A-STRUCTURAL MATERIALS PROPERTIES MICROSTRUCTURE AND PROCESSING* 375, SI (JUL 15 2004), 351–354.
- [114] MAYR, S. G. Activation Energy of Shear Transformation Zones: A Key for Understanding Rheology of Glasses and Liquids. *Phys. Rev. Lett.* 97 (Nov 2006), 195501.
- [115] MCELHANEY, K., VLASSAK, J., AND NIX, W. Determination of indenter tip geometry and indentation contact area for depth-sensing indentation experiments. *Journal of Materials Research* 13, 5 (1998), 1300–1306.
- [116] MIRACLE, D. B. A structural model for metallic glasses. *Nature materials* 3, 10 (2004), 697–702.
- [117] MUKAI, T., NIEH, T., KAWAMURA, Y., INOUE, A., AND HIGASHI, K. Dynamic response of a Pd₄₀Ni₄₀P₂₀ bulk metallic glass in tension. *Scripta materialia* 46, 1 (2002), 43–47.

- [118] MUKAI, T., NIEH, T., KAWAMURA, Y., INOUE, A., AND HIGASHI, K. Effect of strain rate on compressive behavior of a $Pd_{40}Ni_{40}P_{20}$ bulk metallic glass. *Intermetallics* 10, 11 (2002), 1071–1077.
- [119] MUKHOPADHYAY, N., BELGER, A., PAUFLER, P., AND KIM, D. Nanoindentation studies on $Cu - Ti - Zr - Ni - Si - Sn$ bulk metallic glasses. *Materials Science and Engineering: A* 449 (2007), 954–957.
- [120] NEMAT-NASSER, S. *High strain rate testing: ASM Handbook*. ASM International, 2007.
- [121] NEMAT-NASSER, S., AND ISAACS, J. Direct measurement of isothermal flow stress of metals at elevated temperatures and high strain rates with application to Ta and TaW alloys. *Acta Materialia* 45, 3 (1997), 907–919.
- [122] NEUHÄUSER, H. Rate of shear band formation in metallic glasses. *Scripta Metallurgica* 12 (1978), 471–474.
- [123] NIEH, T., WADSWORTH, J., LIU, C., OHKUBO, T., AND HIROTSU, Y. Plasticity and structural instability in a bulk metallic glass deformed in the supercooled liquid region. *Acta materialia* 49, 15 (2001), 2887–2896.
- [124] NISHIYAMA, N., AND INOUE, A. Stability and nucleation behavior of glass-forming $Pd - Cu - Ni - P$ alloy with a critical cooling rate of $0.067K/s$. *Intermetallics* 10, 11 (2002), 1141–1147.
- [125] OLIVER, W. C., AND PHARR, G. M. Improved technique for determining hardness and elastic modulus using load and displacement sensing indentation experiments. *Journal of materials research* 7, 6 (1992), 1564–1583.
- [126] OLIVER, W. C., AND PHARR, G. M. Measurement of hardness and elastic modulus by instrumented indentation: Advances in understanding and refinements to methodology. *Journal of materials research* 19, 01 (2004), 3–20.
- [127] PACKARD, C., WITMER, L., AND SCHUH, C. Hardening of a metallic glass during cyclic loading in the elastic range. *Applied Physics Letters* 92, 17 (2008), 171911–171911.
- [128] PAN, D., INOUE, A., SAKURAI, T., AND CHEN, M. W. Experimental characterization of shear transformation zones for plastic flow of bulk metallic glasses. *Proceedings of the National Academy of Sciences of the United States of America* 105, 39 (2008), 14769–14772.
- [129] PENG, H., LI, M., AND WANG, W. Stress-versus temperature-induced structural evolution in metallic glasses. *Applied Physics Letters* 102 (2013), 131908.
- [130] QIU, K., WANG, A., ZHANG, H., DING, B., AND HU, Z. Mechanical properties of tungsten fiber reinforced $ZrAlNiCuSi$ metallic glass matrix composite. *Intermetallics* 10, 11 (2002), 1283–1288.

- [131] SCHROERS, J., AND JOHNSON, W. L. Ductile bulk metallic glass. *Physical Review Letters* 93, 25 (2004), 255506.
- [132] SCHUH, C., AND NIEH, T. A nanoindentation study of serrated flow in bulk metallic glasses. *Acta Materialia* 51, 1 (2003), 87–99.
- [133] SCHUH, C., AND NIEH, T. A survey of instrumented indentation studies on metallic glasses. *Journal of materials research* 19, 1 (2004), 46–57.
- [134] SCHUH, C., NIEH, T., AND KAWAMURA, Y. Rate dependence of serrated flow during nanoindentation of a bulk metallic glass. *Journal of materials research* 17, 7 (2002), 1651–1654.
- [135] SCHUH, C. A., HUFNAGEL, T. C., AND RAMAMURTY, U. Mechanical behavior of amorphous alloys. *Acta Materialia* 55, 12 (2007), 4067 – 4109.
- [136] SCHUH, C. A., AND LUND, A. C. Atomistic basis for the plastic yield criterion of metallic glass. *Nature materials* 2, 7 (2003), 449–452.
- [137] SCHUH, C. A., AND LUND, A. C. Application of nucleation theory to the rate dependence of incipient plasticity during nanoindentation. *Journal of materials research* 19, 07 (2004), 2152–2158.
- [138] SCHUH, C. A., LUND, A. C., AND NIEH, T. New regime of homogeneous flow in the deformation map of metallic glasses: Elevated temperature nanoindentation experiments and mechanistic modeling. *Acta materialia* 52, 20 (2004), 5879–5891.
- [139] SCHUSTER, B., WEI, Q., HUFNAGEL, T., AND RAMESH, K. Size-independent strength and deformation mode in compression of a *Pd*-based metallic glass. *Acta Materialia* 56, 18 (2008), 5091–5100.
- [140] SENKOV, O., AND SCOTT, J. Specific criteria for selection of alloy compositions for bulk metallic glasses. *Scripta materialia* 50, 4 (2004), 449–452.
- [141] SEO, S., MIN, O., AND YANG, H. Constitutive equation for *Ti – 6Al – 4V* at high temperatures measured using the SHPB technique. *International Journal of Impact Engineering* 31, 6 (2005), 735–754.
- [142] SHEN, J., YIN, W., WEI, Q., LI, Y., LIU, J., AND AN, L. Effect of ceramic nanoparticle reinforcements on the quasistatic and dynamic mechanical properties of magnesium-based metal matrix composites. *Journal of Materials Research*, 1–18.
- [143] SHENG, H., LUO, W., ALAMGIR, F., BAI, J., AND MA, E. Atomic packing and short-to-medium-range order in metallic glasses. *Nature* 439, 7075 (2006), 419–425.

- [144] SONG, S., AND NIEH, T. Flow serration and shear-band viscosity during inhomogeneous deformation of a *Zr*-based bulk metallic glass. *Intermetallics* 17, 9 (2009), 762–767.
- [145] SONG, S., AND NIEH, T. Direct measurements of shear band propagation in metallic glasses—An overview. *Intermetallics* 19, 12 (2011), 1968–1977.
- [146] SONG, S., WANG, X.-L., AND NIEH, T. Capturing shear band propagation in a *Zr*-based metallic glass using a high-speed camera. *Scripta Materialia* 62, 11 (2010), 847 – 850.
- [147] SPAEPEN, F. A microscopic mechanism for steady state inhomogeneous flow in metallic glasses. *Acta Metallurgica* 25, 4 (1977), 407–415.
- [148] STEIF, P., SPAEPEN, F., AND HUTCHINSON, J. Strain localization in amorphous metals. *Acta Metallurgica* 30, 2 (1982), 447–455.
- [149] SUNNY, G., YUAN, F., PRAKASH, V., AND LEWANDOWSKI, J. Effect of high strain rates on peak stress in a *Zr*-based bulk metallic glass. *Journal of Applied Physics* 104, 9 (2008), 093522.
- [150] TAYLOR, G. Thermally-activated deformation of BCC metals and alloys. *Progress in Materials Science(UK)* 36 (1992), 29–61.
- [151] TURNBULL, D. Under what conditions can a glass be formed? *Contemporary Physics* 10, 5 (1969), 473–488.
- [152] TURNBULL, D., AND COHEN, M. H. Free-volume model of the amorphous phase: glass transition. *The journal of chemical physics* 34 (1961), 120.
- [153] TURNBULL, D., AND COHEN, M. H. On the Free-Volume Model of the Liquid-Glass Transition. *The journal of chemical physics* 52 (1970), 3038.
- [154] VAIDYANATHAN, R., DAO, M., RAVICHANDRAN, G., AND SURESH, S. Study of mechanical deformation in bulk metallic glass through instrumented indentation. *Acta materialia* 49, 18 (2001), 3781–3789.
- [155] VOLKERT, C., DONOHUE, A., AND SPAEPEN, F. Effect of sample size on deformation in amorphous metals. *Journal of Applied Physics* 103, 8 (2008), 083539–083539.
- [156] VORMELKER, A. H., VATAMANU, O., KECSKES, L., AND LEWANDOWSKI, J. Effects of test temperature and loading conditions on the tensile properties of a *Zr*-based bulk metallic glass. *Metallurgical and Materials Transactions A* 39, 8 (2008), 1922–1934.
- [157] WANG, J., CHOI, B., NIEH, T., AND LIU, C. Crystallization and nanoindentation behavior of a bulk *Zr – Al – Ti – Cu – Ni* amorphous alloy. *Journal of Materials Research* 15, 03 (2000), 798–807.

- [158] WANG, W., DONG, C., AND SHEK, C. Bulk metallic glasses. *Materials Science and Engineering: R: Reports* 44 (2004), 45 – 89.
- [159] WEI, B., ZHANG, T., LI, W., SUN, Y., YU, Y., AND WANG, Y. Serrated plastic flow during nanoindentation in Nd-based bulk metallic glasses. *Intermetallics* 12, 10 (2004), 1239–1243.
- [160] WEI, Q. Strain rate effects in the ultrafine grain and nanocrystalline regimes— influence on some constitutive responses. *JOURNAL OF MATERIALS SCIENCE* 42, 5 (MAR 2007), 1709–1727.
- [161] WEI, Q., CHENG, S., RAMESH, K., AND MA, E. Effect of nanocrystalline and ultrafine grain sizes on the strain rate sensitivity and activation volume: fcc versus bcc metals. *Materials Science and Engineering: A* 381, 1 (2004), 71–79.
- [162] WEI, Q., JIAO, T., RAMESH, K., MA, E., KECSKES, L., MAGNESS, L., DOWDING, R., KAZYKHANOV, V., AND VALIEV, R. Mechanical behavior and dynamic failure of high-strength ultrafine grained tungsten under uniaxial compression. *Acta materialia* 54, 1 (2006), 77–87.
- [163] WEI, Q., KECSKES, L., AND RAMESH, K. Effect of Low-Temperature Rolling on the Propensity to Adiabatic Shear Banding of Commercial Purity Tungsten. *Materials Science and Engineering: A* 578 (2013), 394–401.
- [164] WEI, Q., RAMESH, K., MA, E., KESCKES, L., DOWDING, R., KAZYKHANOV, V., AND VALIEV, R. Plastic flow localization in bulk tungsten with ultrafine microstructure. *Applied physics letters* 86, 10 (2005), 101907–101907.
- [165] WRIGHT, W. J., SAHA, R., AND NIX, W. D. Deformation mechanisms of the $Zr_{40}Ti_{14}Ni_{10}Cu_{12}Be_{24}$ bulk metallic glass. *Materials Transactions-JIM* 42, 4 (2001), 642–649.
- [166] WU, F., ZHANG, Z., MAO, S., AND ECKERT, J. Effect of sample size on ductility of metallic glass. *Philosophical Magazine Letters* 89, 3 (2009), 178–184.
- [167] WU, F., ZHANG, Z., MAO, S., PEKER, A., AND ECKERT, J. Effect of annealing on the mechanical properties and fracture mechanisms of a $Zr_{56.2}Ti_{13.8}Nb_{5.0}Cu_{6.9}Ni_{5.6}Be_{12.5}$ bulk-metallic-glass composite. *Physical Review B* 75, 13 (2007), 134201.
- [168] WU, W., HAN, Z., AND LI, Y. Size-dependent malleable-to-brittle transition in a bulk metallic glass. *Applied Physics Letters* 93, 6 (2008), 061908–061908.
- [169] WU, X., GUO, Y., WEI, Q., AND WANG, W. Prevalence of shear banding in compression of $Zr_{41}Ti_{14}Cu_{12.5}Ni_{10}Be_{22.5}$ pillars as small as 150nm in diameter. *Acta Materialia* 57, 12 (2009), 3562–3571.

- [170] XIE, S., AND GEORGE, E. P. Size-dependent plasticity and fracture of a metallic glass in compression. *Intermetallics* 16, 3 (2008), 485–489.
- [171] XING, L.-Q., LI, Y., RAMESH, K., LI, J., AND HUFNAGEL, T. Enhanced plastic strain in *Zr*-based bulk amorphous alloys. *Physical review B* 64, 18 (2001), 180201.
- [172] XUE, Y., CAI, H., WANG, L., WANG, F., AND ZHANG, H. Dynamic compressive deformation and failure behavior of *Zr*-based metallic glass reinforced porous tungsten composite. *Materials Science and Engineering: A* 445 (2007), 275–280.
- [173] YADAV, S., AND RAMESH, K. The mechanical properties of tungsten-based composites at very high strain rates. *Materials Science and Engineering: A* 203, 1 (1995), 140–153.
- [174] YANG, B., LIU, C. T., AND NIEH, T. Unified equation for the strength of bulk metallic glasses. *Applied physics letters* 88, 22 (2006), 221911–221911.
- [175] YANG, B., RIESTER, L., AND NIEH, T. Strain hardening and recovery in a bulk metallic glass under nanoindentation. *Scripta materialia* 54, 7 (2006), 1277–1280.
- [176] YE, J., LU, J., LIU, C., WANG, Q., AND YANG, Y. Atomistic free-volume zones and inelastic deformation of metallic glasses. *Nature materials* 9, 8 (2010), 619–623.
- [177] YOKOYAMA, Y., MUND, E., INOUE, A., AND SCHULTZ, L. Production of *Zr*-based Glassy Alloy Rod of 30 mm in Diameter by a Cap-Cast Technique. *Materials transactions* 48, 12 (2007), 3190.
- [178] YUAN, G., QIN, C., AND INOUE, A. *Mg*-based bulk glassy alloys with high strength above 900MPa and plastic strain. *Journal of materials research* 20, 02 (2005), 394–400.
- [179] YUQIAO, Z., NISHIYAMA, N., AND INOUE, A. Development of *Ni – Pd – Pb* Bulk Metallic Glasses with High Glass-Forming Ability. *Materials transactions* 50, 6 (2009), 1243–1246.
- [180] ZHANG, B., WANG, R., ZHAO, D., PAN, M., AND WANG, W. Properties of *Ce*-based bulk metallic glass-forming alloys. *Physical Review B* 70, 22 (2004), 224208.
- [181] ZHANG, Q., ZHANG, W., AND INOUE, A. Preparation of *Cu*-based Bulk Metallic Glass with a Diameter of 25 mm by Copper Mold Casting. *Materials transactions* 48, 3 (2007), 629.

- [182] ZHANG, Y., ZHAO, D., WANG, R., AND WANG, W. Formation and properties of $Zr_{48}Nb_8Cu_{14}Ni_{12}Be_{18}$ bulk metallic glass. *Acta materialia* 51, 7 (2003), 1971–1979.
- [183] ZHANG, Z. F., ECKERT, J., AND SCHULTZ, L. Difference in compressive and tensile fracture mechanisms of $Zr_{59}Cu_{20}Al_{10}Ni_8Ti_3$ bulk metallic glass. *Acta Materialia* 51, 4 (2003), 1167–1179.
- [184] ZHENG, W., HUANG, Y., WANG, G., LIAW, P., AND SHEN, J. Influence of strain rate on compressive deformation behavior of a $Zr - Cu - Ni - Al$ bulk metallic glass at room temperature. *Metallurgical and Materials Transactions A* 42, 6 (2011), 1491–1498.
- [185] ZINK, M., SAMWER, K., JOHNSON, W. L., AND MAYR, S. G. Plastic deformation of metallic glasses: Size of shear transformation zones from molecular dynamics simulations. *Phys. Rev. B* 73 (May 2006), 172203.

LIST OF PUBLICATIONS AND PRESENTATIONS

1. W.H. Yin, F. Xu, O. Ertorer, Z. Pan, X.Y. Zhang, L.J. Kecskes, E.J. Lavernia and Q. Wei, Mechanical behavior of microstructure engineered multi-length-scale titanium over a wide range of strain rates, *Acta Materialia*, vol 61, p3781-3798.
2. J.H Shen, W.H Yin, Q. Wei, Y.L. Li and J.L. Liu, Effect of ceramic nanoparticle reinforcements on the quasistatic and dynamic mechanical properties of magnesium based metal matrix composites, *L. An. Vol 28 2013 J. Mater. Res.*
3. Z. Pan , F. Xu , S.N. Mathaudhu, L.J. Kecskes, W.H. Yin, X.Y. Zhang, K.T. Hartwig and Q. Wei. Microstructural evolution and mechanical properties of niobium processed by equal channel angular extrusion up to 24 passes, 60, 2012 *Acta Materialia*
4. W.H. Yin, L.J. Kecskes and Q. Wei. Mechanical Behavior of Zr/Hf-based Metallic Glasses, TMS 2012 Annual Meeting and Exhibition, 3/13/2012
5. W.H. Yin, C.L. Ma and Q. Wei. High Strain Rate Mechanical Behavior of a Zr-based Metallic Glass as a Function of Temperature, MRS 2012 Fall Meeting

VITA

Weihua Yin was born in Chaohu, Anhui province, P.R. China on November 17, 1987. After completing high school in 2004, he attend North China University of Technology in Beijing, China. He obtained his Bachelor of Science degree in Mechanical Engineering in 2008. After graduation from the college, he joined the University of North Carolina at Charlotte as a graduate student in the Departement of Mechanical Engineering and Engineering Science. In 2011, he graduated with a Master of Science degree and contiune his PhD study in the same university and focus on material engineering.